Alma Mater Studiorum · Università di Bologna

Scuola di Scienze
Corso di Laurea Magistrale in Fisica del Sistema Terra

Numerical simulation of magma pathways and vent distribution in rifts from the early stages to maturity

Relatore:
Prof.ssa Eleonora Rivalta

Presentata da:
Gaetano Ferrante

Correlatore:
Dott. Francesco Maccaferri

Sessione II
Anno Accademico 2020/2021

Contents

Abstract

Continental rifting is the process by which the lithosphere is thinned in response to extensional forces resulting in the formation of large scale fault-bounded basins. Rifting can be accompanied by a large amount of volcanism which can occur both inside and outside the rift depression, usually through the propagation of magma-filled fractures, called dikes. Here I use a model of crustal unloading to explain the temporal evolution of in-rift and off-rift volcanism in terms of the geometrical development of rifted areas and the competition between unloading pressure and tectonic stretching. I find that the progressive deepening of a rift is accompanied by the formation of a stress barrier under the basin which deflects ascending dikes, causing a shift of surface volcanism from the center to the flanks. The intensification of the barrier due to further deepening of the basin also promotes the formation of lower crustal sill-like structures that can stack under the rift, shallowing the depth at which magma is injected. If combined with the widening of the rift due to stretching, the sedimentary loading and the eventual shallowing of the Moho due to mantle upwelling, this would result in a later stage where dikes are injected from above the stress barrier, moving surface volcanism back to the inside of the rift.

Abstract

Il rifting continentale è un processo attraverso il quale la litosfera è assottigliata in risposta a forze estensionali che provocano la formazione di bacini a larga scala delimitati da faglie normali. Il rifting può essere accompagnato da una grande quantità di vulcanismo, che può manifestarsi tanto all'interno quanto all'esterno della depressione e che si verifica solitamente attraverso la propagazione di fratture piene di magma, dette dicchi. In questo lavoro uso un modello di unloading crostale per spiegare l'evoluzione temporale del vulcanismo in-rift e off-rift in termini dello sviluppo geometrico delle zone di rifting e della competizione tra la pressione dovuta all'unloading e la tensione tettonica. Trovo che il progressivo approfondirsi di un rift è accompagnato dalla formazione di una barriera di stress al di sotto del bacino, che deflette i dicchi in ascesa causando uno spostamento del vulcanismo superficiale dal centro verso i fianchi. L'intensificazione della barriera di stress dovuta a un ulteriore approfondimento del bacino promuove anche la formazione di strutture simili a sill nella bassa crosta che possono impilarsi al di sotto del rift, riducendo la profondità alla quale il magma è iniettato. Se combinato con l'allargamento del rift dovuto allo stretching, l'effetto dei carichi sedimentari e l'eventuale diminuzione della profondità della Moho dovuta all'upwelling del mantello, questo risulterebbe in una fase successiva in cui i dicchi si formano al di sopra della barriera di stress, riportando il vulcanismo superficiale all'interno del rift.

Introduction

Continental rifting is the process by which the lithosphere is thinned in response to extensional forces of different origin that result in the formation of large scale fault-bounded basins. A zone of the Earth subjected to continental rifting is referred to as a continental rift or simply a rift. Due to the deformation affecting the lithosphere, rifts are often areas of intense volcanic activity occurring both in the early and late stages of rifting, the latter ultimately leading to the splitting of the continent and the formation of a seafloor spreading center. Also, volcanism is often observed to shift from the inside to the outside of the rift depression and conversely, leading to an ongoing debate about the causes of this variability. Although the distribution of volcanism in rift areas is often well constrained, at least for the case of the most studied rifts, its connection with the physical mechanisms responsible for the propagation of magma through the crust has been poorly investigated. Maccaferri et al. (2014) explained off-rift volcanism in terms of the stress changes induced in the crust by the unloading of the rift depression. They found that when the unloading pressure dominates over the tectonic tensional stresses, the least compressive eigenvector becomes vertical under the basin, deflecting ascending dikes and forcing their way up to the rift flanks. Following their work, in this dissertation I seek to investigate how the progressive deepening of a basin is able to influence the spatio-temporal distribution of volcanism in rift zones.

In CHAPTER 1 I will start by defining some basic terminology regarding rifts and show the principal ways in which rifts are commonly classified. I will introduce the main controversies regarding rift nomenclature and classification. Thereafter, I will describe some phenomenological aspects of rifts, with a special consideration for rift geometry and rift-related volcanism.

In CHAPTER 2 I will outline the main models for the propagation of magma to the Earth's surface and then focus on dikes and their properties. I will introduce the the principal schools of thought about dike propagation and a fundamental controversy about the interaction of dikes with pre-existing fractures.

In CHAPTER 3 I will develop a crustal unloading model to describe how volcanism in rift areas is influenced by the temporal evolution of the basin and rift geometry. I will focus on two basic geometries to represent the rift cross section, namely a rectangular one and a right triangular one.

In CHAPTER 4 I will use and modify a published boundary element dike

propagation code to investigate the effects of dike induced stresses on the trajectories of subsequent dikes in a tectonic and unloading setting.

In CHAPTER 5 I will provide a summary of the main results of the work and point out the principal limits of the model. Finally, I suggest how this thesis can contribute shading light on some aspects of rift formation and how this research could be extended in future studies.

Chapter 1

Volcanism in zones of continental rifting

1.1 Definition

The modern concept of continental rifting stems from British geologist John Walter Gregory's first definition of a rift valley. After visiting Kenya in 1892 he published his classic 1896 book The Great Rift Valley, in which he defined a rift as "a linear valley with parallel and almost vertical sides, which has fallen owing to a series of parallel faults". This definition was very similar to an earlier description of the East African fracture zone given by Austrian geologist Eduard Suess, who had described the long troughs that bounded the great lakes region as *Brüche* and related them to the *Grabens* observed in the Rhine valley. These early definitions were basically interchangeable but although they successfully described the morphological features of rifts, they failed to account for the lithospheric and asthenospheric dynamic processes associated with rifting. More recent definitions therefore focus on both the external features of rifts and the internal modifications connected with them. Burke (1977) defined rifts as "zones along which the entire lithosphere has ruptured in extension" and this definition was later used in a modified form by the American Geological Institute Glossary of Geology. However, Olsen & Morgan (2006) argue that the term "rupture" does not easily adapt to the lithosphere as a whole, also given that a complete breakup of the lithosphere may not occur until the late stages of rifting (i.e. the early stages of seafloor spreading) and therefore suggests to more generally define a continental rift as "an elongate tectonic depression associated with which the entire lithosphere has been modified in extension".

The requirement that the entire lithosphere should be affected by the deformation process makes these more recent definitions way more strict than the classical ones. For example Olsen's definition does not include small extensional features (such as simple grabens), highly extended terranes (HETs)[1] and pas-

[1]Broad zones of extension forming shallow basins or uplift, not always associated with

sive margins[2]. However, it is necessary to point out that distinguishing between some of these structures is not always trivial. Moreover, classifications made for the sake of clarity and simplification often hide the bigger picture and it should always be remembered that most of the features we have mentioned above can represent different stages of the evolution of the same process and therefore be related in many ways, as Olsen & Morgan (2006) highlight.

1.2 From rift to drift

Continental rifting is generally considered as the first step in the development of a new ocean basin in what is usually called the Wilson cycle of ocean opening and closing. If the extensional forces are not relieved after the rift valley is formed, the rift zone can evolve into a *seafloor-spreading center*, or *ocean ridge*. At a ridge, new ocean crust and lithosphere are formed by partial melting of hot upwelled mantle rocks. If the spreading does not stop, a new ocean basin is formed. The margins of the ocean can eventually subside with respect of the adjacent continent as the oceanic lithosphere grows thicker and more unstable and an *ocean trench* is created. If the subduction rate is greater that the spreading rate the ocean can eventually start closing, leading to the subduction of the ridge itself and the collision of the continents. The Himalayas are a present example of the creation of a mountain range by collision of the Indian subcontinent and Eurasia. A visual representation of the Wilson cycle can be found in figure 1.1.

Some rifts never make their way into a spreading center and the splitting process is stopped, giving birth to a *failed rift*. It is interesting to note that this is not a universally accepted definition, as many argue that it can be misleading in that *failed rifts* are actually perfectly successful rifts and prefer to call them *failed oceans* instead (Burke 2011, Şengör & Natal'in 2001).

1.3 Terminology and classification

Continental rifts are usually grouped according to several classifications that take into account different aspects of their morphology, evolution and state of activity. Some of these definitions fall beyond the purposes of this work, so that only the most widespread concepts will be mentioned here. A short glimpse of some of the most studied rifts and their classification according to the different perspectives treated in this section and in section 1.2 is provided in table 1.1.

1.3.1 State of activity

A common distinction takes into account the state of activity of rifts. A *modern rift* is a rift where tectonic and/or magmatic activity has occurred in the last

major modification of the lithosphere (Olsen & Morgan 2006).

[2]The products of successful continental separation, where the initial tectonic depression develops into an ocean basin.

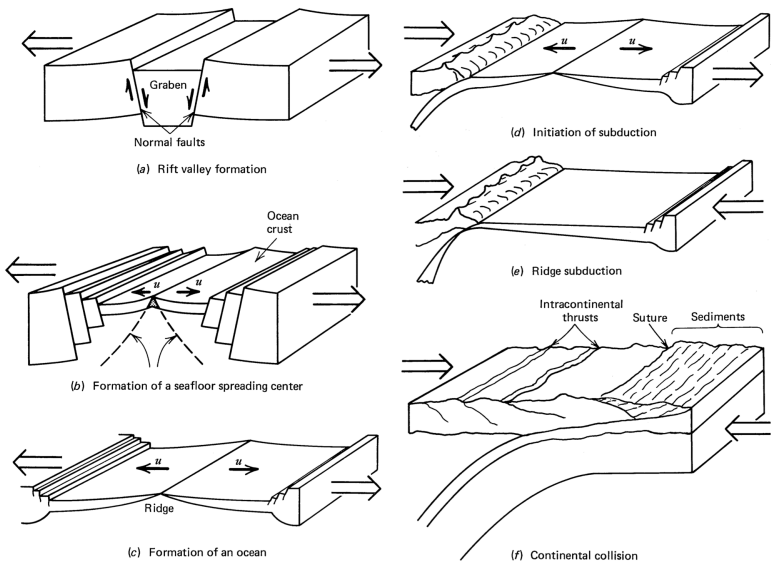

Figure 1.1: The Wilson cycle of ocean opening and closing as described in section 1.2. (a) Extensional forces result in the formation of a rift valley. (b) Prolonged extension causes the formation of a seafloor spreading center. (c) The spreading center develops into an ocean. (d) Subduction initiates at the continental margins. (e) If the subduction rate is greater than the spreading rate the ocean ridge may eventually subduct. (f) If subduction continues the continental margins will collide. Modified from Turcotte & Schubert (2002).

Name	Stage of evolution	State of activity	Dynamic processes
East African Rift System	Rift	Modern	Active
Red Sea/ Gulf of Aden	Spreading center	Modern	Active
Baikal Rift	Rift	Modern	Passive
Midcontinent Rift System	Rift	Paleorift	Passive
Basin and Range	Rift	Modern	Passive
Oslo Rift	Failed rift	Paleorift	Passive

Table 1.1: Some of the most studied rifts and their classification based on the terminology discussed in Sections 1.2 and 1.3. All the rifts considered here are examples of *narrow* rifts, with the exception of the Basin and Range province.

10 My, while a *paleorift* has not experienced recent tectonic and/or magmatic activity and is devoid of any significant remaining transient thermal phenomena (Morgan & Ramberg 1987). Rifts can form along the branches of triple junctions, namely the zones of the Earth where three tectonic plates meet. A branch where the splitting process is aborted is called a *failed arm*. A typical example of a failed arm is considered to be the Benue valley of the Central African Rift System, that aborted its extension in the Late Cretaceous (100.5–66 My) as the other two rift segments opened as part of the Atlantic basin (Condie 2013).

Not all of these definitions are universally accepted and different interpretations of the same term often exist. For instance, it is quite common to find the terms *failed rift* (defined in section 1.2) and *aulacogen* listed as synonyms, while some authors give them different meanings and define an *aulacogen* as a "paleorift that has been reactivated by compressional deformation" (Olsen & Morgan 2006) or a "rift that dies out towards the interior of a continent" (Condie 2013).

1.3.2 Active and passive rifts

Sengör & Burke (1978) suggested a dynamical classification that accounts for the forces at the base the rifting process and distinguished between active and passive rifting (figure 1.2). *Active rifting* occurs in response to thermal upwelling of the asthenosphere, usually related to the ascent of a mantle plume to the base of the lithosphere. This is believed to be the case of the East African Rift, as many studies have related it to the action of a deep superplume originating beneath southern Africa and rising towards Eastern Africa (Ritsema et al. 1999). Zones of active rifting are characterized by doming and strong volcanism in the early stages followed by faulting and graben formation in later stages. Magma in active rifting zones is usually related to melting by decompression of the

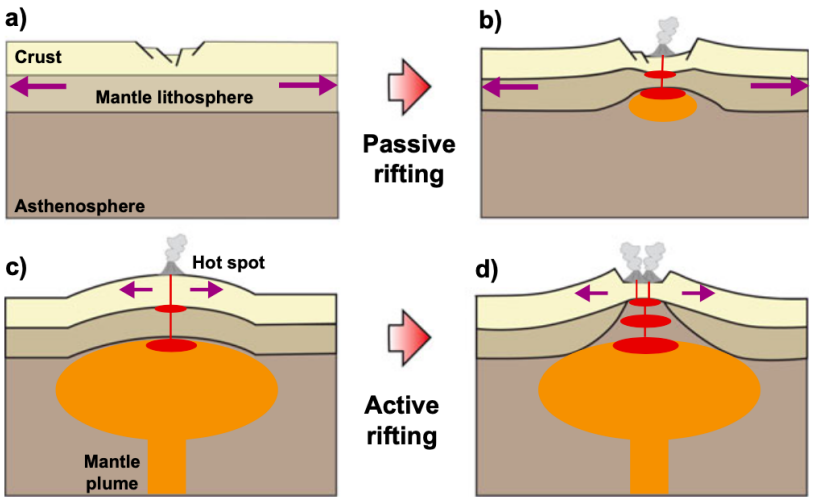

Figure 1.2: Schematic representation of the active and passive classification of rifting of Sengör & Burke (1978). From Acocella (2021).

rising plume. On the other hand, *passive rifting* describes a process in which deformation is produced by regional stress fields usually originating from remote plate boundary forces. Therefore, in zones of passive rifting faulting is usually the first detectable event and volcanism follows later on. This is caused by the stretching and thinning of the lithosphere that force the asthenosphere to upwell and melt by decompression, generating magma.

1.3.3 Merle's classification

Although being very popular in the scientific literature, the "active-passive" classification is not the only one and it is not free from criticism. Merle (2011) argues that clear-cut evidence of active rifting is limited to the East African Rift, while numerous rifts reveal a tectonic evolution that combines aspects from both active and passive rifting (e.g. the European Cenozoic Rift System), giving rise to some ambiguity in the distinction. Also, the study of Phanerozoic rifts showed that volcanic activity and doming in rift zones can be better explained as consequences of lithospheric stretching than as main driving forces themselves (Ziegler & Cloetingh 2004).

As an alternative Merle suggests a new classification based on the four tectonic environments at the base of the formation of rifts, namely subduction zones, mountain chains, mantle plumes and transform faults. The typical *subduction-related* setting is the formation of back-arc basins resulting from the roll-back of the subducting slab (e.g. the Sea of Japan, the Black Sea). However, subduction-related extension can also result in different rifting settings than back-arc basins. This is the case of the Basin and Range region and the

Wudalianchi volcanic field. During continental collision, extensional deformation in the foreland can cause *mountain-related* rifts. This is the case of the Baikal Rift, which results from the lateral escape of the Amuria–North China plate due to far-field stresses resulting from the India-Asia collision, and the European Cenozoic Rift System, which has been explained in terms of the alpine compression. *Transform-related* rifts are usually associated with the formation of pull-apart basins along strike slip faults, such as the Dead Sea and the California Ridge Basin, while the Alpine Tethys Ocean is a good example of a transform-related rift successfully developed into an oceanic ridge. Last, *mantle plume-related* rifts are very rare on Earth and the East African Rift is the only verified example, most likely associated with the African super-plume revealed by Ritsema et al. (1999).

This classification was motivated by the need for a more complete distinction than the "active-passive" one and a less complicated grouping than some of the following attempts (Şengör & Natal'in 2001, Sengor 1995). In addition to capturing the essential features of the various rifting areas, it is very useful in that it reveals how rift zones that share the same tectonic origin can differ from each other because of numerous local factors that influence lithospheric deformation and also manages to link the different tectonic environments from a causal point of view.

1.3.4 Lithospheric extension

Both active and passive rifting processes result in extension of the lithosphere but the way this extension occurs can be influenced by numerous parameters. It is now believed that continental lithosphere subjected to extensional stresses can extend in two different ways, namely the wide rift mode and the narrow rift mode. In the *narrow rift* mode deformation is localized along areas of size comparable to the thickness of the lithosphere so that normal faulting occurs on scales of the order of 100km. This is the case of many of the most studied rifts in the world, such as the Rhine graben, the East African Rift System and the Baikal Rift, among others. On the other hand, the *wide rift* mode is localized over length scales several times larger than the thickness of the lithosphere and occurs during or after the cessation of continental collision, as in the Tibet and Basin and Range regions, respectively (Brun 1999). Unlike narrow rifts, wide rifts do not usually show significant gradients in crustal thickness. It is believed that the mode of extension is determined by a combination of the initial thermal state and rheology of the crust, its thickness and the strain rate. For example, wide rifts are thought to be favored by high temperatures and low strain rate, while lower temperatures and high strain rate are thought to promote narrow rifts. However, this is not always the case. The Main Ethiopian Rift is an example of a narrow rift ($80 - 100$ km wide) developed in a weak lithosphere characterised by presence of a hot lower crust and uppermost mantle due the action of a warm plume. This rheological layering should have resulted in distributed deformation and wide rifting, which are clearly not observed in the MER. Keranen et al. (2009) suggest that the common models of rift mode formation that focus only

on temperature, thickness, and vertical strength profiles are not sufficient, and that inherited structures and associated lithospheric weaknesses serve as the primary controls on the mode of extension.

It should be pointed out that Buck (1991) also included *core complexes* in his dissertation as a third mode of lithospheric extension. Core complexes are characterized by the exhumation of deeper ductile crust to the surface resulting in fault bounded domal structures, as can be observed in California's Whipple Mountains. However, Brun (1999) argued that core complexes should not be considered a distinct mode of extension but simply anomalies within the wide rift mode. This still remains a debated issue, as it also hints at how all the cases mentioned above could only be three different steps of the long time evolution of an extending continental region. This could in fact be the case of the southern Basin and Range region, as Buck (1991) suggested.

1.4 Rift geometry

Continental rifting results in the formation of large-scale depressions on the surface of the Earth, whose morphology is highly dependent on the different parameters influencing the deformation, namely dynamical forces, tectonic setting, mode of lithospheric extension, and so on. Hence the difficulty of classifying rifts according to their geometry. However, some common features can still be found.

The brittle response to extension of the upper crust usually accomodates deformation through the formation of normal faults. The earliest and simplest extensional model of rifting was the "wedge hypothesis" developed by Meinesz in 1950, in which a full-graben shaped wedge of continental crust bounded by normal faults sinks into the fluid mantle until isostatic equilibrium is reached (figure 1.3). The lack of seismic evidence of the projection of deep crust into the mantle lead to a refinement of this model by Bott (1976). Here, the wedge hypothesis is restricted to the brittle upper crust, while ductile stretching and thinning occur at depth. However, as Rosendahl et al. (1986) and Bott (2006) argue, the fundamental unit of rift geometry consists in the development of a half-graben bounded by a single major fault (figure 1.3). This geometry is accounted for by the "flexural cantilever" model developed by Kusznir et al. (1995). The fundamental units can in turn link with each other to form different geometries, such as full-grabens or alternating polarity half-grabens.

With regards to the quantitative features of rift basins, some characteristic dimensions can be found. As will be outlined in chapter 3, the main parameters we are interested in to develop our model are the width and depth of a basin and the dip of its boundary faults. We define the *width* W of a rift basin as the horizontal distance between its boundary faults, as shown in figure 1.4. If the rift basin has a perfect half-graben shape we can think of the width of the basin as the horizontal length of the subsided area. Rift basins are usually up to several tens of kilometers wide, although rift widths can show a great variability from a basin to the other and also along the length of the same basin. The *depth* D of the rift is defined as the maximum depth of subsidence reached by the hanging

wall due to fault slip, as shown in figure 1.4. The *dip* of the boundary faults follows the classical definition for normal faults. Faulting at the boundaries of extensional rift systems usually occur at high angles (with dips at around 60°or more) but low angle (<45°) dipping faults can also be observed across the stretched zone, usually related to wide rifting and detachment surfaces. Rift basins are also classified in terms of their *length* L, namely the dimension along the axis of the rift. This can reach hundreds of kilometers for single rift basins or even thousands if rift systems are considered. As rift basins are usually much longer than they are wide, a plane strain approximation has been employed in this work.

The parameters describing rift geometry can vary as a function of time as the rift evolves in response to tectonic stresses. Depending on the forces in action, the strain rate, the composition and temperature of the lithosphere, rift evolution may result in different scenarios from one rift to another, making it impossible to define a common pattern. Nonetheless, some general behaviors can still be identified. One typical effect of rift evolution is the deepening of the basin due to faulting in order to accomodate the extensional strain, resulting in an increased D. In this work, rift evolution will be in fact simulated by the progressive deepening of a basin, through the application of a gradually increasing unloading. However, rifts may also undergo modifications in length L and/or in width W. Changes in length are usually associated with the propagation of the area affected by extensional deformation, which is referred to as *rift propagation*. Rift propagation may or may not occur as a smooth process and is highly influenced by the presence of inherited lithospheric weaknesses (such as ancient orogenic belts) (Dunbar & Sawyer 1988), making the order and timing of events sometimes difficult to assess. This will not be accounted for in my model, as a plane strain approximation will be employed. Lastly, prolonged extension may eventually result in the widening of the basin, especially in the mature stages of rifting when close to continental break-up. In order to assess the possible effects of this phenomenon, I will test differences in my results arising from different values of rift width W.

1.4.1 An example from the Main Ethiopian Rift

The Main Ethiopian Rift of Africa (MER) represents a useful showcase of the different geometries listed above and also hints at some of their possible evolutions. The rift depression is between 30 and 100 km wide and is bounded by steep escarpments whose height can vary from a few hundreds to a few thousands of meters. The MER is usually divided into three portions that differ both in morphology and temporal evolution: Northern (NMER), Central (CMER) and Southern (SMER).

The shape of the NMER is generally asymmetric, as suggested by seismic refraction and supported by magnetotelluric analysis (Corti 2009). Subsidence in this portion has probably been gradual, with the present steep escarpments only developing between the Pliocene and Pleistocene (~ 2.5 Ma), as constrained by Chernet et al. (1998). On the other hand, the CMER showcases a more varied

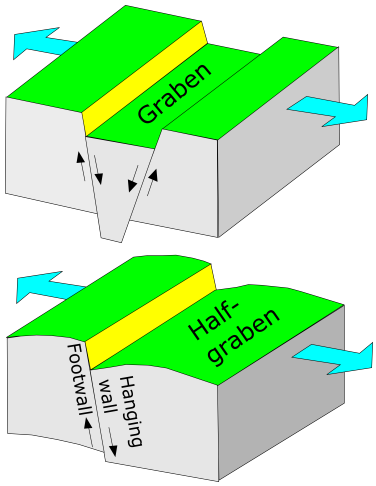

Figure 1.3: Schematic representation of a full-graben (left hand panel) and a half-graben (right hand panel).

evolution. According to Woldegabriel et al. (1990), this portion formed in two stages: between the late Oligocene and the early Miocene ($\sim$ 20 Ma) the rift presented a typical asymmetrical configuration, with half-graben structures of opposing polarity alternating along axis. Between the late Miocene or early Pliocene, increased volcanotectonic activity resulted in the formation of a symmetrical rift, more similar to the shape of an actual full-graben. Lastly, the SMER is characterized by a more complex architecture, with the coexistence of two near-parallel basins (namely Chamo and the Galana basins) separated by the Amaro horst. The Chamo basin appears to be roughly symmetrical, while the Galana basin is more tilted towards the central horst. However, no detailed geophysical studies are available to well constrain the subsurface rift architecture of this area, as Corti (2009) points out.

Rift propagation through the different segments of the MER was not a smooth process (Keranen & Klemperer 2008): extension did not occur continuously but rather at discrete episodes interrupted by periods of relative quiescence. The temporal evolution of the segments has been interpreted in terms of different models of rift propagation, mainly derived from two end-members: a northward propagation from southwestern Ethiopia towards the Afar depression (Wolfenden et al. 2004) and a southern propagation from the Afar towards the SMER (Bonini et al. 2005). However, more recent studies suggest a less linear propagation of extensional deformation (Keranen & Klemperer 2008, Rooney et al. 2007) and fall beyond the purposes of this work.

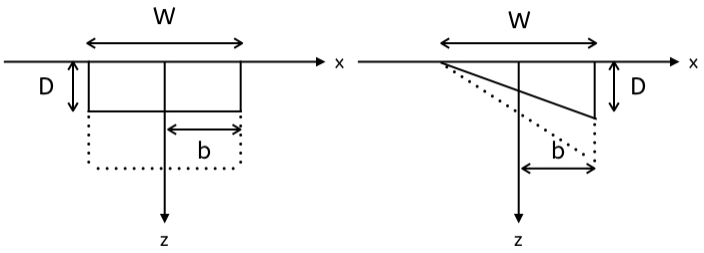

Figure 1.4: *Left*: model representation of a full-graben with characteristic parameters. *Right*: model representation of a triangular rift with characteristic parameters. Dashed lines represent the deepening of the basin with time.

1.5 Rift-related volcanism

Regardless of the dynamic forces responsible for lithospheric deformation causing rifting to occur, volcanism and magma transport play an important role in the development of continental rifts. Lithospheric thinning is usually associated with upwelling of the asthenosphere and melting by decompression, promoting magma migration to the surface and leading to the formation of volcanic structures inside and outside the rift depression (figure 1.5). Furthermore, the presence of magma within a rift is fundamental in assisting extension itself, especially in the later stages of rifting: as the continental rift gradually evolves into a spreading center, deformation starts shifting from faulting and ductile stretching to magma-accommodated extension and is therefore promoted at lower levels of stress compared to non-magmatic rifts (Buck 2004).

Eruption of ascending magma in rift areas is observed both inside or outside the rift basin, giving rise to some questions about what drives this spatial variability. Bosworth (1987) explained off-axis volcanic belts in the East African Gregory Rift in terms of the lithospheric extension model derived by Wernicke (1985). This model predicted major lithospheric thinning associated with continental rifting to be offset from the surface rift architecture because of the presence of low-angle detachment faults. This would indeed cause volcanism to occur at some distance from the upper crustal basin structure. However, the majority of the most studied rifts provide evidence that lithospheric thinning associated with rifting mostly occurs under (or nearly under) its surface manifestation, as Bott (2006) argues. Ellis & King (1991) suggested that flank volcanism in rift zones should be explained in terms of the flexural deformation of the crust due to normal faulting. This would in fact cause dilatational strain in the footwall at the base of the crust but also horizontal compression at the top of the footwall, possibly preventing shallow dike propagation (Maccaferri et al. 2014).

Maccaferri et al. (2014) showed that off-rift volcanism can be explained by

considering the physical mechanisms at the base of magma propagation. They pointed out that the propagation of magma through the crust is regulated by a number of mechanisms, such as fracture mechanics and fluid dynamics, and that evaluating the elastic stress field is critical to develop a correct model of magma trajectories. They found that when the unloading stresses generated in the crust by the formation of a rift basin dominate over the tectonic stretching a "stress barrier" appears under the rift. This deflects dikes rising to the surface and causes them to erupt offset from the basin. Also, they found that injected magma can form subhorizontal magmatic sheets that can get trapped as stacked sills if their injection occurred near the rift axis.

While throwing light on a plausible reason for off-rift volcanism, this model did not attempt to investigate how progressive crustal unloading affects the redistribution of volcanism in rift zones. Also, the analysis was limited to the uniform strip unloading case, that was meant to reproduce a full-graben shaped depression. However, as pointed out in section 1.4, rift basins preferentially develop as half-grabens. The effective way in which this model links surface volcanism with the physical processes responsible for magma migration makes it suitable for investigating the temporal evolution of volcanism in rifted areas as driven by the geometrical development of a basin, as I will do in this work. Also, it is straightforward to extend it to different unloading geometries, such as the triangular one required to simulate a half-graben.

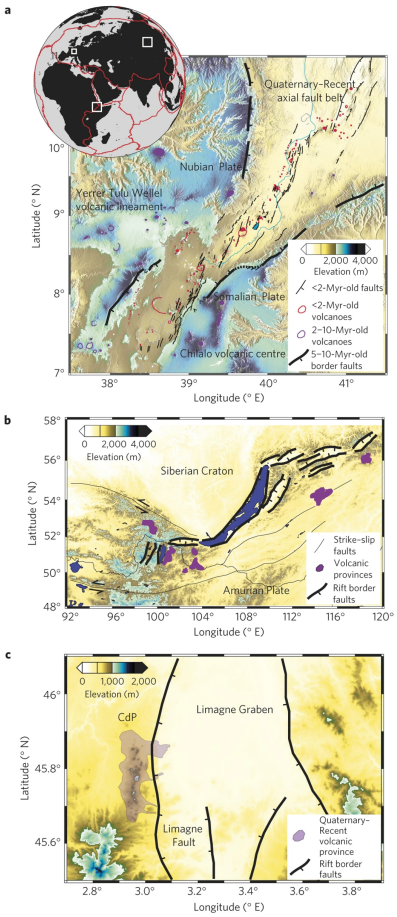

Figure 1.5: Topographic, structural and volcanic architecture of the MER (a), Baikal Rift (b) and Limagne Graben (c). Image taken from Maccaferri et al. (2014).

Chapter 2

Magma propagation through dike ascent

2.1 Mechanisms of magma transport

The problem of magma transport in the Earth's interior has been a highly debated one. A number of mechanisms have been traditionally proposed to explain magma propagation through the lithosphere, such as stoping, diapirism and diking, giving rise to a long-standing question about which one would better explain the geological and geophysical evidence. *Stoping* consists in the erosion of the walls of a magma chamber due to gravity or magma pressure, resulting in the net upward migration of melt. This mechanism fails to explain the emplacement of large magmatic intrusions (*plutons*), as stoping would produce a larger quantity of xenoliths[1] than it is usually observed. *Diapirism* occurs when a viscous mass of material moves in a viscous denser material, therefore ascending because of its positive buoyancy. Diapirs have been discredited as an efficient mechanism of magma propagation through the crust, as their slow ascent velocities cause their solidification to often occur below the depth where plutons are found. On the other hand, it is since decades acknowledged that dike propagation can provide the high velocities needed for the presence of xenoliths to be explained and early freezing to be prevented.

2.2 Diking

Diking is the process by which magma is transported by magma-filled fractures propagating through the surrounding rocks. Since the late 1980s diking has been recognized as the predominant magma transport mechanism in the brittle upper crust. Not only most eruptions occur through dikes, but also plate divergence in zones of continental rifting and ocean spreading mostly occur in the form of

[1] Fragments of rock settled in magma coming from different sources than the magma itself.

numerous episodes of diking. Moreover, the importance of dike modeling is not limited to the understanding of magma migration, as our knowledge about dike behavior can also be applied with minor modifications to industrial hydraulic fracturing processes.

Although the lower crust may have a more ductile rather than brittle behavior, there is still evidence that erupted magma may have moved for the vast majority of its path as a dike (Kavanagh 2018). An explanation for this could lie in the rheological response of rocks, which is strongly dependent on the ratio of rock to magma viscosity, strain rate and the timescale of the considered phenomenon. Rubin (1993) addressed the problem of the minimum viscosity contrast between rock and magma necessary for rock to behave in a brittle rather than a ductile way. Using self-similar solutions of fluid-filled, pressurized cracks in viscoelastic materials he concluded that if $\eta_r/\eta_m > 10^{11} - 10^{14}$ the host rock tends to respond elastically. This is true for basalts and low-viscosity felsic magmas, even for relatively high host rock temperatures

2.2.1 Dike geometry

Field observations show that dikes appear as planar, sheet-like bodies with three different characteristic dimensions, namely length, breadth and thickness (figure 2.2). The *length* is generally defined as the dimension along the direction of propagation. If vertically propagating dikes are considered, the length is usually referred to as *height*. This is usually the greatest of the three dimensions, ranging from several hundreds meters to a few kilometers (Rivalta et al. 2015). On the other hand, the *thickness* is the shortest dimension and it represents the opening of the dike. It typically ranges from tens of centimeters to several meters. Lastly, the third dimension is often called *width* or *breadth* and it is of size comparable to the length, with the latter being usually greater. A schematic representation of a vertically propagating dike is shown in figure 2.1, showing the three characteristic dimensions described above.

As I have already pointed out in chapter 1 with regards to rifts, my model is built on a plane strain approximation. This will imply that the volume of magma contained in a dike will be represented by its cross-section in my simulations. As for the case of rifts, the plane strain approximation is justified by the aspect ratios of dikes: according to Kavanagh (2018), the typical thickness-to-breadth ratio of dykes ranges from 0.01 to 0.0001, broadly supporting my assumptions. The main drawback, however, is that I won't be able to simulate along rift dike propagation.

2.3 Dike propagation

2.3.1 Classical approaches

The problem of modelling dike propagation is far from trivial. A number of physical processes should be considered in order to fully describe the propagation

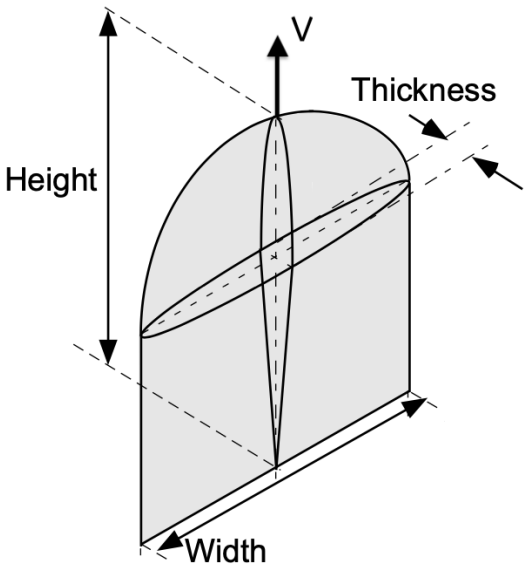

Figure 2.1: Schematic representation of a dike propagating vertically with velocity **V** and its three characteristic dimensions. Modified from Watanabe et al. (2002).

of fluid-filled fractures, such as fracture and plasticity of the host rock, viscous effects of the filling fluid, phase changes due to pressure gradients. Approximations are therefore employed to make the problem more tractable (Rivalta et al. 2015).

Dikes can propagate as fluid-filled cracks either connected to a pressurized cavity or isolated from any other driving source. Nakashima (1993) referred to these two modes of propagation as Type I and Type II, respectively. Type II dikes are usually modelled starting from the approach developed by Weertman (1971) for studying water-filled crevasses in glaciers. The main result is the existence of a critical volume V_c for autonomous dike propagation. For volumes V lower than V_c the buoyancy-induced stresses in the vicinity of the dike tips (embodied by the *stress intensity factor* K_I) do not overcome the *fracture toughness*[2] of the rock K_c and the fracture is static. If $V \geq V_c$ fractures begin to close at one end and simultaneously break the rock at the other end, therefore promoting self-propelled propagation.

Weertman's classical approach to diking implies a strong approximation with respect to viscous effects due to magma flowing into the crack, which are either simplified or totally neglected. The coupling between elastic fracturing and flow of fracture-filling fluids has been carried out since Spence et al. (1987) through the lubrication approximation, assuming steady state flow. This approach pro-

[2]A property that measures the resistance of a particular material to the propagation of a fracture (Pollard et al. 2005).

Figure 2.2: Field observation of a frozen eroded basaltic dike at Etna volcano (Italy). People for scale.

vides an accurate prediction of the velocity and shape of dikes.

However, both models suffer from important limitations. The Weertman approximation of negligible viscosity can turn out to be highly inappropriate for high viscosity magmas, while the lubrication theory is limited by the null fracture toughness assumption and to very simple planar geometries and stress distributions. Mixing these models requires the use of numerical approaches.

2.3.2 Numerical models

Most numerical models dealing with fluid-filled fracture propagation are based on the boundary element method (BEM) approach. This technique involves the discretization of the sole domain boundaries and it is therefore suitable for dike propagation problems that usually involve the addition and removal of fracture elements at each iteration. In chapter 4 I will simulate the propagation of dikes in the stress field typical of rifting environments. I will also, for the first time regarding rifts, include the stress induced by the previously intruded dikes. To do so, I will extend the FORTRAN90 code developed by Maccaferri et al. (2010) and based on the boundary element scheme first developed by Dahm (2000). The mathematical model of the code, as described by Maccaferri et al. (2011), will be briefly outlined here.

The fluid-filled fracture is modelled as a boundary element crack composed of N dislocation elements opening in a brittle elastic medium, as shown in figure 2.1. Prescribed stresses are assigned at the midpoint of each element so that the normal and tangential component of the Burgers vector of each dislocation can be computed solving

$$\begin{cases} \sum_{j=1}^{N} [b_j^n N_{ij}^n + b_j^s N_{ij}^s] = -\Delta P_i \\ \\ \sum_{j=1}^{N} [b_j^n S_{ij}^n + b_j^s S_{ij}^s] = -\tau_i \end{cases} \tag{2.1}$$

where $i = 1, ..., N$ and the symbols are defined in table 2.1. The overpressure $\Delta P_i = \Delta P(x_i, z_i)$ is the difference between the fluid pressure and the confinement pressure, which is in turn given by the superposition of the lithostatic pressure $P_{lit}(z)$ and the normal component of external stresses $\sigma(x, z)$. We can therefore write

$$\Delta P(x, z) = \rho_f g(z - z_t) - P_{lit}(z) + \Delta P_K + \sigma(x, z) \tag{2.2}$$

where ΔP_K accounts for the fluid compressibility and ρ_f varies according to any variation of fluid volume.

Equation 2.1 is based on the displacement discontinuity method (DDM) described by Crouch et al. (1983). A quasi-static approach is used here to simulate fracture propagation. The trajectory is found by testing different propagation directions ahead of the dike tip and choosing the one that maximizes the total energy release $\Delta E = \Delta W + \Delta G$, where ΔW and ΔG are the changes in elastic and gravitational energy, respectively. If ΔE overcomes a given threshold E_T,

propagation occurs and a new element is added to the crack. For elastic-brittle materials we have

$$E_T = 2(1 - \nu^2)\gamma_s \tag{2.3}$$

with ν being the Poisson's ratio of the rock and γ_s the specific surface fracture energy. Maccaferri et al. (2011) further decompose ΔW and ΔG into contributions coming from the surrounding rock and the fluid, so that $W = W_r + W_f$ and $G = G_r + G_f$. W_r is the work done against the elastic forces to open the fracture surface by an amount equal to the Burger's vector; W_f represents the variation in elastic energy of the compressible fluid subjected to volume change; G_f is the contribution of the mass of the fluid to the variation of gravitational potential energy; lastly, G_r is the work done by gravity forces in creating the observed displacement field in the surrounding rock and it equals to zero when far away from boundaries.

Symbol	Definition
b_j^n	normal component of Burger's vector for j-th element
b_j^s	shear component of Burger's vector for j-th element
N_{ij}^n	normal traction at the midpoint of i-th element due to the normal component of Burger's vector at j-th dislocation
S_{ij}^n	shear traction at the midpoint of i-th element due to the normal component of Burger's vector at j-th dislocation
N_{ij}^s	normal traction at the midpoint of i-th element due to the shear component of Burger's vector at j-th dislocation
S_{ij}^s	shear traction at the midpoint of i-th element due to the shear component of Burger's vector at j-th dislocation
ΔP_i	overpressure on the fracture surface of i-th element
τ_i	shear traction on i-th element due to any topographic or tectonic stress

Table 2.1: Symbols and definitions of the parameters employed in section 2.3.2.

2.3.3 The problem of pre-existing fractures

Stresses acting in the crust are able to deform the rock in a variety of ways. This is especially true in rifted areas, where faulting and diking concurrently occur in a limited region of space. This motivates a crucial discussion about whether dikes could use of pre-existing faults to make their way up to the surface.

Dikes have usually enough energy to propagate autonomously through the crust, so that pre-existing fractures are not needed to transport magma (Rivalta et al. 2015). Also, dikes and faults commonly orient themselves according to different criteria. According to Anderson (1951), faulting occurs on a plane that is oriented at an angle with respect to the directions of the minimum and maximum principal stresses. On the other hand, dikes are commonly observed to open roughly in the direction of the least compressive stress (Anderson 1972)

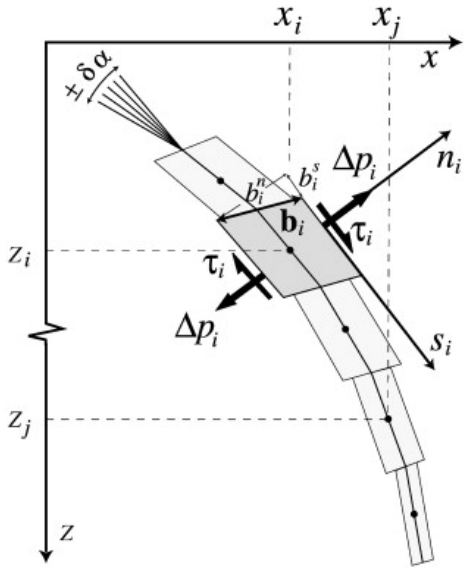

Figure 2.3: Geometric representation of the BEM model of a dike with symbols and reference frames. From Maccaferri et al. (2011).

and tend to propagate perpendicular to that. In other words, faults being shear dislocations, they tend to orient to the optimal shearing direction, while dikes needing to open and accomodate a volume, they tend to intrude perpendicular to the least compressive direction (figure 2.4). Thus, faults are in general the most difficult paths for magma pockets.

However, the behaviour of dikes may not be as straightforward. Numerical models usually assume that dikes propagate in the direction of maximum energy release (Dahm 2000, Maccaferri et al. 2011) and this could significantly differ from being perpendicular to σ_3, depending on the actual stress setting. The interaction between dikes and pre-existing fractures can therefore be more complicated. Ziv et al. (2000) investigated the stability of dike intrusions along pre-existing fractures oriented obliquely with respect to the least compressive stress. They concluded that even for magma pressures that exceed the dike-normal external stress, it is still unlikely for dikes to make use of a pre-existing fracture. Nevertheless, three conditions are identified that would promote such circumstance:

1. The fracture is almost perpendicular to the least compressive stress.
2. The ratio of shear to opening of the dike is sufficiently small.
3. The dike-normal external stress is small if compared to the rock tensile strength.

The last point is particularly crucial, in that lithostatic stresses increase with

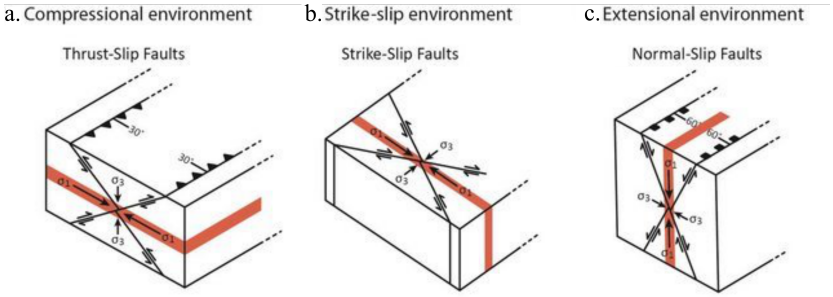

Figure 2.4: **a-c** Fundamental fault modes with their stress tensors compared to the orientation of magmatic intrusions following the same stress tensor (in red). Modified from Le Corvec (2013).

depth and therefore make it very difficult for a dike emerging from the mid to lower crust to follow pre-existing faults (Ziv et al. 2000).

2.4 Dike pathways and vent location

2.4.1 Loadings

Understanding the behaviour of propagating dikes is crucial to better comprehend magma migration through the crust and to improve our ability to forecast the location of vents opening to the surface. Numerical and analog models of fluid-filled fractures have been able to shed considerable light upon the different factors influencing dike propagation.

Dahm (2000) numerically addressed the problem in inhomogeneous media and stress fields using a BEM approach. He found that the growth and propagation of fluid-filled fractures is controlled by internal fluid pressures, external elastic stresses and the fracture toughness of the rock. When a negative density difference between the fluid and the rock is considered, the upward lithostatic stress decrease in the rock is larger than the hydrostatic stress decrease in the fluid, resulting in fracture propagation towards the surface. This is often referred to as a *buoyancy effect*. If the effects of a topographic load are considered, a rotation of the principal stresses is expected, therefore influencing dike trajectories and fluid accumulation. Dikes originating at depth are found to propagate towards the centre of the topographic load (figure 2.5), which can in turn prevent them from reaching the surface, if tectonic stresses are not considered.

Watanabe et al. (2002) conducted a series of analog experiments in order to study the competition between the external stress and the fluid excess pressure in controlling the propagation direction of fluid-filled fractures. This was obtained by systematically changing the external loading and the liquid excess pressure for silicon oil filled fractures in gelatin. They found that dikes tend to propagate by progressively changing their orientation to make it perpendic-

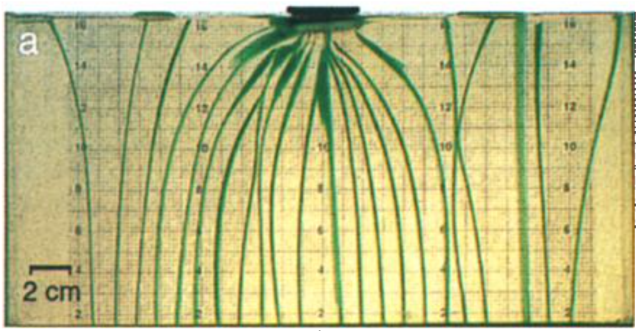

Figure 2.5: Effect of surface loadings on the trajectories of air-filled dikes (dyed in green) in a gelatin experiment conducted by Muller et al. (2001) to simulate the propagation of dikes in a 2-D elastic half-space. Image taken from Muller et al. (2001).

ular to the least compressive stress σ_3. The magnitude of trajectory deflection is larger for smaller ratios of the average excess pressure to the load per unit area. Also, a crack is found to arrest its ascent at a deeper depth for larger loads. Maccaferri et al. (2019) used numerical and analog models to revise and improve the results of Watanabe et al. (2002). They addressed the role of crack length on the propagation paths of dikes in the presence of an external heterogeneous stress field, finding that longer fluid-filled cracks are less sensitive to the background stress for a given ratio between external stress and fluid pressure.

2.4.2 Unloadings

Surface loadings are therefore able to influence dike trajectories by rotating the principal stresses in a half-space. This is also true for negative loadings (that is *unloadings*), which will affect dike propagation in an opposite way. Hooper et al. (2011) found that the unloading stress changes associated with the retreat of ice caps can alter the capacity for storing magma in the crust. They used a numerical model to simulate the opening of a dike in order to evaluate the effect of ice load decrease on magma storage at the Kverkfjöll volcanic system, Iceland. They found that the retreat of ice caps can either encourage or discourage eruptive activity, depending on the orientation of the dikes that carry magma from depth. In the case of the Kverkfjöll system, this resulted in enhanced capture of magma within the crust. The effect of crustal unloading on dike propagation has been investigated by Maccaferri et al. (2014) to explain off-axis volcanism in rifted areas. They found that for sufficiently high values of rift depth fractures coming from depth tend to be deflected by the unloading-induced stress field and to direct themselves towards the flanks of the unloaded zone. Corbi et al. (2015) developed numerical models to show the importance of the unloading effect of caldera formation in determining the total stress budget of a volcano, explaining the peculiar pattern of circumferential and radial fissures

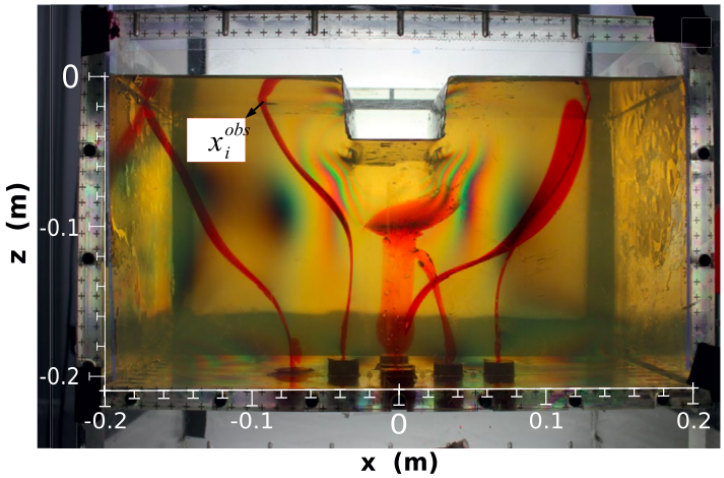

Figure 2.6: Front view of the gelatin box at the conclusion of one of the experiments conducted by Mantiloni et al. (2021). Crack trajectories are marked post-intrusion with red ink. Modified from Mantiloni et al. (2021).

at Fernandina, Galápagos. They concluded that the competition of caldera decompression, magma buoyancy forces and tectonic stresses controls not only the development of the fissures but also the formation of shallow systems of stacked sills. Similar results were obtained by Gaete et al. (2019), who used analog experiments to assess the impact of unloading stresses on post-caldera magma intrusions. They found that the unloaded stress field from a caldera can be responsible for the divergence of vertically ascending dikes, resulting in circumferential dikes and cone sheets. Mantiloni et al. (2021) arranged an analog unloading setup by excavating the surface of a gelatin block with the same geometry of the one I will use in this work. They found that fractures coming from depth tend to be deflected by the unloading-induced stress field and to direct themselves towards the flanks of the unloaded zone (figure 2.6). They also developed a statistical-mechanical strategy in order to forecast the surface arrivals of ascending dikes.

2.4.3 The "stress barrier" under rift basins

As I have already pointed out, the classical definition of rifting implies the formation of a symmetrical subsiding wedge that constitutes the rift depression. As a first order approximation, Maccaferri et al. (2014) assume that the border faults of the basin are perfectly vertical (that is their dip is 90°) so that a rectangular cross section can be considered. This is justified by the high steepness of border faults observed in rift zones, as described in section 1.4. Also, the substantial difference between basin length and width that usually characterizes rift depressions suggests that a plane strain approximation should be

suitable, as long as the considerations are limited to the central branch of the basin. Consider a symmetrical rift basin of width W and depth D as shown in figure 1.4. The problem therefore reduces to finding the stress field induced in an elastic half-space by an infinite strip unloading acting on its free surface. From Jaeger et al. (2009):

$$\sigma_{zz} = \frac{P}{\pi}[(\theta_1 - \theta_2) - \sin(\theta_1 - \theta_2)\cos(\theta_1 + \theta_2)] \tag{2.4}$$

$$\sigma_{xx} = \frac{P}{\pi}[(\theta_1 - \theta_2) + \sin(\theta_1 - \theta_2)\cos(\theta_1 + \theta_2)] \tag{2.5}$$

$$\sigma_{xz} = \frac{P}{\pi}[\sin(\theta_1 - \theta_2)\sin(\theta_1 + \theta_2)] \tag{2.6}$$

where θ_1 and θ_2 are shown in figure 2.7 and $P = \rho g D$ is the unloading pressure due to crustal unloading[3]. All the principal symbols employed in these chapters are summarized in table 3.1, along with their definition and unit of measure. A graphic visualization of equations 2.4 is provided as a two-dimensional contour in appendix A.

Maccaferri et al. (2014) showed that when a horizontal tectonic tensile stress σ_{tec} is superimposed, the direction of the least compressive eigenvalue σ_3 becomes vertical for certain values of depth corresponding to the unloading pressure dominating over the tectonic stretching. This happens when $K = \frac{\pi}{2}\frac{\sigma_{tec}}{P} < 1$. Mathematically, this condition is expressed by noting that the shear stresses vanish in $x = 0$ and therefore imposing

$$\sigma_{zz}(x = 0, z) > \sigma_{xx}(x = 0, z) + \sigma_{tec}. \tag{2.7}$$

Solving for z leads to

$$z_1 < z < z_2 \tag{2.8}$$

where

$$z_1 = \frac{W}{2}\frac{1 - \sqrt{1 - K^2}}{K} \tag{2.9}$$

$$z_2 = \frac{W}{2}\frac{1 + \sqrt{1 - K^2}}{K}. \tag{2.10}$$

Maccaferri et al. (2014) refer to the region between z_1 and z_2 as the "stress barrier" (when existing) and call z_1 and z_2 its lower and upper limits, respectively. They found that the relative position of the stress barrier and the depth z_{in} at which dikes nucleate determines three different scenarios for their propagation and for the final surface distribution of magmatism, as shown in figure 2.8. If $z_{in} < z_1$ dikes ascend subvertically causing in-rift volcanism. When $z_1 < z_{in} < z_2$ the model predicts off-rift volcanism and sill formation, depending on the initial distance of the dikes from the rift axis. Lastly, if $z_{in} > z_2$

[3]Note that a compressive-negative/tensile-positive sign convention is used for stresses.

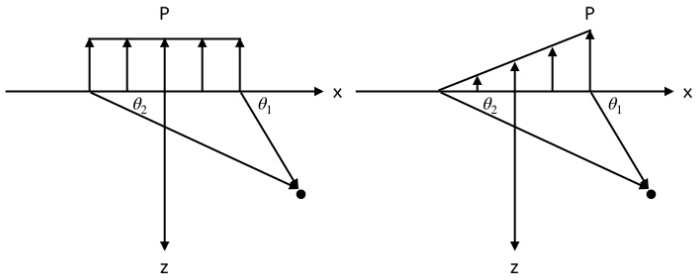

Figure 2.7: Unloading geometries used in sections 3.2 and 3.3. These are analogous to those provided by Jaeger et al. (2009) but arrows point upwards, representing unloading.

dykes are deflected towards the rift sides, resulting in off-rift volcanism without sill formation.

Here I will start from these results to investigate the temporal evolution of magma pathways and vent locations as controlled by a progressive surface unloading, meant to simulate the deepening of a rift basin with time.

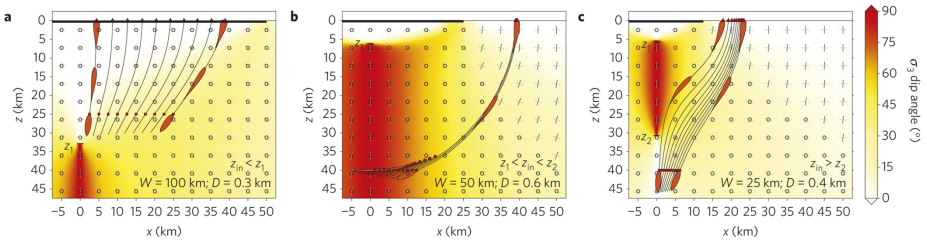

Figure 2.8: Dike trajectories for z_{in} above (a), within (b) and below (c) the stress barrier zone. Red squares indicate the upper tip of the dyke at injection, red circles indicate that a dyke has been arrested as sill, red triangles indicate the position of the arrival at the surface. Black and grey segments show the directions of σ_1 and σ_3 respectively (a circle indicates direction perpendicular to the page) for three nominal sets of graben width, W and depth, D, (see insets). The dip angle of σ_3 is colour-shaded. A tectonic uniform tensile stress of $\sigma_{tec} = 5\,\mathrm{MPa}$ is superimposed to the unloading stresses. From Maccaferri et al. (2014).

Chapter 3

The evolution of rift-related volcanism

Rift zones are often areas of intense and distributed volcanism, due to lithospheric thinning associated with the extensional forces at the base of rifting (chapter 1). It is now clear that most volcanic eruptions are fed by dikes propagating through the crust, where elastic stresses serve as major guidelines to set up their trajectories (chapter 2). It is therefore expected that rift architecture should play an important role in influencing magma propagation and eruption, rifts being zones of substantial crustal unloading. However, the spatial and temporal distribution of volcanic activity and their connection with the physical mechanisms that allow magma propagation have been poorly investigated.

In this chapter I seek to show how the progressive crustal unloading due to rift basin subsidence modifies the stress field in the crust and therefore magma propagation, affecting the surface distribution of volcanism through time. To do so, I will start from the results obtained by Maccaferri et al. (2014) and extend them to account for temporal variability and a different geometry, namely that of a half-graben. In chapter 4 I will eventually upgrade the BEM code employed by Maccaferri et al. (2014) to let propagating dikes interact with previously emplaced ones through their stress field and with erupted ones through the application of superficial loads, simulating deposited magma.

3.1 The elasticity assumption

In this chapter the continental crust will be assumed to behave completely elastically, so that the stresses generated in it by the unloading pressure will be maintained unchanged for the times required for rifting initiation. However, the Earth's crust does not exhibit a uniform rheology throughout its thickness, and an elastic-brittle behaviour is only limited to the upper crust. Below that layer, a time dependent rheology is expected, as temperatures increase with depth and rocks become accordingly more ductile. The precise layering of the lithosphere

Symbol	Definition	Unit of measure
P	unloading pressure	Pa
ρ	rock density	kg m^3
D	rift depth	m
W	rift width	m
b	rift half-width	m
g	gravity acceleration	m s^{-2}
σ_{tec}	tectonic stress	Pa
z_1	stress barrier upper limit	m
z_2	stress barrier lower limit	m
t	time	y
α	deepening rate	m y^{-1}
σ_1	most compressive principal stress	Pa
σ_3	least compressive principal stress	Pa
K	stress parameter	

Table 3.1: Symbols, definitions and units of measure of the parameters employed in the work.

remains however difficult to assess. Common models of lithospheric rheology are usually end-member cases of more complex situations, for lithospheric strength strongly differ as a function of the age, composition, temperature and strain rate of a region (Bürgmann & Dresen 2008). However, although a visco-elastic rheology would be a much better approximation of the behaviour of the lower crust, a full elastic assumption will be employed in this work.

This assumption is not completely unrealistic. Seismic evidence is provided that a strong mid-lower crust is present below young rifts (Déverchère et al. 2001, Craig et al. 2011), allowing stresses to be maintained for longer periods. This is also proven by the presence of a tens of millions of years lasting topography, which implies the existence of a high rigidity layer for the same timespan (Turcotte 1979). Moreover, relaxation of rock primarily occurs in shear (Segall 2010), so that normal stresses are easily preserved through time. This would include the horizontal tectonic stresses σ_{tec}.

3.2 The full-graben case

3.2.1 Modelling basin geometry

Before diving into more detailed simulations for the cases at issue, I will first address the problem in a simplified way from an analytical standpoint. I seek to investigate how z_1 and z_2 evolve with respect to time if a deepening rift basin is considered. For simplicity, I will make some assumptions:

1. the rift deepens at a constant deepening rate α, so that the depth of the basin D will evolve as $D = \alpha t$;

2. the width W of the basin remains constant throughout the rifting process;
3. rift topography and dike shape can be modelled through a plane strain approximation.

A few words are needed about these assumptions. First, care must be taken when modelling the deepening rate. In this model, subsidence of the rift basin is only due faulting (that is thermal effects are neglected) so that the deepening rate α is for all intents the slip rate of the border faults. Regardless of whether such slip occurs by stick-slip or by creeping, I am considering the long-term evolution of the stress field. Second, I am only considering time variations in rift depth and ignoring changes in width. In reality, basins do not only get deeper but also slighlty wider as rifting goes on, so that more realistic effects can be predicted by looking at how z_1 and z_2 change for different rift widths. This is in fact shown for all of my results. Lastly, though a plane strain approximation is justified by the aspect ratios of rifts and dikes, this will prevent my results from describing along-axis dike propagation and the effect of the far ends of the rift. A 3-D extension of this model would be needed to investigate these circumstances.

3.2.2 Time evolution of the stress barrier

Substituting $D = \alpha t$ in the expression for P and then in that of K leads to time dependent equations for z_1 and z_2

$$z_1 = -\frac{W}{\pi}\frac{\rho g \alpha t}{\sigma_{tec}}\left(1 - \sqrt{1 - (\frac{\pi}{2}\frac{\sigma_{tec}}{\rho g \alpha t})^2}\right) \tag{3.1}$$

$$z_2 = -\frac{W}{\pi}\frac{\rho g \alpha t}{\sigma_{tec}}\left(1 - \sqrt{1 + (\frac{\pi}{2}\frac{\sigma_{tec}}{\rho g \alpha t})^2}\right) \tag{3.2}$$

that are plotted in figure 3.1 for $W = 25\,\text{km}$. Some considerations about this figure are required before diving into a more general plot for equations 3.1 and 3.2.

The time evolution of z_1 and z_2 is shown in figure 3.1 for a 25 km wide rift deepening at a rate of $\alpha = 0.001\,\text{m/y}$. As the time spans from $t = 0$ to $t = 2\,\text{My}$, the basin depth increases from 0 to 2 km, and the two variables are therefore shown on the same horizontal axis. The depth at which the upper and lower limit of the stress barrier can be found is read on the vertical axis. The straight line extending from $t = 0$ to approximately $t = 0.3\,\text{My}$ comes from the terms under square root in equations 3.1 and 3.2 being negative, so that the real parts of z_1 and z_2 coincide up to that point. Along the straight line the unloading pressure P is not large enough to compete with the constant tectonic stresses σ_{tec}, but it grows with time to eventually overcome it at approximately $t = 0.3\,\text{My}$, where the line bifurcates and the stress barrier is formed. Let me call the time instant at which this happens t_c. The upward and downward branch therefore represent z_1 and z_2, respectively. Note how z_2 extends way beyond the vertical dimension of the Earth's crust, making a large part of figure

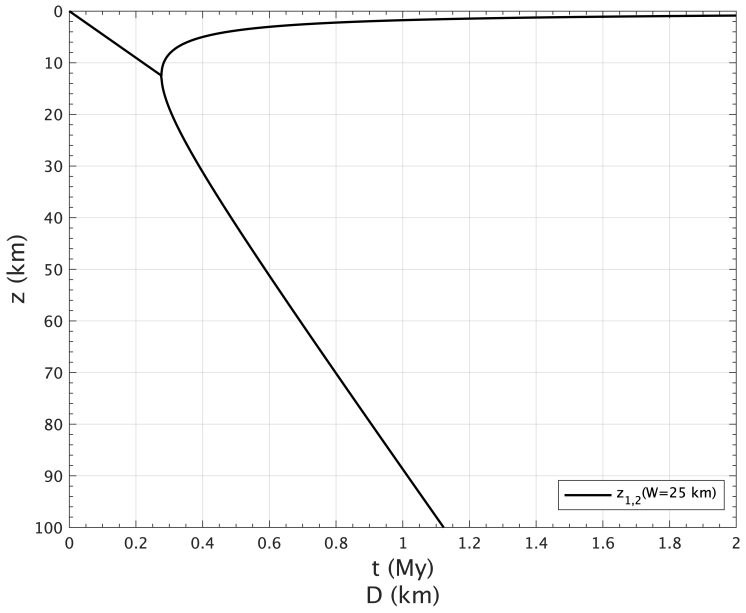

Figure 3.1: z_1 and z_2 for a full-graben deepening at a rate of $\alpha = 0.001\,\mathrm{m/y}$ plotted with respect to time for $W = 25$. See section 3.2.1 for further description.

3.1 meaningless with respect to our dissertation. In this respect, I can introduce the parameter z_{moho} to account for the depth of the Mohorovičić discontinuity between the crust and the mantle and set it to a realistic value of $z_{moho} = 40\,\mathrm{km}$. This will also serve as the depth of dike injection for most of my simulations.

The time evolution of z_1 and z_2 is shown in figure 3.2 for different rift widths, namely $W = 25$, 50, 100 and 300 km. Recall from figure 3.1 that the stress barrier does not form until $t = t_c$, so that the region $0 < t < t_c$ does not provide us any information. Hence it has been patched in red in figure 3.2, along with the region $z > z_{moho}$, which in turn has been patched in blue. It is evident from figure 3.2 that t_c is independent from rift width, and it only depends on the ratio between σ_{tec} and P, as equations 3.1 and 3.2 clearly show. On the other hand, rift width strongly influences the depth at which the barrier is formed, along with the rate at which z_1 and z_2 decrease and increase, respectively. This results in wider basins having a deeper barrier for a given time or basin depth.

The evolution of z_1 and z_2 and the limits imposed by t_c and z_{moho} have strong implications for the propagation of dikes from depth to the surface. It is known from Anderson (1972) that dikes tend to open and propagate roughly perpendicularly to the direction of the least compressive eigenvalue σ_3, and the latter being vertical between z_1 and z_2 implies the existence of a stress barrier under the rift (section 2.4.3). This will affect dike propagation in a number of ways depending on the relative position of the stress barrier and the injection

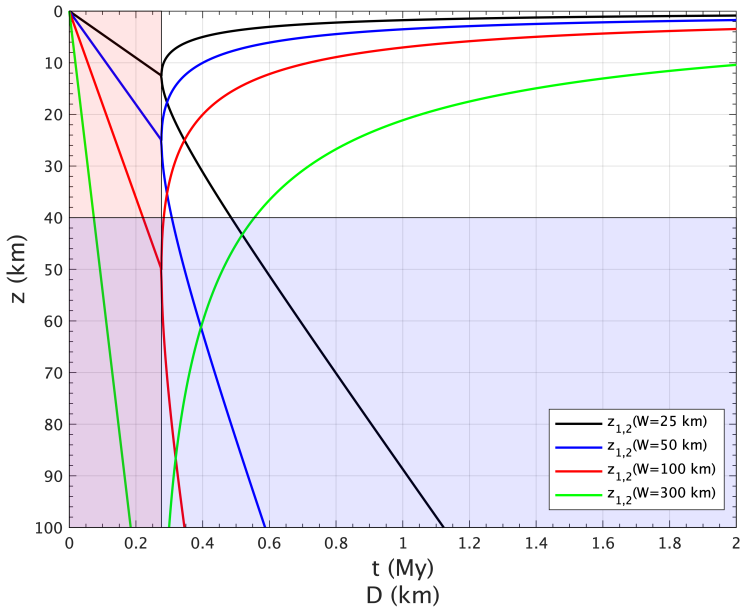

Figure 3.2: z_1 and z_2 for a full-graben deepening at a rate of $\alpha = 0.001\,\mathrm{m/y}$ plotted with respect to time for $W = 25$, 50, 100 and 300 km. See section 3.2.1 for further description.

depth. For my purposes, let me assume a constant injection depth and set it equal to the Mohorovičić discontinuity depth z_{moho}, so that the relative position will only change due to the evolution of the stress barrier. Graphically, this can be understood by moving along the horizontal line $z = z_{moho}$ in figure 3.2 and looking up to see whether two branches of the stress barrier are encountered, just one or none of them, for each width curve. These three cases will be described in detail in the next section.

3.2.3 Analysis of dike trajectories

I am now in a position to apply the time evolution of the stress barrier described in section 3.2.1 to the propagation of dikes through the lithosphere. As mentioned before, I will assume that the injection depth will be constant with time and equal to the depth of the Moho z_{moho}. With regards to dike propagation, I will make use for now of the results of Anderson (1972) and assume that the trajectories will be roughly perpendicular to the direction of least compressive eigenvalue σ_3. This assumption will eventually be dropped in chapter 4, where a boundary element code will be employed to assess the role of dike interaction in the distribution of volcanism.

Dike trajectories are influenced by the location and magnitude of the stress barrier, as shown in figure 3.3 for a $W = 25$ km wide rift at three different time

instants or basin depths. When the rift is only $D = 100\,\text{m}$ deep (figure 3.3, top panel) the stress barrier has not formed yet and dikes follow sub-vertical trajectories that result in in-rift eruptions. Given that surface eruptions (colored triangles in figure 3.3) are predicted to be scattered across the basin, a monogenetic type of volcanism would be expected for this configuration. As time evolves the rift gets deeper and the stress barrier develops. When the rift is $D = 400\,\text{m}$ deep (figure 3.3, middle panel), the stress barrier is fully included in the domain and ascending dikes are deflected by it as they approach z_2. This results in off-rift surface volcanism, as shown by the red triangles in figure 3.3. Lighter colors (yellow, orange) represent previous eruptions. Notice how the presence of the stress barrier results in focusing the volcanism in narrow regions flanking the rift. This effect increases with growing intensity and extension of the barrier. When $z_2 > z_{moho}$ dikes are injected from inside the stress barrier (figure 3.3, bottom panel). This is in fact the most representative case of the three, in that z_2 overcomes the depth of injection for most of a rift's lifetime, as figure 3.2 clearly shows. Care should be taken when dealing with this particular configuration. Maccaferri et al. (2014) showed that for typical rock-magma density differences dikes injected very close to the symmetry axis of the stress barrier do not have enough buoyancy to make their way to the surface and might get stuck as sub-horizontal sills in the vicinity of their injection site. This is not evident in the approximation of figure 3.3, where dikes are assumed to indifferently propagate perpendicularly to σ_3. However, it will eventually be shown in chapter 4.

Similar results occur for a $W = 50\,\text{km}$ and a $W = 100\,\text{km}$ wide rift (figures 3.4 and 3.5, respectively). Although sharing the same general traits with the $W = 25\,\text{km}$ wide rift, these plots clearly show how the wider the rift, the shorter the timespan where $0 < z_1 < z_2 < z_{moho}$, making it already null at around $W = 100\,\text{km}$. This is due to the stress barrier formation depth and derivative of $z(t)$ being proportional to the rift width, eventually resulting in very wide rifts being characterized by a prolonged period of in-rift volcanism (green line in figure 3.2). Moreover, note how off-rift eruptions tend to concentrate closer to the basin as its width increases. This will in fact be better investigated and discussed in section 3.4.1.

3.3 The half-graben case

3.3.1 Unloading formulas

As I have discussed in section 1.4, the fundamental rift unit is better represented by a half-graben rather than by a graben. It is straightforward to adapt the full-graben model to a half-graben by considering the stresses induced by a load shaped as a right triangle (Jaeger et al. 2009):

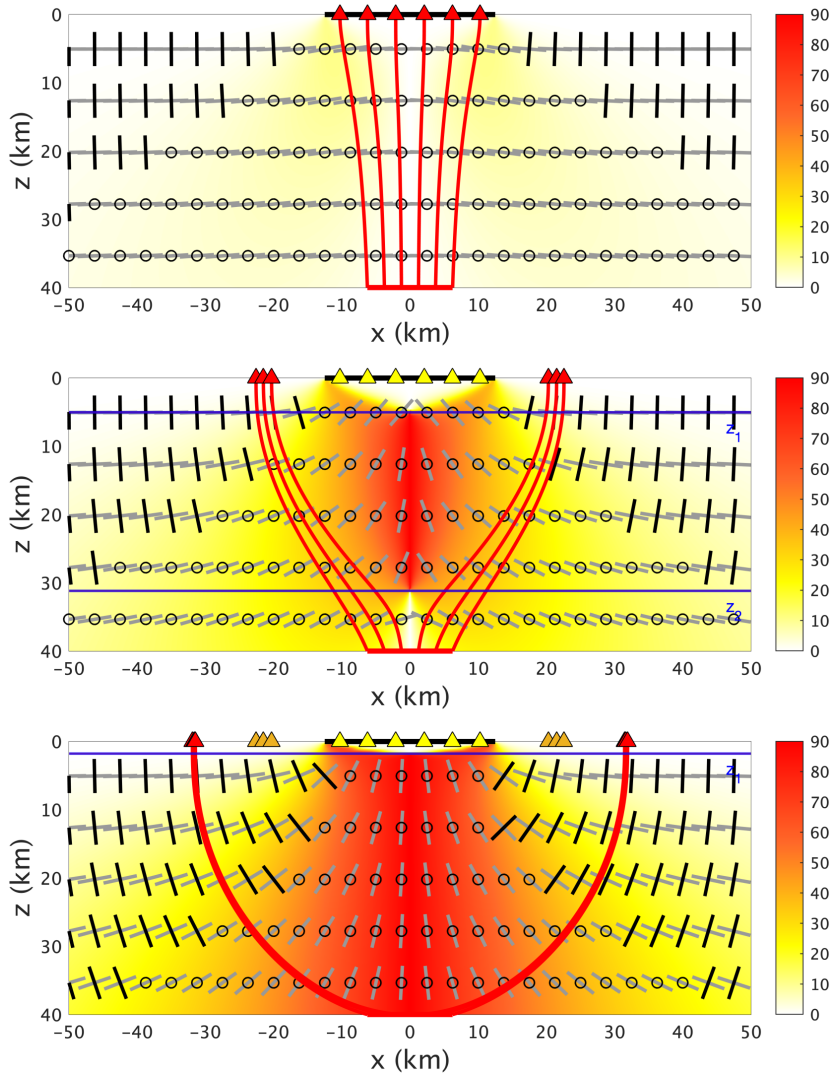

Figure 3.3: Dike trajectories and surface volcanism in a $W = 25\,\text{km}$ wide full-graben for three different basin depths (from top to bottom: 100 m, 400 m and 1 km). A uniform horizontal tensional stress $\sigma_{tec} = 5\,\text{MPa}$ is superimposed to the unloading stresses. Horizontal blue lines represent the upper and lower limits of the stress barrier. Black and grey segments in the background indicate the directions of σ_1 and σ_3, respectively. Colormap and relative colorbar show the dip angle of σ_3. Black bold line at $z = 0\,\text{km}$ represents the location of the rift. Red bold line at $z = 40\,\text{km}$ represents the magma ponding zone. See section 3.2.3 for further description.

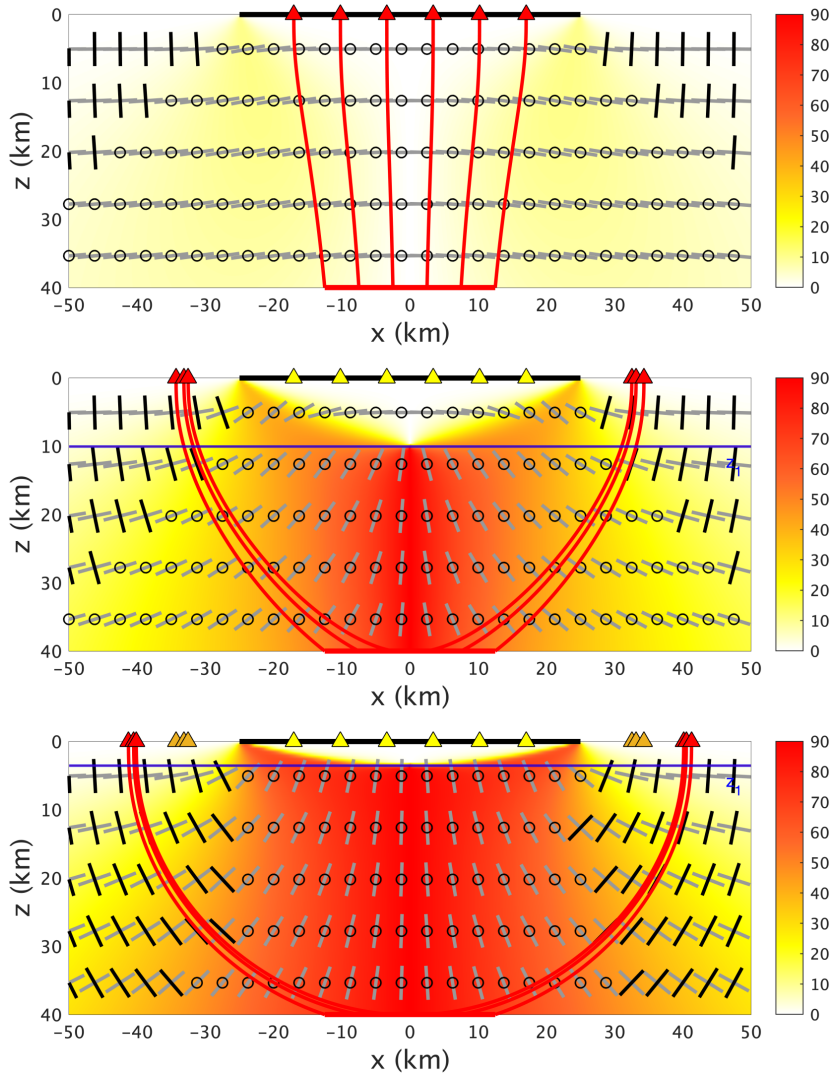

Figure 3.4: Dike trajectories and surface volcanism in a $W = 50\,\text{km}$ wide full-graben for three different basin depths (from top to bottom: 100 m, 400 m and 1 km). A uniform horizontal tensional stress $\sigma_{tec} = 5\,\text{MPa}$ is superimposed to the unloading stresses. Horizontal blue lines represent the upper and lower limits of the stress barrier. Black and grey segments in the background indicate the directions of σ_1 and σ_3, respectively. Colormap and relative colorbar show the dip angle of σ_3. Black bold line at $z = 0\,\text{km}$ represents the location of the rift. Red bold line at $z = 40\,\text{km}$ represents the magma ponding zone. See section 3.2.3 for further description.

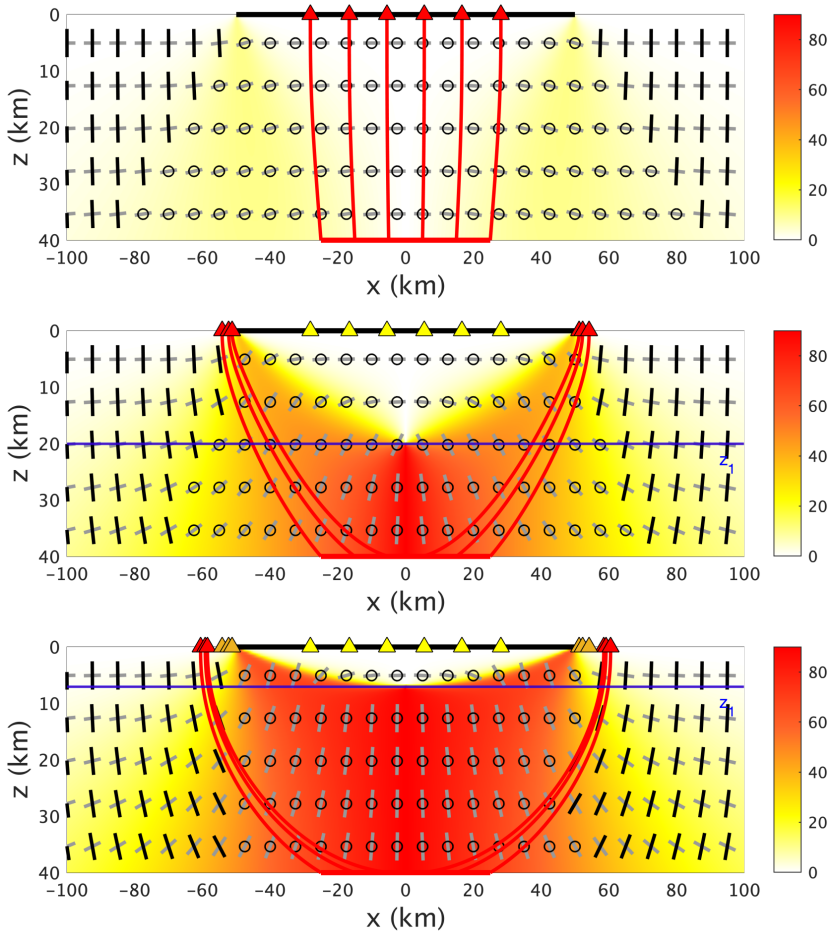

Figure 3.5: Dike trajectories and surface volcanism in a $W = 100\,\text{km}$ wide full-graben for three different basin depths (from top to bottom: 100 m, 400 m and 1 km). A uniform horizontal tensional stress $\sigma_{tec} = 5\,\text{MPa}$ is superimposed to the unloading stresses. Horizontal blue lines represent the upper and lower limits of the stress barrier. Black and grey segments in the background indicate the directions of σ_1 and σ_3, respectively. Colormap and relative colorbar show the dip angle of σ_3. Black bold line at $z = 0\,\text{km}$ represents the location of the rift. Red bold line at $z = 40\,\text{km}$ represents the magma ponding zone. See section 3.2.3 for further description.

$$\sigma_{zz} = \frac{P}{2\pi}\{[1 + (x/b)](\theta_1 - \theta_2) - \sin(2\theta_1)\} \tag{3.3}$$

$$\sigma_{xx} = \frac{P}{2\pi}\{[1 + (x/b)](\theta_1 - \theta_2) + \sin(2\theta_1) - (2z/b)\ln(r_2/r_1)\} \tag{3.4}$$

$$\sigma_{xz} = \frac{P}{2\pi}\{1 - (z/b)(\theta_1 - \theta_2) + \cos(2\theta_1)\} \tag{3.5}$$

where r_1, r_2, θ_1 and θ_2 are shown in figure 2.7. Equation 3.5 is actually a corrected form of that provided by Jaeger et al. (2009). Their equation and the validation of 3.5 are given in appendix B. A graphic visualization of equations 3.3 is provided as a two-dimensional contour in appendix A.

3.3.2 Stress barrier

Following the procedure outlined by Maccaferri et al. (2014) and recalled in section 3.2 for the full-graben case, I seek to find the region where the shear stresses σ_{xz} vanish, imposing

$$1 - (z/b)(\theta_1 - \theta_2) + \cos(2\theta_1) = 0. \tag{3.6}$$

The equation was solved numerically for a series of equally spaced z-coordinates. The x-coordinates satisfying equation 3.6 for those z-coordinates will be referred to as $x_0(z)$. Next, I checked whether

$$\sigma_{zz}(x_0(z), z) > \sigma_{xx}(x_0(z), z) + \sigma_{tec}. \tag{3.7}$$

The z-coordinates satisfying equation 3.7 for a given set of P, W and σ_{tec} will constitute a region of the half-space where σ_3 is vertical, which we will refer to as the "stress barrier" for the half-graben case. z_1 and z_2 are therefore found by looking for the minimum and maximum value of z for which equation 3.7 is solved.

3.3.3 Time evolution of the stress barrier

By plotting z_1 and z_2 for regularly increasing values of P I found that the stress barrier below the half-graben generates later and at shallower depth if compared to the full-graben, for a given deepening rate α (figure 3.6). The first of these differences has obviously the effect of extending the period of time during which there is no stress barrier, promoting a longer phase of monogenetic scattered volcanism inside the rift basin. The second difference, in turn, results in prolonging the time (and depth) interval for which $z_1 < z_2 < z_{moho}$, favoring dike ascent and reducing the likelihood of sill formation.

It should be pointed out, however, that despite the similarities between figures 3.2 and 3.6, the geometry and therefore the effects of the stress barrier for the half-graben case are mainly influenced by the asymmetry of the unloading, resulting in a much more different dike behavior than for the full-graben case. This will in fact be highlighted in section 3.3.4.

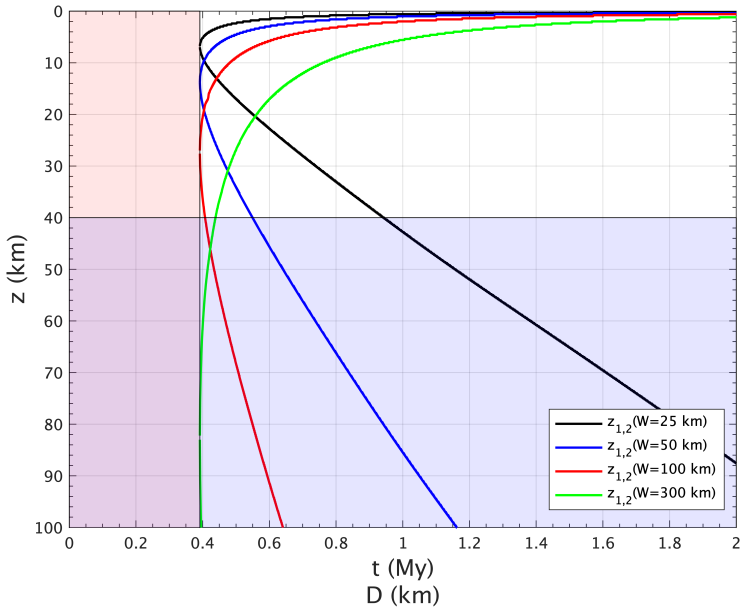

Figure 3.6: z_1 and z_2 for a half-graben deepening at a rate of $\alpha = 0.001\,\mathrm{m/y}$ plotted with respect to time for $W = 25$, 50, 100 and 300 km. See section 3.3.3 for further description.

3.3.4 Analysis of dike trajectories for a half-graben

The half-graben case is more complicated than the full-graben case. The shear stresses σ_{xz} for a rectangular basin are null only for $x = 0$, forcing the stress barrier to be restricted to that coordinate. This results in the principal stresses being symmetrical with respect to the $x = 0$ axis and so for dike trajectories, for our chosen injection geometry. The stress barrier for the half-graben has a different shape, as shown in figure 3.7 for a $W = 25\,\mathrm{km}$ wide rift, where the red shaded area is shifted to the right of $x = 0$ and deflected towards the deeper side of the graben. The main consequence is that dike trajectories are no longer symmetrical with respect to $x = 0$. If we assume that dikes are injected from a horizontal strip of length $W/2$ centered at $x = 0$ (as in the full graben case), this results in more concentrated paths on the negative x direction. The resulting volcanism would therefore tend to focus on the left side of the half-graben, that is its shallowest part. However, this is a random assumption. The spatial distribution of surface volcanism in a half-graben is highly dependent on the horiziontal coordinate at which dikes nucleate: dikes injected from below the shallower side of the basin may still erupt within the rift, while those that form under the deeper side tend to ascend towards the flank. If the magma ponding zone is shifted towards the deeper side more trajectories will come from the right side of the basin, favoring off-rift arrivals (figure 3.10).

As the barrier grows both in extension and intensity, surface volcanism becomes less scattered and tends to concentrate in narrower areas. This effect was also observed in the the full-graben case and will actually result in being amplified when considering dike interactions, as in chapter 4. In this case, however, the presence of the stress barrier does not hinder the possibility of in-rift volcanism on the shallower side of the basin, even for high values of basin depth D.

3.4 Conclusions

3.4.1 Overview

In chapter 3 I focused on investigating the temporal evolution of the stress barrier generated in the crust by the progressive deepening of a symmetrical and an asymmetrical rift basin (figures 3.2 and 3.6), simulated through the application of surface unloadings and horizontal tectonic stresses. I found that the time of emergence of the stress barrier is independent of rift width W, while the latter determines the depth at which the barrier nucleates. I provide now an alternative plot for the same results, as shown in figure 3.11 for both the full and half-graben cases. Here z_1 and z_2 are normalized by the rift width W, along with the depth to the Moho z_{moho}. As a result, the time evolution of the stress barrier reduces to a single curve for all the widths, while the normalized z_{moho} splits into different horizontal lines.

Making use of the time dependence of the stress barrier and the space distribution of principal stresses I have simulated dike propagation from the crust-mantle boundary to the surface, assuming that fractures would open in the direction of the least principal stress σ_3. Surface volcanism is expected to shift from the inside of the rift to its flanks as the basin deepens and the stress barrier intensifies (figure 3.14). This is true for both the full-graben and the half-graben geometries. However, for half-grabens the presence of the stress barrier does not always prevent in-rift volcanism as it would for a full-graben case, even for high values of basin depth D, and this is especially true for wide basins. Moreover, in-rift volcanism is expected to focus on the shallower side of the basin. This is also shown by plotting the outermost dike's x-coordinate of eruption with respect to time (and therefore basin depth D) (figure 3.11). Only the positive arrivals are shown for the full-graben case due to the symmetry of the trajectories. On the other hand, the positive and negative trajectories for the half-graben case behave in a very different way, so they have been shown separately. Note how narrower rifts allow for dikes reaching the surface at more times their half-width than wide rifts, as was already noticeable in figures 3.3, 3.4 and 3.5 and will again be seen in chapter 4. This is due to the Moho being fixed throughout the various simulations while the rift width W changes, rearranging the direction of σ_3 at the injection depth and causing off-rift vents to focus in the proximity of the basin for wide rifts.

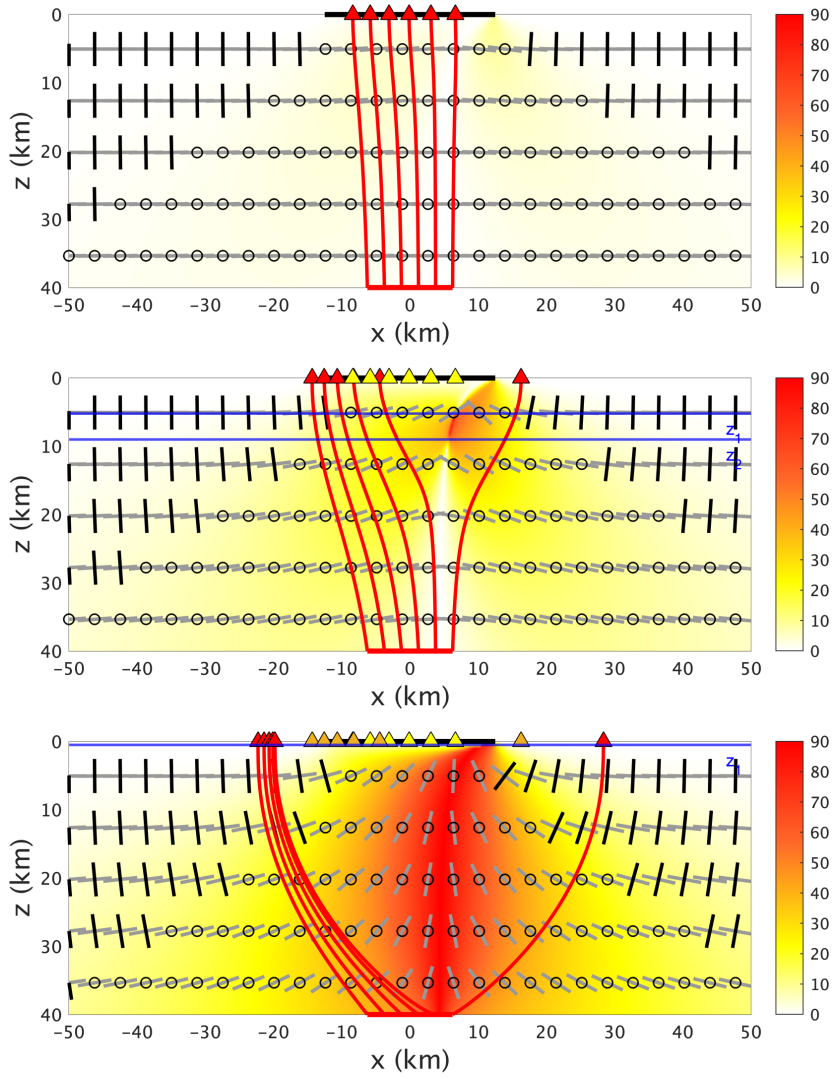

Figure 3.7: Dike trajectories and surface volcanism in a $W = 25\,\text{km}$ wide half-graben for three different basin depths (from top to bottom: 100 m, 400 m and 1 km). A uniform horizontal tensional stress $\sigma_{tec} = 5\,\text{MPa}$ is superimposed to the unloading stresses. Horizontal blue lines represent the upper and lower limits of the stress barrier. Black and grey segments in the background indicate the directions of σ_1 and σ_3, respectively. Colormap and relative colorbar show the dip angle of σ_3. Black bold line at $z = 0\,\text{km}$ represents the location of the rift. Red bold line at $z = 40\,\text{km}$ represents the magma ponding zone. See section 3.3.4 for further description.

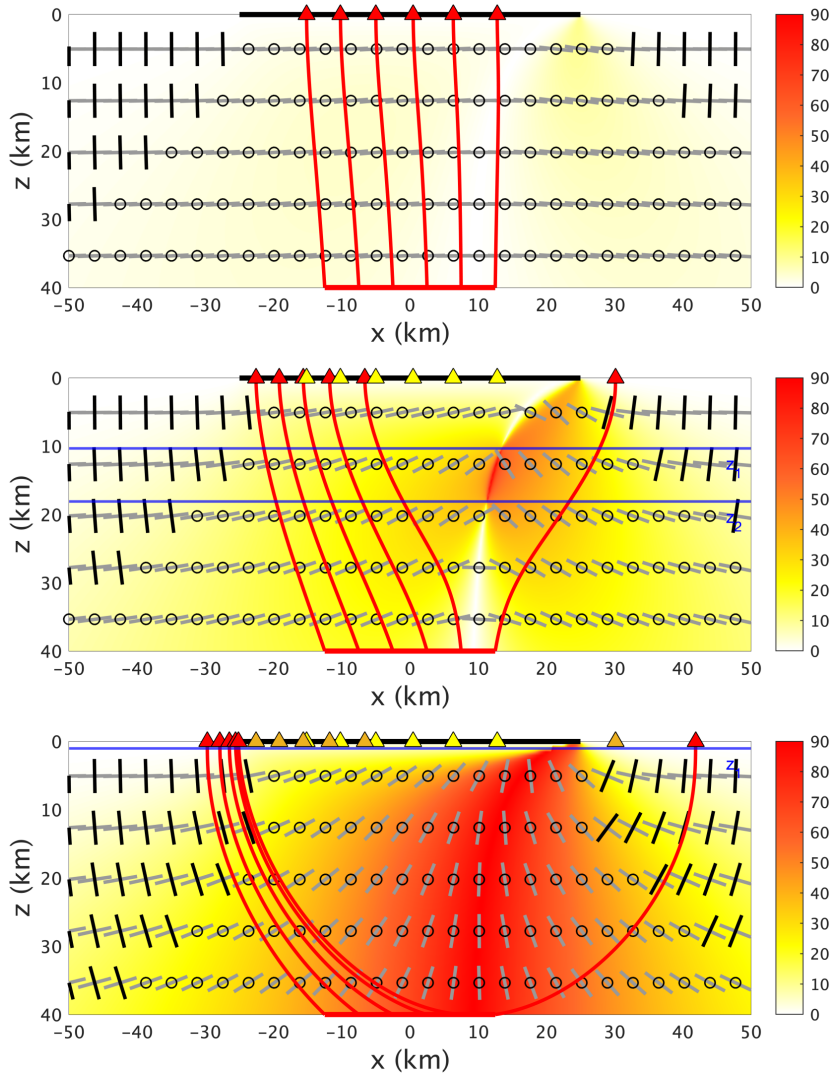

Figure 3.8: Dike trajectories and surface volcanism in a $W = 50\,\text{km}$ wide half-graben for three different basin depths (from top to bottom: 100 m, 400 m and 1 km). A uniform horizontal tensional stress $\sigma_{tec} = 5\,\text{MPa}$ is superimposed to the unloading stresses. Horizontal blue lines represent the upper and lower limits of the stress barrier. Black and grey segments in the background indicate the directions of σ_1 and σ_3, respectively. Colormap and relative colorbar show the dip angle of σ_3. Black bold line at $z = 0\,\text{km}$ represents the location of the rift. Red bold line at $z = 40\,\text{km}$ represents the magma ponding zone. See section 3.3.4 for further description.

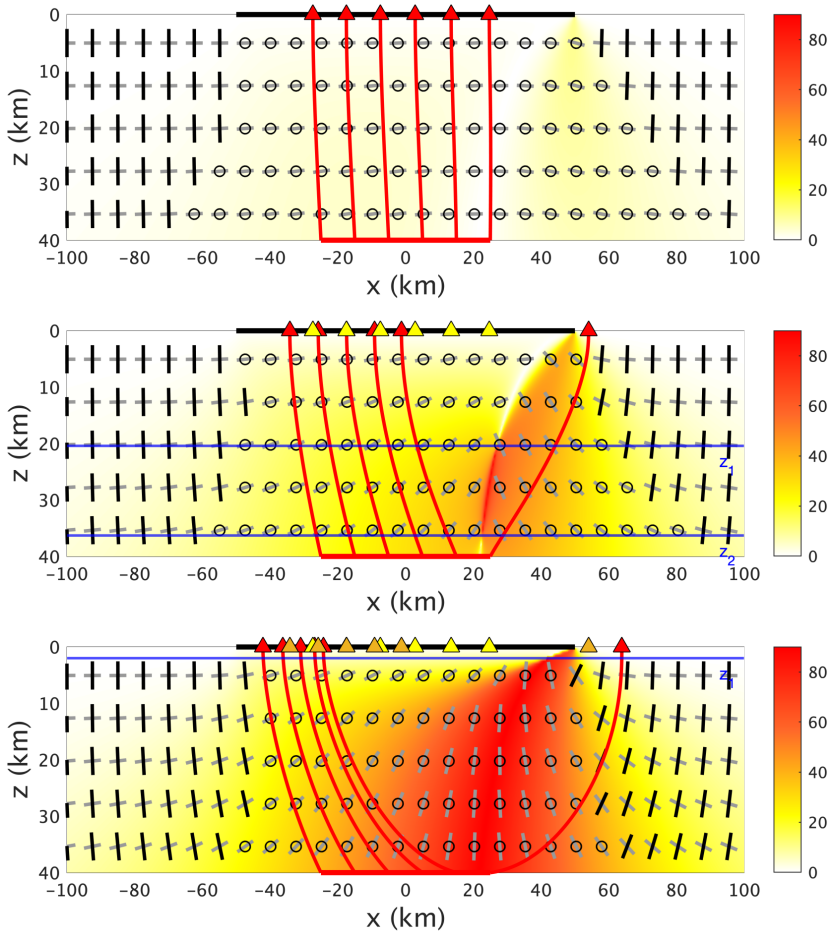

Figure 3.9: Dike trajectories and surface volcanism in a $W = 100\,\text{km}$ wide half-graben for three different basin depths (from top to bottom: 100 m, 400 m and 1 km). A uniform horizontal tensional stress $\sigma_{tec} = 5\,\text{MPa}$ is superimposed to the unloading stresses. Horizontal blue lines represent the upper and lower limits of the stress barrier. Black and grey segments in the background indicate the directions of σ_1 and σ_3, respectively. Colormap and relative colorbar show the dip angle of σ_3. Black bold line at $z = 0\,\text{km}$ represents the location of the rift. Red bold line at $z = 40\,\text{km}$ represents the magma ponding zone. See section 3.3.4 for further description.

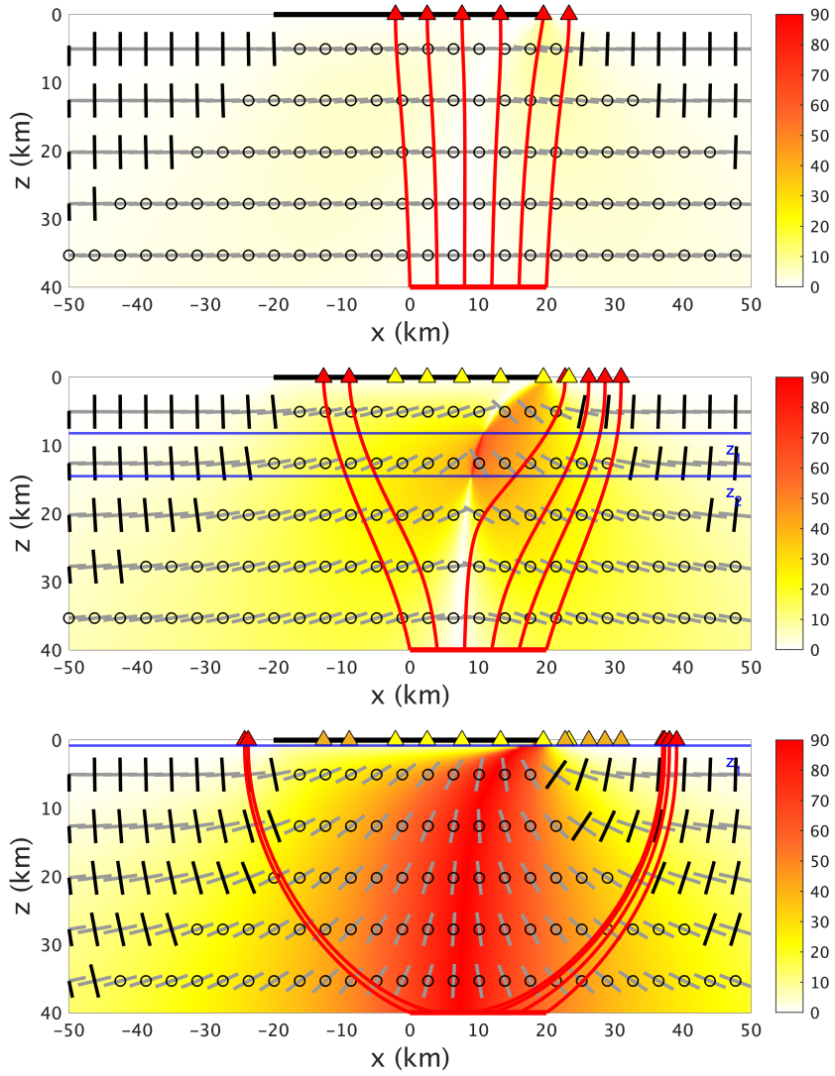

Figure 3.10: Dike trajectories and surface volcanism in a $W = 40\,\text{km}$ wide half-graben for three different basin depths (from top to bottom: 100 m, 400 m and 1 km). A uniform horizontal tensional stress $\sigma_{tec} = 5\,\text{MPa}$ is superimposed to the unloading stresses. Horizontal blue lines represent the upper and lower limits of the stress barrier. Black and grey segments in the background indicate the directions of σ_1 and σ_3, respectively. Colormap and relative colorbar show the dip angle of σ_3. Black bold line at $z = 0\,\text{km}$ represents the location of the rift. Red bold line at $z = 40\,\text{km}$ represents the magma ponding zone. See section 3.3.4 for further description.

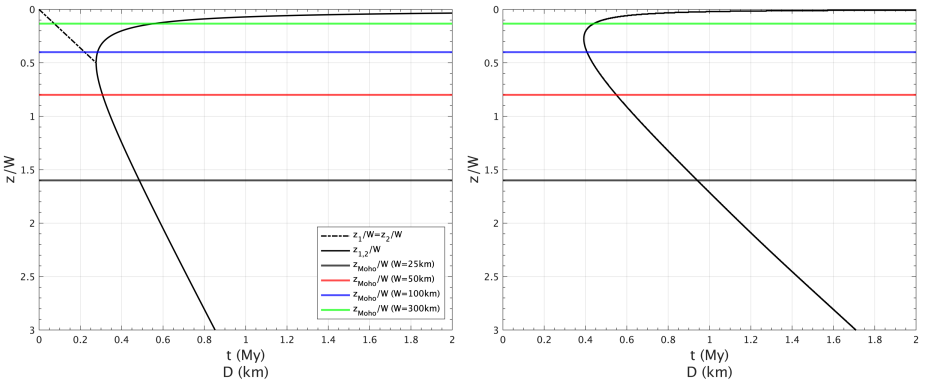

Figure 3.11: z_1/W and z_2/W plotted with respect to time for a full-graben (left panel) and a half-graben (right panel) deepening at a rate of $\alpha = 0.001\,\mathrm{m/y}$. Horizontal colored lines represent z_{Moho}/W for $W = 25$, 50, 100 and 300 km. Legend is valid for both panels. See section 3.4.1 for further description.

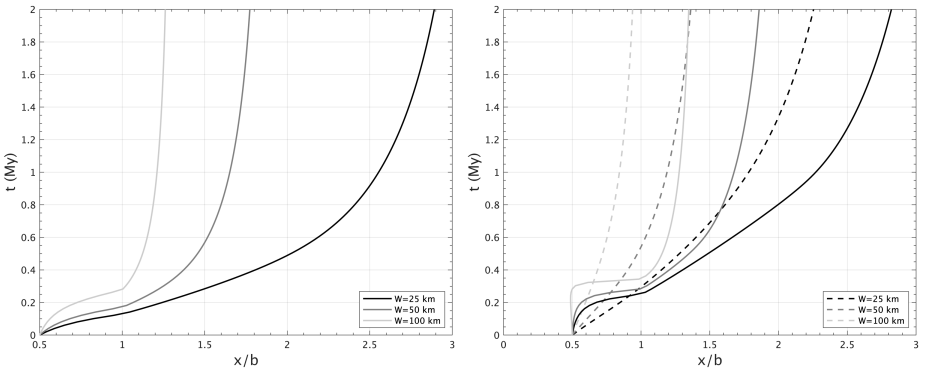

Figure 3.12: Temporal evolution of the horizontal coordinate of eruption for the outermost dikes, for $W = 25$, 50 and 100 km. *Left*: full-graben case. Only the positive values are shown due to the symmetry of the problem. *Right*: half-graben case. Full lines represent positive horizontal coordinates, while dashed lines plot the absolute value of negative coordinates.

3.4.2 Discussion

The results obtained in chapter 3 manage to explain some interesting aspects of volcanism in rifted areas. The migration of surface volcanism from the center of the forming basin to its flanks has been observed in many early rifting environments, such as lake Baikal (Kiselev 1987) and the Kenya rift (Braile et al. 2006). In the latter case, migration of volcanism has also been accompanied by a shift of the basin shape from a half-graben to a full-graben (Braile et al. 2006). For a given depth D, this would imply the formation of a more symmetrical stress barrier, hindering in-rift dike arrivals and favoring off-rift volcanism (sections 3.2.3 and 3.4.1). Michon & Merle (2001) summarized the evolution of the Massif Central rift in terms of the spatio-temporal distribution of its volcanism. They distinguished between three different magmatic periods, namely a pre-rift magmatic event, a rifting event and a major magmatic event. The rift-related magmatic event was spatially connected with the area of high crustal thinning, that is the Limagne graben, and resulted in more than 200 monogenetic scattered volcanoes mainly erupted within the basin. The subsequent major event was characterised by two peaks of volcanism, which contributed to form the Monts Dore and Sancy stratovolcanoes, the Dèves basaltic shield and the Chaine des Puys, all located off-rift with respect to the Limagne graben (figure 3.13). This sequence of events is consistent with the results of this chapter.

On the other hand, evidence is provided of a later migration of volcanism from the flanks to the basin during the advanced stages of rifting (Kiselev 1987, Corti 2009). This phenomenon is sometimes accompanied by the deactivation of border faults and the development of in-rift magma assisted fractures, usually marking the progression of rifting into seafloor spreading (Corti 2009). Clearly, this is not taken into account at this stage of the model. However, some significant considerations can already be made. As rifts progress towards more mature stages they tend to become wider. From figures 3.2 and 3.6 we know that z_1 is deeper for wide rifts, fostering the possibility of magma ascending from above the stress barrier and therefore reaching the surface inside the rift basin. Moreover, as dikes get stuck as horizontal sills below the rift basin due to the intensification of the stress barrier, they may serve as a shallower ponding zone, possibly raising the depth at which magma is injected and enhancing the effect. In order to include some of these features in my model, in the next chapter I will relax the assumption of non-interacting magma trajectories. The new model will include the effect of previously intruded and stalled dikes, as well as the topographic loads created by the eruptions.

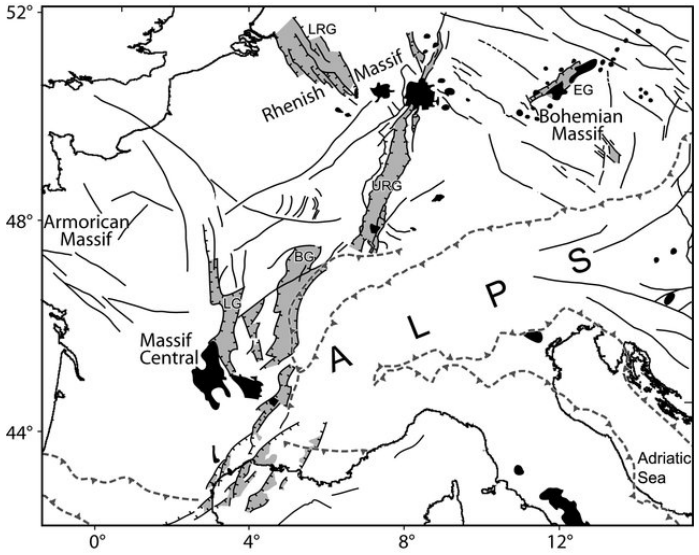

Figure 3.13: Map of the main features of the European Cenozoic rift system in the Alpine and Pyrenean foreland, showing Cenozoic faults (black lines), rift-related sedimentary basins (light gray), and volcanic fields (black). The dashed barbed lines indicate the Alpine deformation front. BG-Bresse Graben; EG-Eger Graben; LG-Limagne Graben; LRG-Lower Rhine Graben; URG-Upper Rhine Graben. The off-rift volcanic fields near the Limagne Graben represent the Chaine des Puys, the Monts Dore and Sancy stratovolcanoes (western side of the basin) and the Dèves basaltic shield (eastern side of the basin). Image taken from Lustrino & Carminati (2007).

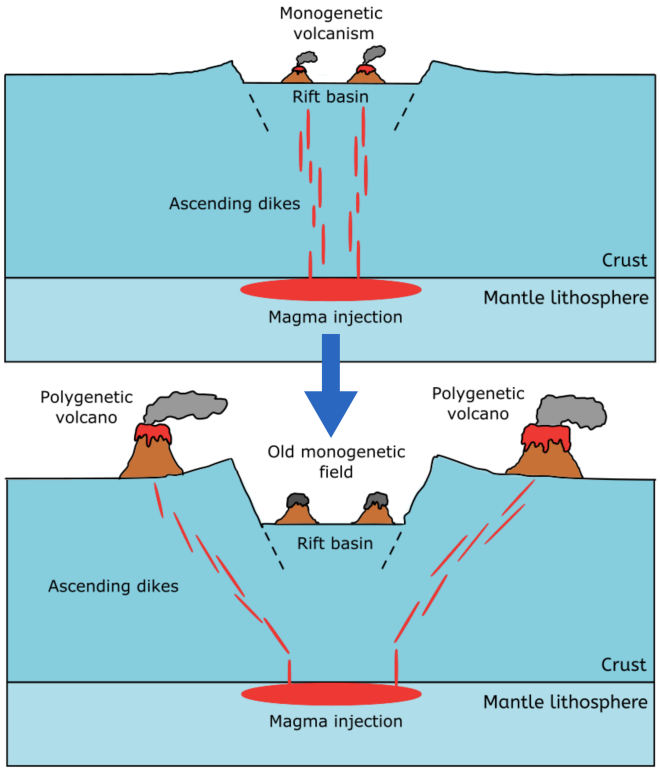

Figure 3.14: Two stages of the evolution of rift-related volcanism, following from the results obtained in chapter 3. *Top*: magma injected from below a shallow rift basin makes its way up to the surface and erupts in scattered in-rift locations, resulting in a monogenetic type of volcanism. *Bottom*: as the basin deepens a stress barrier is formed, causing ascending dikes to be deflected and surface volcanism to focus on the rift flanks. The redistribution of principal stresses below the rift results in closer magma pathways, fostering the formation of polygenetic volcanoes.

Chapter 4

Effects of dike-dike interactions

4.1 The role of dike stresses

The calculations carried out in chapter 3 were based on the assumption that dikes move perpendicularly to the direction of the least compressive eigenvalue σ_3. I will now drop this assumption and make use of the boundary element dike propagation code developed by Maccaferri (2010), Maccaferri et al. (2011) (section 2.3.2). However, some modifications to the code are necessary to adapt it to my need of considering dike-dike interaction. This code simulates fluid-filled fracture propagation by considering dikes as pressurized fractures filled with a buoyant fluid that move in the stress field generated by internal magma excess pressure, tectonic forces and surface loadings, but does not consider the stress perturbations due to the emplacement of previous unerupted dikes, nor the surface loading due to the erupted magma piling up on the surface. In reality, stresses in the vicinity of other fractures can be of great importance in rotating the principal directions, therefore altering the trajectories of subsequent dikes. This is especially true if numerous intrusions accumulate in vast subsurface volumes over time frames of hundreds of thousands of years.

Ito & Martel (2002) used laboratory experiments and numerical models to quantify the effects of dike interaction on the focusing of magma in the upper mantle. They found that two adjacent buoyant dikes will tend to merge as they ascend if they are spaced closely enough. The key parameters controlling the maximum horizontal distance at which interaction takes place are found to be dike driving pressures, dike head lengths and the difference between the principal stresses of the remote stress field.

Kühn & Dahm (2008) investigated dike interaction by adding the effect of dike induced stress fields on the propagation of subsequent dikes to the boundary element code developed by Dahm (2000). They found that ascending fractures behave independently until they approach previously emplaced dikes and their

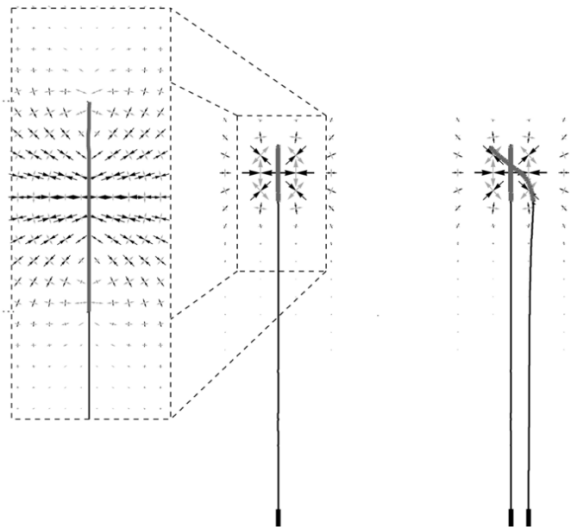

Figure 4.1: Schematic representation of dike-dike interaction. The stress field induced by the emplacement of the first dyke is indicated by arrows (black arrows: principal axis of maximum compression σ_1, light grey arrows: principal axis of least compression σ_3). Modified from Kühn & Dahm (2008).

.

interaction results in focusing and crossing of dikes (figure 4.1), confirming the experimental results of Ito & Martel (2002). This has strong implications concerning the generation of magma chambers and the formation of sheeted dyke complexes. The degree of interaction is found to be dependent on the competition between the pressure in the dike head and horizontal tensional stresses, high values of the latter reducing dike focusing and promoting vertical ascent. Although shedding light on the possible mechanisms that favor or hinder the formation of magma chambers at fast and slow spreading ridges, respectively, Kühn & Dahm (2008) did not take into account the role of superficial loadings to the behaviour of the system.

In this chapter I will combine the two effects by keeping track of the stress field generated by dikes that are emplaced at depth and the loading exerted by those that erupt on the surface, updating the background stress field after each dike simulation.

4.2 Modelling dike interaction

The BEM dike propagation code developed by Maccaferri et al. (2011) and outlined in section 2.3.2 already considers the effects of external stress fields acting on the fracture. It therefore needs to be modified in two ways so that:

1. it stores the stress field generated by intruded dikes;

2. it considers the loading applied by extruded dikes on the surface of the Earth's crust.

The information about the external stress acting in the elastic domain (file name, path, spatial domain and grid step of the input stress file) is contained in one of the input files of the code, called `input_field`, along with parameters related to the output files. Another input file, called `input_BE`, contains parameters defining the geometry of boundary element (BE) crack, the properties of the elastic domain, and the properties of the fluid filling the crack, together with parameters defining the crack propagation procedure.

Some words must be spent with regards to the parameter `z_stop` contained in this file. If ascending dikes reach the depth defined by the value of `z_stop` the simulation will stop. This necessity arises because propagation runs are usually stopped at a distance from the free surface, in order to avoid unintended dike behavior when breaching the $z = 0$ boundary.

In order to better achieve my aim of describing rift volcanism evolution, I have extended the code to account for the stresses generated by previously ascended dikes as follows. I have introduced two controls on dike interaction, represented by the variables `inter_on` and `z_threshold` that are read by the program from the `input_field` file. The first is a boolean switch whose values `.true.` and `.false.` turn dike interaction on and off, respectively, while the latter is a reference depth which has to be compared to the tip depth of the previous dike. At the end of the run of each dike, the code evaluates `inter_on` and `z_threshold`. If the first happens to be `.true.` and `z_threshold` is smaller than the depth to the tip of the lastly propagated dike `zf_top`, the previous external stress matrix is de-allocated and the `DIKE_INTERACTION` subroutine is called. The latter opens the background stress field file and the file containing the stress generated by the last iteration of the previous dike, sums them together and finally overwrites the background stress file, calling a subroutine for allocating the new stress matrix. On the other hand, dikes whose tips exceed the reference depth `z_threshold` are thought to "erupt" and fully relax their stresses. The erupted material would then load on the free surface, inducing further stresses in the half-space that would result in maintaining the focusing effect, although to a lesser extent. I implemented this procedure in the `TRI_LOADING` subroutine, which reads the $x-$coordinate of the lastly propagated dike (if the depth to its top is less than `z_threshold`) and there applies a superficial loading in the form of an equilateral triangle with a cross-sectional area equal to that of the dike itself. The stress field generated by the loading is then added to the background stress and submitted to the following dike.

I also made the code operational to account for different dike properties from one run to the other, namely the cross-sectional area (plane strain analogue to magma volume) and magma density, in order to evaluate how different parameters affect dike propagation.

4.3 Comparison with interaction-free trajectories

In order to show the effects of dike interaction and their implications for the evolution of rift volcanism, I first provide results for a basin of given width for three different values of basin depth, and compare them with the interaction-free results obtained for the same rift parameters. The simulations are shown in figure 4.2 for a $W = 40\,\text{km}$ wide rift extending from $x = -20$ to $x = 20\,\text{km}$. On the left hand side of the figure the interaction-free trajectories are shown, whereas on the right hand side each dike moves within a stress field resulting from the background stress plus the stress generated by the previous dikes. The external stress is the superposition of a horizontal tensile stress of 5 MPa and a $D = 100$, 300 and 600 m deep full-graben (figure 4.2, top, middle and bottom panels, respectively). The horizontal stresses σ_{xx} due to the superposition of unloading, dike and the 5 MPa tectonic stresses are shown as a shaded contour in the background of figure 4.2. Dikes are injected from left to right at $z = 40\,\text{km}$, $x = 2, 4$ and 6 km, except for the $D = 600\,\text{m}$ deep basin, where they are injected from bottom to top at $x = 2\,\text{km}$, $z = 40, 39$ and 38 km.

These snapshots represent three settings in which the stress barrier has not formed yet ($z_1, z_2 \notin \mathbb{R}$), is included in the domain ($0 < z_1 < z_2 < z_{moho}$) and extends beyond the domain ($0 < z_1 < z_{moho} < z_2$), respectively. Although being probably not representative of the evolution of a rift, for there is a very short period of time where the barrier is such that $0 < z_1 < z_2 < z_{moho}$, figure 4.2 simply captures some consequences of considering dike interaction in our discussion. Previously ascended dikes focus the emplacement of subsequent dikes in a narrower region, fostering the formation of large volcanic structures. The trajectories remain unchanged until a dike moves close to another and starts to feel its stress field. Interestingly, for the 600 m deep rift, the effect of the first two dikes is to promote the ascent of the third one, which would otherwise remain stuck if dike interaction was not considered.

The material parameters employed in this and the following simulations are summarized in table 4.1.

Symbol	Definition	Value
μ	rigidity of the rock	20 GPa
ρ_r	rock density	$2900\,\text{kg}\,\text{m}^{-3}$
ρ_m	magma density	$2600\,\text{kg}\,\text{m}^{-3}$
ρ_s	sediments density	$2700\,\text{kg}\,\text{m}^{-3}$
ν	Poisson's ratio of the rock	0.25
K	bulk modulus of magma	10 GPa

Table 4.1: Material properties employed in the simulations of chapter 4. Values are taken from Maccaferri et al. (2014) and Turcotte & Schubert (2002).

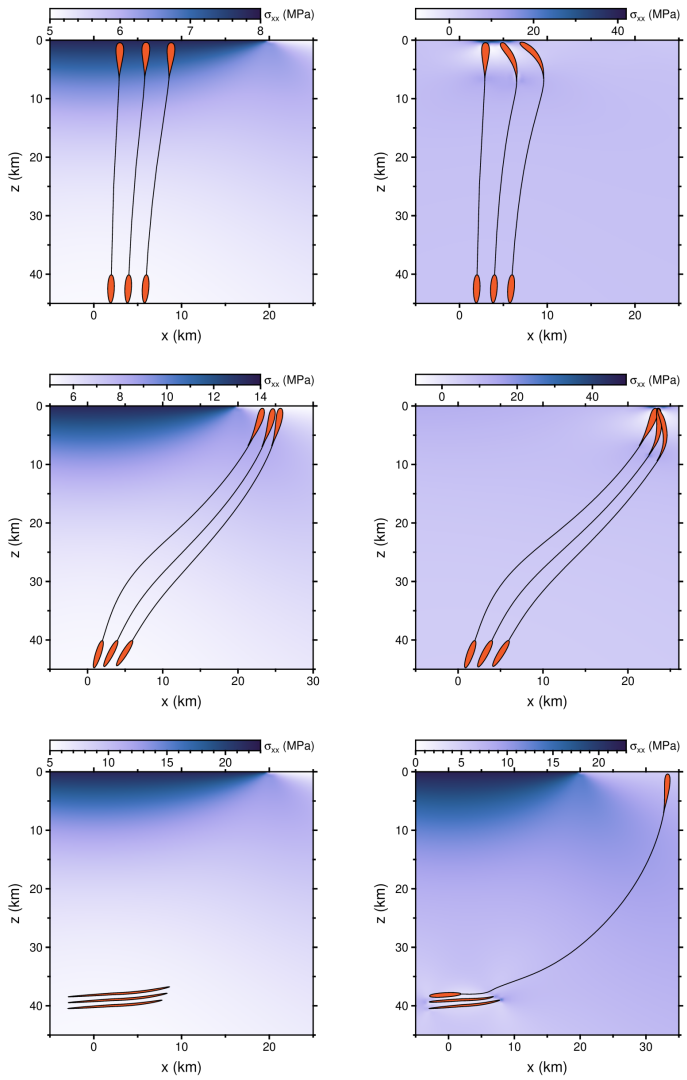

Figure 4.2: Dike simulations for a rift extending from $x = -20$ to $x = 20$ km. From top to bottom, $D = 100$, 300 and 600 m. *Left column*: interaction-free trajectories. *Right column*: interacting dikes. Shaded contour shows the superposition of horizontal unloading stresses and a 5 MPa tensile stress. See section 4.3 for a more detailed description of the figure.

4.4 Analysis of dike trajectories

4.4.1 The full-graben case

Despite providing clear insights into the effect of dike interaction, figure 4.2 does not shed much light on how this might be able to affect the long term distribution of volcanism as the rift basin evolves. A better description of this phenomenon should investigate how dikes might be able to interact with each other from one configuration of the stress barrier to the other. This is in fact shown in figure 4.3 for a $W = 40\,\text{km}$ wide full-graben at three stages of its depth evolution, namely $D = 100$, 300 and 600 m. These correspond to the stress barrier having not formed yet, being fully included in the domain and extending beyond the domain in the positive z direction, respectively. In analogy to figure 3.3, the colors of the dikes have been chosen so that the most recently ascended dikes are filled in red and former intrusions are filled with increasingly lighter colors (orange, yellow). Also, dikes have been chosen to be injected at $z = z_{moho}$ and at random horizontal coordinates extracted from a normal distribution with mean $\mu = 0$ and standard deviation $\sigma = b/2$. Note how dikes move roughly perpendicular to the direction of the least compressive eigenvalue σ_3 (grey segments in the background of figures 4.3 and 4.4), validating the assumption made in chapter 3. The trajectories become however more unstable when close to other dikes.

Considering dike interaction leads to a dramatic departure from non interacting trajectories when close to previously emplaced dikes, while dike paths remain basically unchanged up to a distance of approximately one dike length to previous intrusions. For shallow basins (figure 4.3, top panel) there is no stress barrier yet and dike trajectories are sub-vertical, causing closely injected dikes to interact at the surface. On the other hand, distantly injected dikes tend to ascend independently from each other. As the rift deepens, a stress barrier is formed (figure 4.3, middle panel). This results in important consequences on the determination of dike trajectories. Because the depth at which z_2 appears (figure 3.2) is generally greater than the depth of emplacement considered in this example, dikes ascending from depth perceive the presence of the stress barrier before being influenced by the stress field generated by dikes emplaced at previous configurations of rift depth D, and therefore are not attracted by them. However, the trajectories are more closely spaced in this case than in the "no stress barrier" case, as could already be noted in figure 3.3, causing interaction between dikes from the same background stress configuration to be more likely. When $z_2 > z_{moho}$ (figure 4.3, bottom panel) dikes are injected from inside the stress barrier. As in Maccaferri et al. (2014), this results in different behaviors depending on the coordinate of injection. Dikes injected close to the vertical axis of the stress barrier (that is, $x = 0$) are likely to cease their ascent and get stuck as sub-horizontal sills. On the other hand, when dikes are injected at some greater distance from $x = 0$, they might be able to "escape" the stress barrier, eventually reaching the surface.

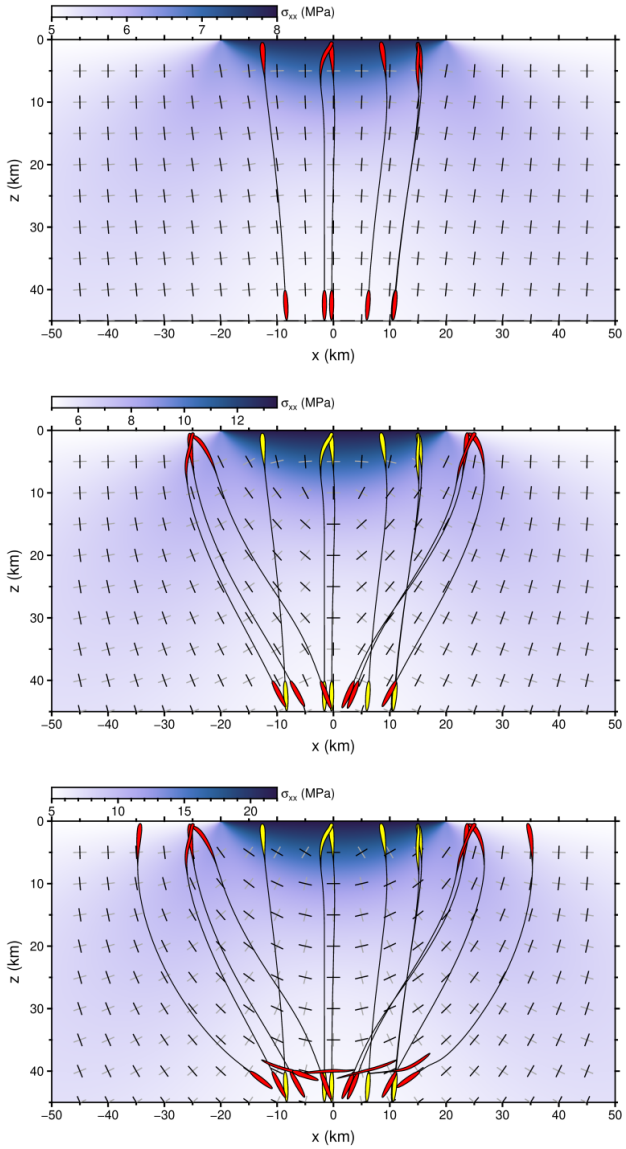

Figure 4.3: Dike simulations for a symmetrical rift extending from $x = -20$ to $x = 20\,\text{km}$. From top to bottom, the rift is $D = 100$, 300 and 600 m deep. Shaded contour shows the superposition of horizontal unloading stresses and a 5 MPa tensile stress. Black and grey segments in the background indicate the directions of the inplane maximum and minimum compression directions due to the background stress, respectively. See section 4.4.1 for a more detailed description of the figure.

4.4.2 The half-graben case

The effects of dike interaction for dikes propagating below a half-graben are shown in figure 4.4 for a $W = 40\,\text{km}$ wide rift at three different basin depths, namely $D = 200$, 500 and 900 m. Due to the geometry and intensity of the stress barrier below the half-graben, these values have been chosen to be different from those employed in section 4.4.1 in order to investigate similar settings in terms of the location of the stress barrier.

It is immediately evident how dike trajectories below half-grabens result in surface volcanism being focused on the shallower side of the basin, as it was already noticeable in figure 3.7. As for the full-graben, dike interaction forces dikes to be attracted by previous intrusions if they are injected closely enough but in this case interaction with dikes emplaced at earlier configurations of basin depth is more likely due to the stress barrier being shifted from the center. This may promote the formation of polygenetic volcanoes inside the rift depression, as opposed to full-grabens where this is limited to the flanking regions, at least in the early stages of rifting. On the other hand, the geometry of the barrier prevents dikes from ascending towards the inside of the deeper side of the basin, forcing their way up to the right flank.

4.5 Density of dike emplacements

The simulations carried out in the previous section still do not clearly show how the growth of the stress barrier affects the preferred depth of emplacement of propagating dikes thorough time. In this respect I conducted a series of simulations meaning to represent the progressive deepening of a basin with time and its effect on the propagation of dikes at and between each stage of evolution.

The results are shown as density plots in figures 4.5 and 4.6 for a $W = 40\,\text{km}$ full-graben and a a $W = 40\,\text{km}$ half-graben, respectively. For each case, 10 different simulations have been conducted, with basin depths ranging from $D = 100\,\text{m}$ to $D = 1\,\text{km}$. A number of dikes have been injected at each run and the stress field generated by their emplacement has been maintained through the following runs. For the first simulations, dikes were injected at normally distributed x_{inj} coordinates and fixed z_{inj} depth. On the other hand, z_{inj} has been varied for the last runs in order to avoid unrealistic behavior of dikes when injected too close to previously emplaced ones. This is not physically meaningless, as previous sill-like intrusions can in turn become the source of ascending magma. The number of dikes for each run has been arbitrarily increased with increasing rift depth to represent intensified melting due to the shallowing of the Moho and the decompression resulting from the basin unloading. The number of simulated dikes, the coordinates of their injection and the depth of the rift are provided for each run in table D.1 and D.2 for the full and half-graben cases, respectively.

I start by analyzing the full-graben case shown in figure 4.5. As expected

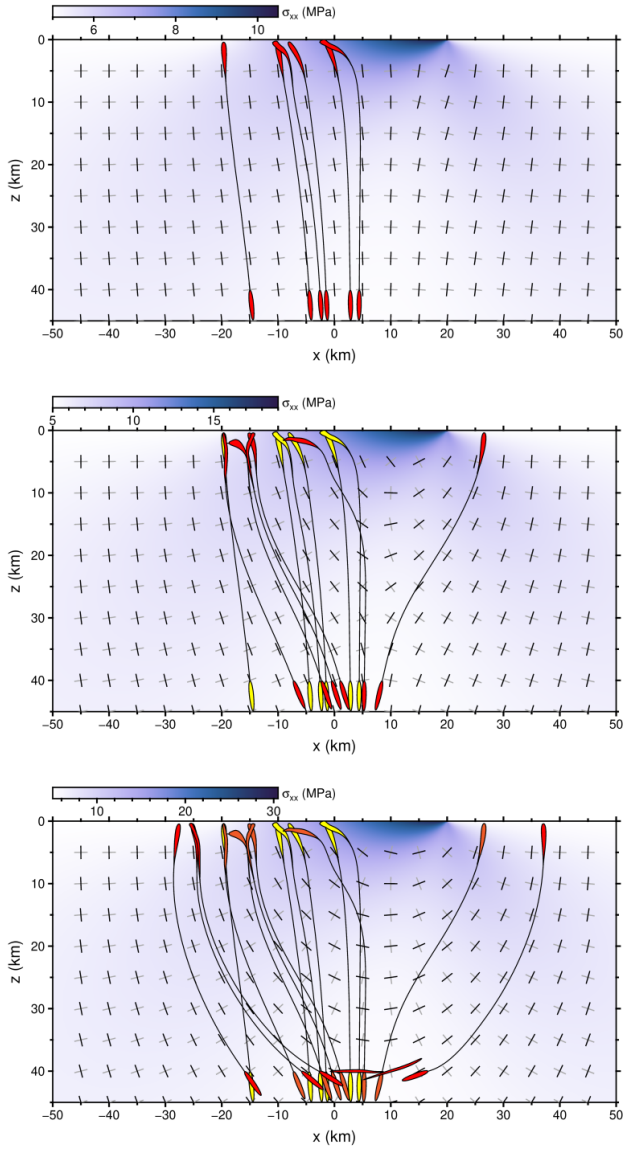

Figure 4.4: Dike simulations for an asymmetrical rift extending from $x = -20$ to $x = 20\,\text{km}$. From top to bottom, the rift is $D = 200$, 500 and 900 m deep. Shaded contour shows the superposition of horizontal unloading stresses and a 5 MPa tensile stress. Black and grey segments in the background indicate the directions of the inplane maximum and minimum compression directions due to the background stress, respectively. See section 4.4.2 for a more detailed description of the figure.

from the considerations made in the previous sections, at first dikes tend to ascend to the surface of the rift basin, possibly breaching it and erupting. If dikes are injected closely enough they are attracted by neighbouring intrusions and may create zones of magma accumulation. As the stress barrier grows, dikes are deflected towards the flanks of the rift, increasing the possibility of interaction due to the trajectories being more closely spaced. After z_2 overcomes z_{moho}, some dikes might be able to escape the barrier and make their way up to the surface, but the majority of them gets trapped as horizontal sills close to their injection site. This effect becomes increasingly frequent as the rift deepens and the barrier becomes more intense.

The half-graben case is shown in figure 4.6. As for the full-graben, surface volcanism is predicted to shift from the inside of the basin to its flanks, but the transition does not happen as abruptly. Instead, some dikes still manage to erupt inside the rift depression. Due to the position of the stress barrier and its lower intensity for a given basin depth D, sill-like structures fail to appear until a greater deepening is reached. This causes dikes to become more focused in the proximity of the surface than they were in the symmetrical case. This is also shown in the polar histograms provided in appendix C.

Some words must be spent with regards to the simulations leading to figures 4.5 and 4.6. For these simulations, dikes emplaced at all depths have been thought to maintain their stress field and therefore contribute to the external stress field perceived by the subsequent dikes. In reality, when dikes get very close to the surface they may, partially or totally, erupt, therefore releasing part of their stress. This could result in an overestimate of dike interaction by the simulations at issue. However, this is not necessarily true. First, evidence is provided for dikes to get arrested during their propagation near the surface. Xu et al. (2016) used insights from InSAR, stress calculations and analog experiments to explain the arrest of the 2009 Harrat Lunayyir dike intrusion in Saudi Arabia. They showed how the dike propagating at shallow depth induced graben-bounding normal faulting due to the extension generated above its tip. Slip on the graben faults resulted in turn in hindering further vertical propagation of the dike, causing its arrest at shallow depth. Second, as magma is erupted by ascended dikes it would load on the free surface, resulting in the redistribution of stresses in the vicinity of the eruption site. Loads on free surfaces have the result of attracting ascending cracks, possibly maintaining the focusing effect. This is in fact taken into account for the simulations of the next section.

4.6 Long-term evolution

In section 4.5 I found that the intensification of the stress barrier due to the deepening of the rift is responsible for the formation of sill-like lower crustal structures that tend to grow in thickness as the basin evolves. The progressive accumulation of underplated material will form a new magma storage zone which, together with the shallowing of the Moho due to mantle upwelling, will

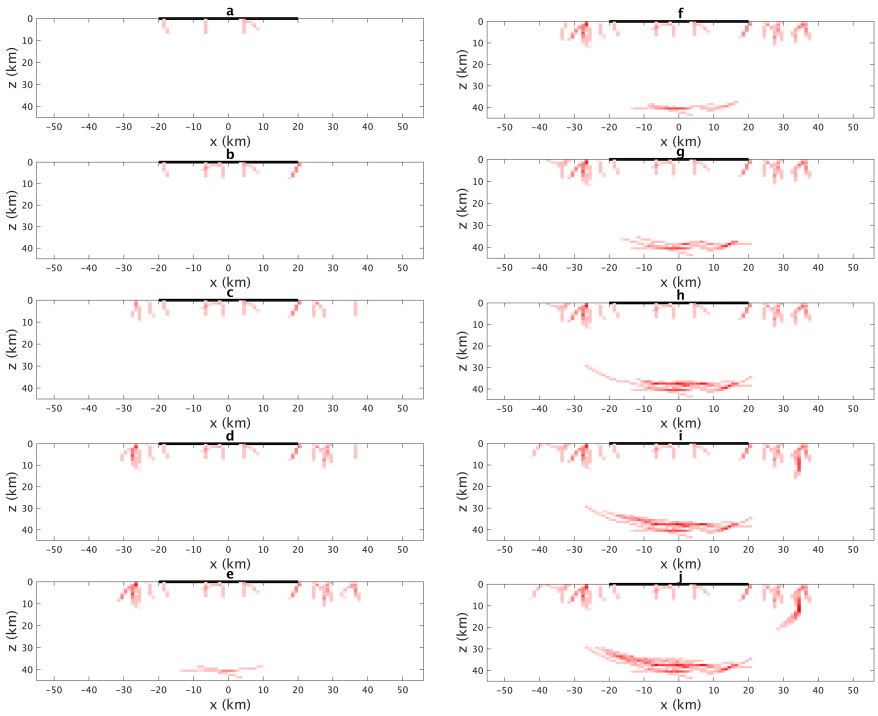

Figure 4.5: Density of dike segments at different stages of rift deepening for a $W = 40\,\text{km}$ full-graben, from $D = 100\,\text{m}$ (panel `a`) to $D = 1\,\text{km}$ (panel `j`). Red areas indicate zones of high dike segment density. Black bold line at $z = 0$ indicates the location of the rift basin. See section 4.5 and table D.1 for further description and simulation parameters.

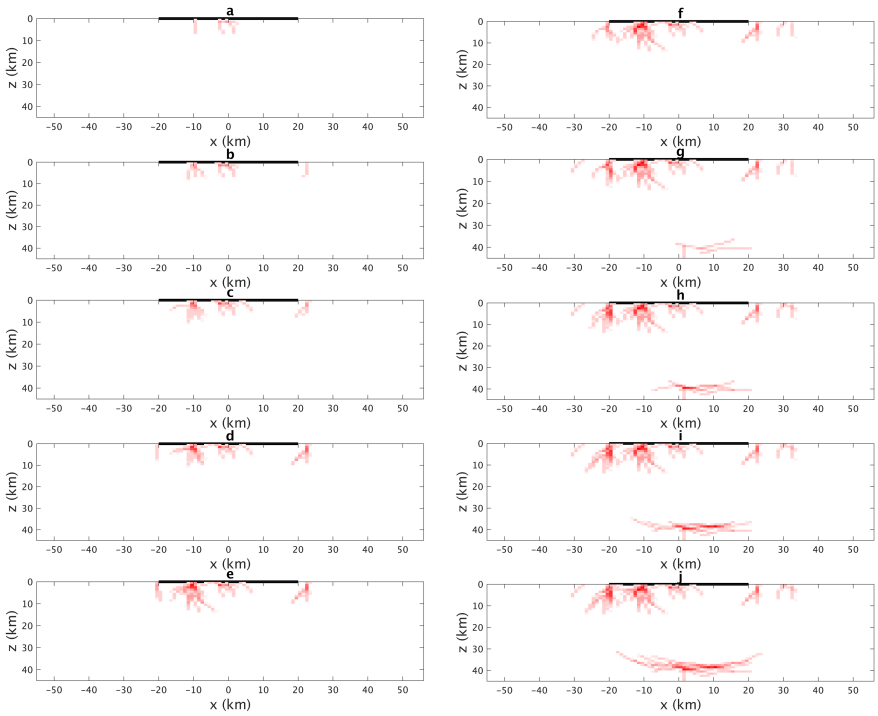

Figure 4.6: Density of dike segments at different stages of rift deepening for a $W = 40\,\text{km}$ half-graben rift, from $D = 100\,\text{m}$ (panel `a`) to $D = 1\,\text{km}$ (panel `j`). Red areas indicate zones of high dike segment density. Black bold line at $z = 0$ indicates the location of the rift basin. See section 4.5 and table D.2 for further description and simulation parameters.

progressively raise the depth at which magma is injected into the crust. This may be combined with the widening of the rift due to stretching and the accumulation of low-density sediments inside the basin. Both sediment loading and rift widening have the effect of deepening the upper limit of the stress barrier z_1. This may lead to a shift of surface volcanism from the flanks back into the rift depression. This is shown in figure 4.6, where the above mentioned effects are combined to provide a scenario for a boundary element simulation: the depth of the Moho discontinuity has been raised from $z_{Moho} = 40$ to $z_{Moho} = 30\,\text{km}$ (represented by the blue shaded area in the figure); a 12.5 km thick layer of underplated material has been envisioned above the Moho, coherently with the location and dimension of the sill-like structures observed under rifts (Thybo & Artemieva 2013) and investigated in section 4.5; a $W = 100\,\text{km}$ wide basin has been simulated through the application of a $D = 1\,\text{km}$ deep unloading and the superposition of a $T = 600\,\text{m}$ thick layer of low-density sediments, whose topography is shown in the upper panel of figure 4.7. Dikes injected from above the stress barrier will reach the surface inside the depression. This would mark an additional stage in the distribution of volcanism in rift zones, coherently with the observation of the migration of surface volcanism from the flanks to the axial part of the rift in many extensional settings (Kiselev 1987, Corti 2009).

In order to fully examine the long-term evolution of volcanism in a deepening rift I carried out 20 additional simulations for a $W = 100\,\text{km}$ wide rift, as shown in figures 4.8 and 4.9 . The first 10 simulations represent the deepening of the basin from $D = 100\,\text{m}$ to $D = 1\,\text{km}$. The remaining 10 simulations (figure 4.9) account for sedimentation processes through the application of a strip loading with thickness increasing from $T = 100\,\text{m}$ to $T = 800\,\text{m}$ (figure 4.9, panels `k` to `r`), as documented in tables D.3 and D.4.

Four stages of rift-related volcanism can be distinguished by looking at figures 4.8 and 4.9. The first one (corresponding to panels `a` to `c`) is a phase of scattered in-rift dike arrivals. During the second stage (panels `d` to `g`) ascending dikes start to be deflected by the stress barrier, resulting in the formation of off-rift volcanoes. Moreover, dikes begin to get stuck as horizontal sills if they are injected too close to the rift axis, where the stress barrier grows in intensity. This becomes more frequent in the third phase (panels `h` to `p`), where the layer of underplated material grows in thickness and external dikes may eventually escape the barrier reaching the surface by the flanks. Lastly, the sedimentary loading and the shallowing of the injection depth due to the stacking of the sills result in a fourth stage (panels `q` to `t`), where volcanism begins to focus back to the inside of the rift basin. To better display the four stages, the simulations belonging to each of them have been plotted in different colors (green, magenta, blue and red, from early to later stages) in figure 4.10, along with the respective rift topography and vent locations.

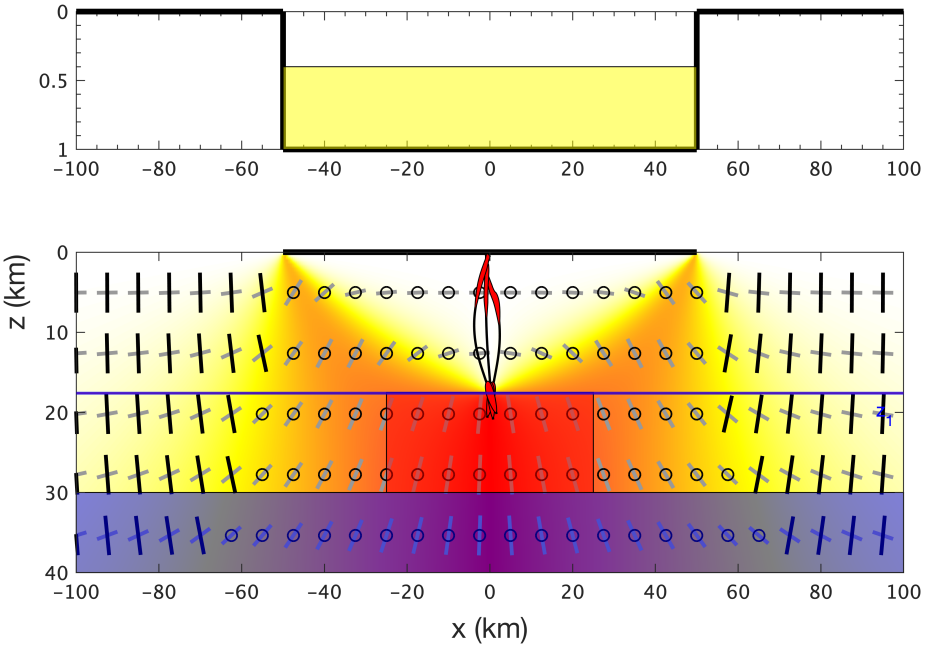

Figure 4.7: *Top*: topography of the rift basin, with sediments in yellow. *Bottom*: last stage of the evolution of rift-related volcanism, following the considerations made in section 4.7.2. The blue and red patches represent Moho uplift and sill-like structures, respectively. The horizontal blue line is the upper limit of the stress barrier z_1. Three dikes have been injected from above z_1. Their trajectories and their initial and final locations are superimposed on the background.

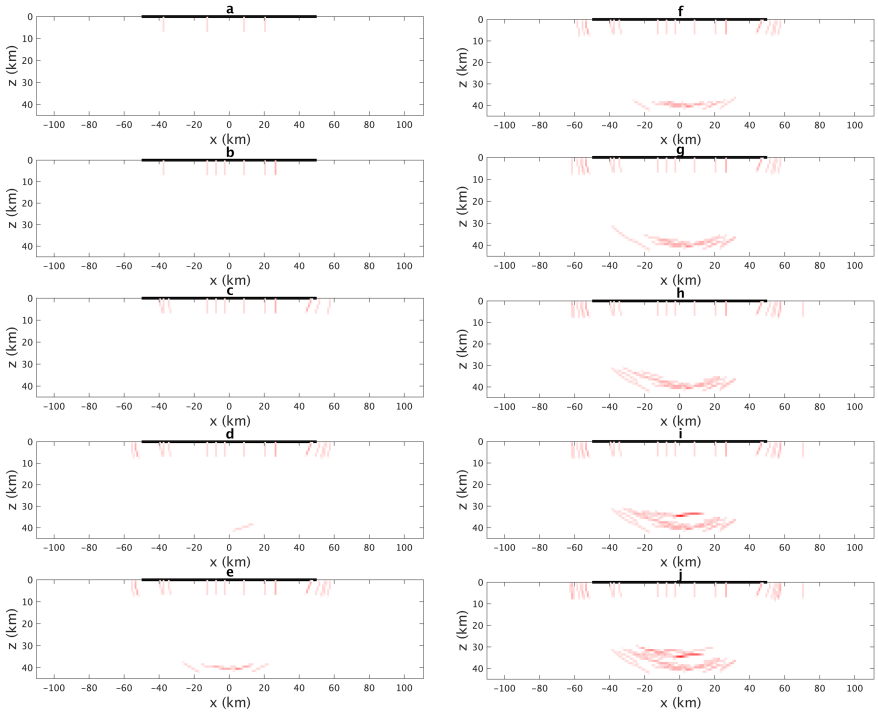

Figure 4.8: Density of dike segments at different stages of rift deepening for a $W = 100\,\text{km}$ full-graben, from $D = 100\,\text{m}$ (panel `a`) to $D = 1\,\text{km}$ (panel `l`). Red areas indicate zones of high dike density. Black bold line at $z = 0$ indicates the location of the rift basin. Panels continue in figure 4.9. See section 4.6 and table D.3 for further description and simulation parameters.

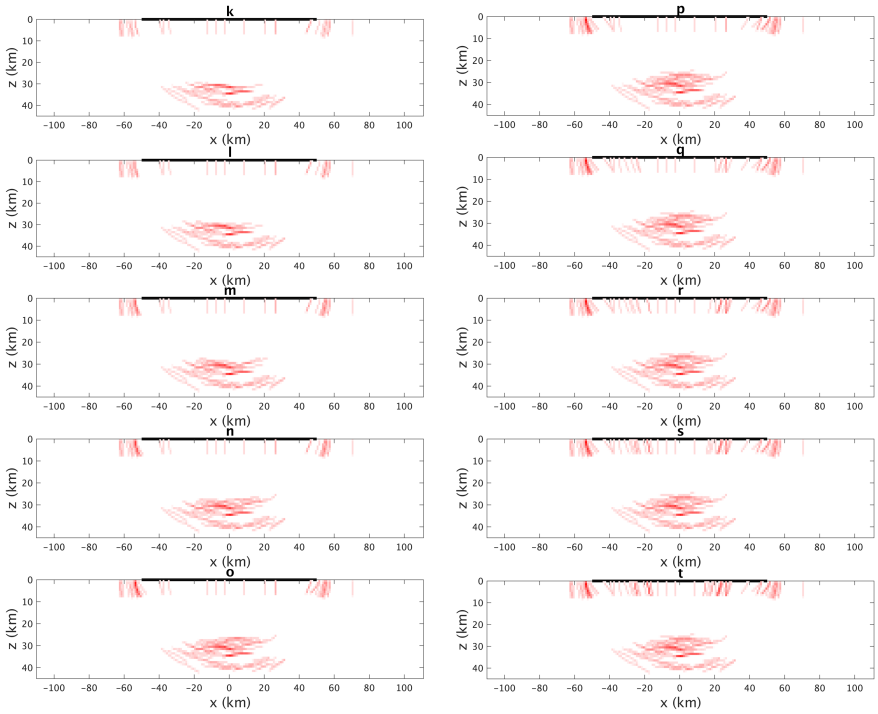

Figure 4.9: Density of dike segments at different stages of rift deepening for a $W = 100\,\text{km}$ wide symmetric rift, from $D = 1.1\,\text{km}$ (panel `k`) to $D = 2\,\text{km}$ (panel `t`). Red areas indicate zones of high dike density. Black bold line at $z = 0$ indicates the location of the rift basin. See section 4.6 and D.4 for further description and simulation parameters.

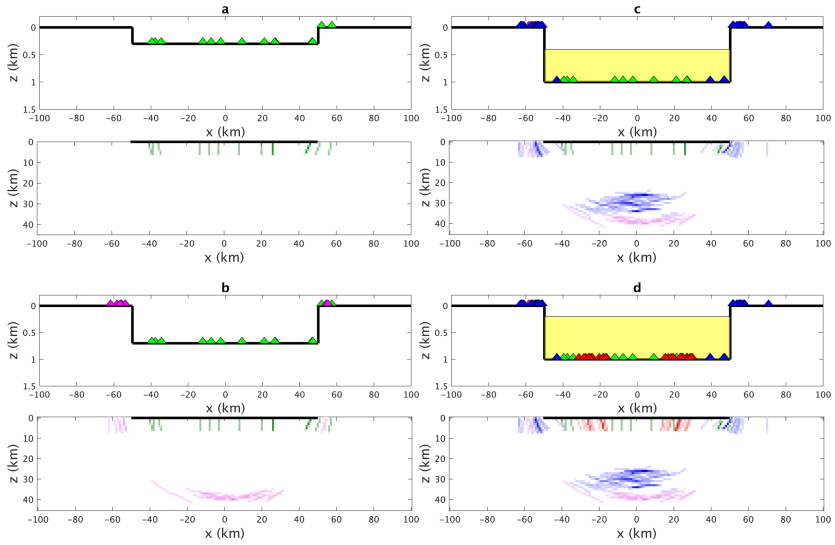

Figure 4.10: The four stages of rift-related volcanism as described in section 4.6. For each stage, the upper panel displays the topography of the rift and the locations of vents, while the lower panel shows the density distribution of dikes up to that simulation. The yellow patch indicates the thickness of sediments. See section 4.6 for further description.

4.7 Conclusions

4.7.1 Overview

In chapter 4 I refined the models carried out in chapter 3 to account for the possibility of dike-dike interaction. I have done this by extending the boundary element dike propagation code developed by Maccaferri et al. (2011) to let dikes interact with each other through the stress field generated at their emplacement. As expected from other works on the subject (Kühn & Dahm 2008, Ito & Martel 2002), this results in dike crossing and focusing for closely injected dikes. As for sufficiently deep rift basins, this would further promote off-rift merging of dikes, consistently with the presence of large volcanic structures on the flanks of some rift basins, like Mount Chamo in Ethiopia (Corti 2009) and the Monts Dore and Sancy stratovolcanoes near the Limagne graben (Michon & Merle 2001). At first the number of dikes for each simulation was kept low in order to keep the figures clear. Larger numbers of dikes and simulations were then run to create density plots for the purpose of revealing the areas of preferred dike focusing and their evolution through time. The progressive deepening of the basin causes magma intrusions to shift from the inside of the rift to its flanks, eventually accumulating as horizontal sills close to their injection depth (figure 4.13). This is consistent with the presence of underplated layers or lower crustal magmatic intrusions observed in a variety of extensional continental areas and

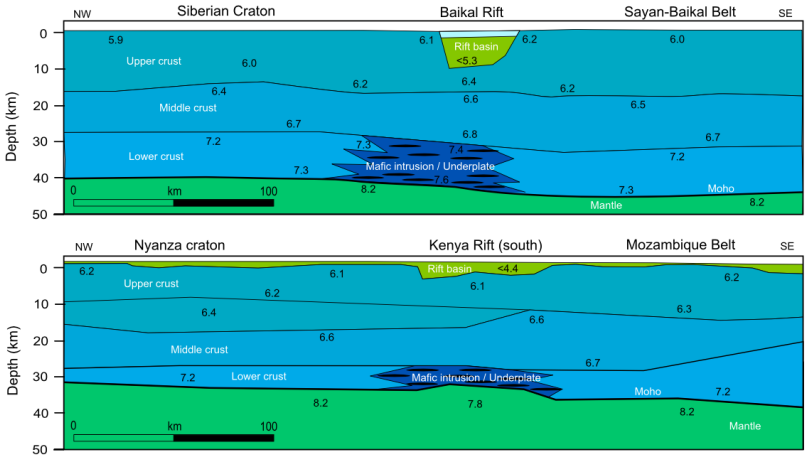

Figure 4.11: Seismic P-wave velocity structure of the crust along two profiles across presently active rift zones: The Baikal Rift zone in Siberia (top, after Thybo & Nielsen (2009)), southern Kenya Rift (bottom, after Birt et al. (1997). Modified from Thybo & Artemieva (2013).

rift zones (Thybo & Artemieva 2013) (figure 4.11): Birt et al. (1997) observed a strongly reflective lower crust directly below the Kenya Rift graben, coherent with the presence of an high velocity underplated layer; Mackenzie et al. (2005) explained variations in seismic reflectivity in the lower crust beneath the Main Ethiopian Rift in terms of layered sills; Thybo & Nielsen (2009) attributed the high seismic velocity zone below the Baikal rift depression to horizontal magmatic intrusions in the lower crust.

Lastly, I found that the joint action of underplating induced by the stress barrier, rift widening caused by lithospheric stretching and sedimentary loading promotes a further shift of rift-related volcanism from the flanks of the basin back to the inside, favored by Moho uplift due to mantle upwelling.

4.7.2 Discussion

The results obtained in chapter 4 shed new light on the possible mechanisms responsible for the transition from off to in-rift volcanism observed in many extensional settings, as the Baikal Rift and the Main Ethiopian Rift. Corti (2009) divides the tectonic history of the MER in two different phases: an early Mio-Pliocene ($2 - 24$ My) rifting stage - characterized by displacement along large boundary faults and intense volcanic activity distributed within the rift, on the flanks and near the faults - and a second Quaternary (< 2 My) rifting stage, marked by the deactivation of the boundary faults and a riftward shift of the volcano-tectonic activity (figure 1.5). This is consistent with my conclusions, also considering evidence for the presence of underplated material under the

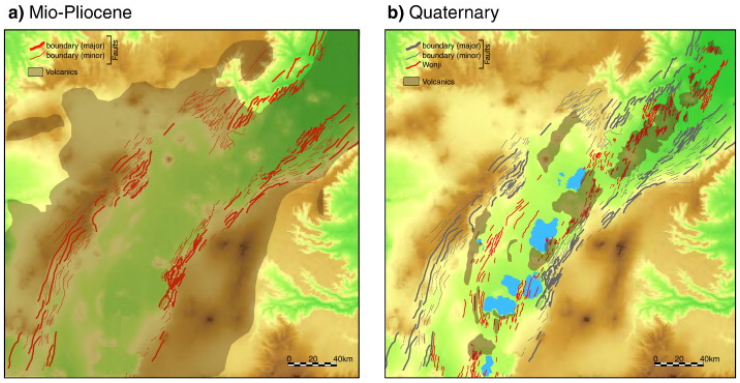

Figure 4.12: Distribution of volcanic rocks (brown shaded areas) in the MER in the Mio-Pliocene and Quaternary. *Left:* bold red segments - major boundary faults; red segments - minor boundary faults. *Right:* bold grey segments - major boundary faults; grey segments - minor boundary faults. Image taken from Corti (2009).

MER (Mackenzie et al. 2005) and the concurrence of the above mentioned shift with the deactivation of the boundary faults, that has resulted in hindering further deepening of the basin and shallowing of the stress barrier, favoring in-rift volcanism.

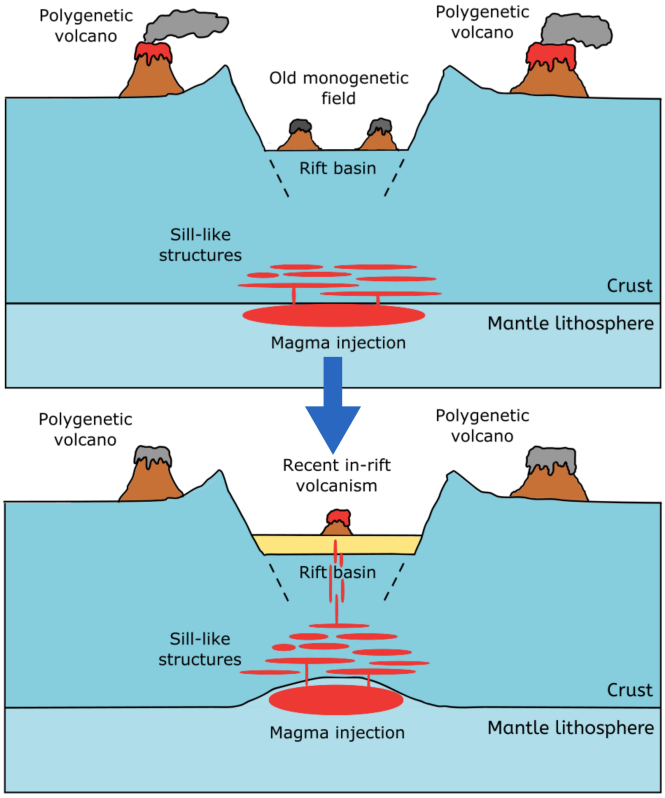

Figure 4.13: The two last stages of the evolution of rift-related volcanism, following the results outlined in chapter 4. *Top*: the intensification of the stress barrier causes dikes to get stalled at lower crustal depths, resulting in the formation of sill-like structures. *Bottom*: the joint action of rift widening, sediment loading and sill formation moves volcanism back to the inside of the rift.

Chapter 5

Summary and Perspective

5.1 Overview

In chapter 3 I have investigated how the unloading stresses generated by the progressive deepening of a rift basin in extensional settings is able to influence the location of vents and intrusions through time by rotating the principal stresses in an elastic crust, resulting in modified dike trajectories. I found that volcanism in symmetrical rift zones, if melt is available during the early stages, is expected to start in the inside of the basin, likely resulting in scattered monogenetic structures. After a critical depth of the basin is reached, volcanism would shift to the flanks of the rift due to the formation of a stress barrier under the rift. At this stage, the formation of off-rift polygenetic structures is promoted by the tight spacing of dike trajectories. The case of a triangular shaped half-graben appears to be more complex due to the asymmetry of the stress barrier, causing a prolonged phase of in-rift volcanism. The spatial distribution of surface volcanism is highly dependent on the horiziontal coordinate at which dikes nucleate: dikes injected from below the deeper side of the basin tend to ascend towards the flank, while those that form below the shallower side may still erupt within the rift.

In chapter 4 I have extended my model to account for the role of the stresses generated by formerly emplaced and erupted dikes in setting the trajectories of the subsequent ones, leading to enhanced dike focusing and enforcing the results of chapter 3. I found that for high values of basin depth dikes may get stuck as sill-like structures beneath the rift, creating a thick layer of underplated material that may serve as a shallower injection depth for subsequent dikes. The presence of this layer, if combined with the widening of the rift due to stretching and the sedimentary loading, could result in a later stage where dikes are injected from above the stress barrier, moving surface volcanism back to the inside of the rift. I argued that this effect could also be enhanced by the shallowing of the Moho due to mantle upwelling, which cannot however be simulated by this model.

It should be pointed out that the four stages depicted in this work are a result

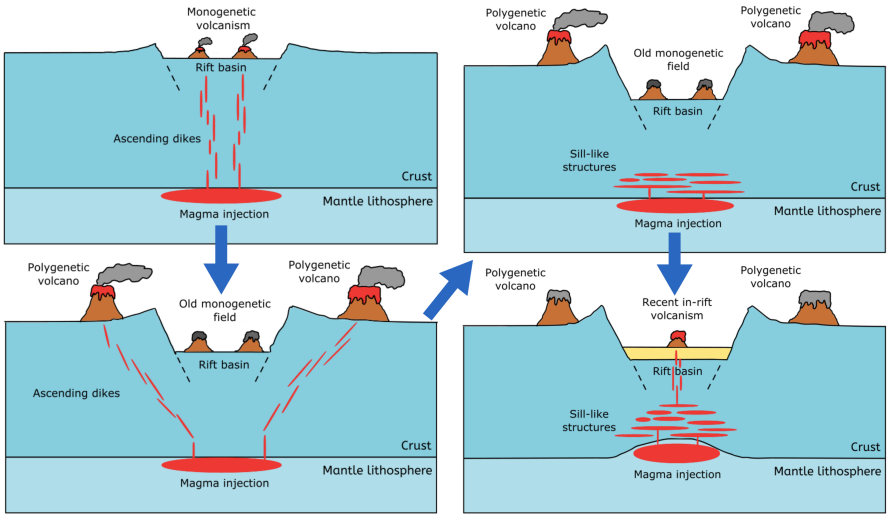

Figure 5.1: The four stages of rift-related volcanism as envisioned in our work.

of the specific assumptions and choices of model parameters made throughout the dissertation. In reality, the order and timing of the events could differ from those shown here, mainly due to variations in rift parameters and magma supply. For instance, considering narrower rifts may result in a prolonged phase of off-rift volcanism and a delayed phase of sill forming, due to the reduced thickness of the stress barrier during the first periods of basin deepening. Also, the late in-rift shift of volcanism described in this chapter may be postponed or completely hindered for narrower rifts, z_1 being significantly shallower for them than it is for wider ones. Therefore, care must be taken when applying the results of this work to specific rift areas, in that the model should be first adjusted to the specific case studies before drawing any conclusions. Moreover, the simulations leading to figures 4.8, 4.9 and 4.10 were conducted with the BEM code developed by Maccaferri (2010), Maccaferri et al. (2011) and do not include the contribution of mantle upwelling to the results. In order to consider a more realistic evolution of the lithosphere below the rift, a geodynamical code would be needed. The shallowing of the Moho would have the effect of further raising the depth at which dikes are injected, not only supporting the results of our model but possibly amplifying them, especially during the last stages.

The results achieved with this work, if properly adjusted to account for different parameters, may shed light on the physical mechanisms at the base of the evolution of volcanism in a number of different rifting settings.

5.2 Limits of the model and outlook

5.2.1 Rheology of the lithosphere

Chapters 3 and 4 were constructed upon the assumption of a purely elastic crust subjected to everlasting stresses of unloading and tectonic origin. As mentioned in section 3.1 this was justified by a number of considerations regarding the strength and the estimated viscosity of the crust. However, the high variability surrounding both these parameters and the timespans of rifting requires the role of lithospheric rheology to be taken into account.

American chemist E. C. Bingham coined the term *rheology* in 1929 and described it as "the study of the flow and deformation of all forms of matter". This study involves the use of constitutive equations to relate strains and stresses acting on a given material. It is clear that a good knowledge of the rheology of the Earth's interior is of prominent importance in providing the means of assessing its history and evolution. In this perspective, understanding the rheology of the lithosphere in particular is fundamental for a more dynamical description of rifting. However, the problem of assessing the rheological behaviour of the various lithospheric layers is far from trivial.

Bürgmann & Dresen (2008) effectively describe the three main models of the distribution of rheological properties and strength in the crust and upper mantle, as shown in figure 5.2. In a food consistency analogy, these are termed the jelly sandwich model, the crème brulée model and the banana split model.

The *jelly sandwich* model is the classic view of a weak middle-to-lower crust included between a strong upper crust and a strong mantle lithosphere. The upper crust exhibits a pressure-dependent increase of the frictional strength of rocks and is coherent with the Mohr-Coulomb theory and the empirical Byerlee's law, until a brittle-ductile transition is encountered for temperatures between 300 and 500° C. The *crème brulée* model has been proposed as an alternative to the jelly sandwich model and posits that the mantle lithosphere is weakened by thermal and porous processes. In this case the strength of the continental lithosphere would be mostly determined by the dry and brittle crust. Finally, the *banana split* model argues that the continental lithosphere has been greatly reduced in strength along plate boundaries due to the high temperatures and strain rates and the role of water.

The issue of whether the overall deformation of the lithosphere is accomodated by discrete weakened zones or by a viscous lower lithosphere is one with considerable history. This originated from the attempt of interpreting the transient deformation observed in the post-1906 San Francisco earthquake triangulation data (Segall 2010). In this regard, Thatcher (1983) highlighted the impossibility of distinguishing between a *thick lithosphere* model with transient slip on the downdip extent of the fault and a *thin lithosphere* model relying on distributed viscoelastic flow, as already pointed out by Barker (1976). Work has been done to reconcile evidence coming from geodetic, laboratory and geological observations (Bürgmann & Dresen 2008) and this has only served to emphasize the great variability of lithospheric strength and rheology as a function of age,

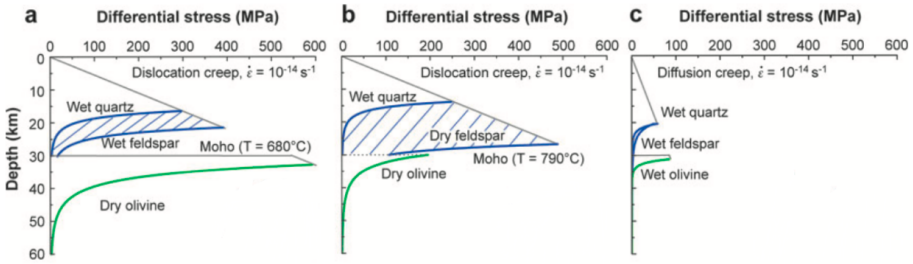

Figure 5.2: Strength of the lithosphere plotted as differential stress as a function of depth the three main models of lithospheric rheology: the jelly sandwich model (a), the crème brulée model (b) and the banana split model (c). Strength envelopes are based on the flow law parameters presented in Bürgmann & Dresen (2008). For the crust, a quartz and feldspar rheology was used, while the strong mantle is composed dominantly of dry olivine. A uniform strain rate of $\dot{\epsilon} = 10^{-14}\,\mathrm{s}^{-1}$ is used for all the models. Modified from Bürgmann & Dresen (2008).

composition, temperature and strain rate of the continental lithosphere. In this perspective, the three popular models described above should only be seen as end-members of generally more complex situations.

Considering other rheologies from the elastic one employed in this work can lead to different consequences on how the lithosphere transforms in response to tectonic forces and how the unloading stresses are maintained through time. The problem of the rheology of the lithosphere can be tackled in contexts of processes such as the formation of rifts by making use of geodynamical codes, as the one outlined in Sternai (2020) and based on Gerya (2019), or ASPECT, an extensible code written in C++ simulating convection in the Earth's mantle (Bangerth et al. 2021), and will be the subject of my future work.

5.2.2 Melting

Little or no attention was payed in my dissertation about the processes leading to the generation of magma needed for dikes to nucleate and ascend. A more complete discourse on the subject should definitely take into account the role of melting in defining the volumes of melt available to form dikes and the timing of events. This is often taken into account by geodynamical codes, as briefly outlined in Sternai (2020).

Active rifts are the result of the impingement of a mantle plume at the base of the lithosphere, and are thus characterized by early convection resulting in large scale volcanism followed by rifting. However, many continental rifts start as passive rifts and are usually devoid of magma until stretching thins the lithosphere sufficiently for the asthenosphere to melt through decompression (Burchardt 2018). The process is schematically shown in figure 5.3: as the crust is extended, the underlying mantle rocks rise from point A to point B, undergoing a considerable drop in pressure and a slight decrease in temperature.

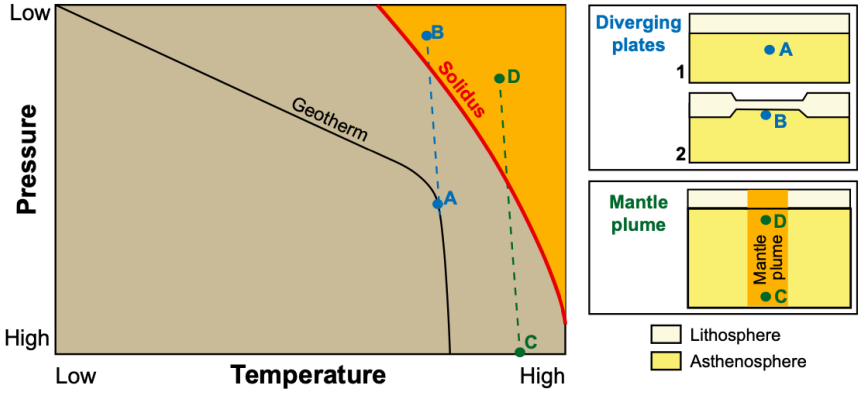

Figure 5.3: Decompression melting for mantle rocks lying at point A and C on the P-T diagram, representing the effect of diverging plates and a mantle plume, respectively. See section 5.2.2 for additional details. From Acocella (2021).

If point B happens to be above the solidus, partial melting occurs. A similar process occurs with mantle plumes, the decompression happening at greater depths due to the mantle within the plume being significantly hotter than the one through which it rises (Acocella 2021). It should be reminded however that this is not the only process responsible for rock decompression to happen in extensional settings. Rifting is usually characterized by the formation of large fault-bounded basins on the surface of the Earth, as described extensively in chapter 1. This would result in further decompression due to the unloading pressure acting beneath basin, which would add to the effect of mantle upwelling promoting partial melting.

5.2.3 3-D implementation

The superficial manifestation of rifting consists in the development of large scale fault-bounded basins extending for tenths of kilometers in width and hundredths of kilometers in length; similarly, dikes are characterized by three dimensions, one of which is usually orders of magnitude smaller than the others. As was already mentioned in sections 1.4 and 2.2.1, we took advantage of the geometry of the problem to simplify our model by making use of a plane strain approximation. This was apparently sufficient to obtain results that are consistent with diverse evidence from many extensional settings. However, the real structure of rifts can be very complex and assessing the role of three-dimensionality in rift-related dike propagation can be of great importance. Most analytical and numerical methods dealing with fluid-filled fracture propagation are two-dimensional. Davis (2021) extended them to three dimensions approximating the fracture as a penny-shaped crack influenced by both an internal pressure and stress gradients (analytical method) and simulating curved fractures as a

mesh of triangular dislocations computed using the displacement discontinuity method (numerical method). They applied the results to propagating dikes and sills in volcanic regions, focusing on reconstructing the trajectory of a large horizontal sill formed during the 2018 Sierra Negra eruption (Davis et al. 2021). In addition to involving short computation times, these models can be applied to arbitrary stresses, topographies and crack shapes, therefore proving to be very suitable to extend my simulations to three-dimensional unloading conditions and may serve as an interesting starting point for future works.

Appendix A

Loads on elastic half-spaces

The problem of the stress field generated in an elastic half-space due to loads applied on its free surface is one with considerable history. Solutions to the problem can be derived in a number of ways. Jaeger et al. (2009) make use of the complex variable method to investigate the stresses and displacements in an elastic half-space under the action of surface loads. Here I briefly summarize the fundamental steps in the development of the loading formulas used in chapter 3 as described by Davis & Selvadurai (1996).

In 1878 Joseph Boussinesq derived the solution for a normal *point load* applied to the surface of a homogeneous, isotropic, elastic half-space. The point load is mathematical artifice in that it implies the application of a finite force on a surface of zero area (that is, a point). This results in singularities in the stress and displacement fields at the point of application, that will eventually disappear when more physical conditions are considered. Starting from Boussinesq's solution, Albert Flamant solved the problem of a normal *line load* applied at the surface of an elastic half-space. His simple solution involved making use of the principle of superposition to integrate the point load solution along an infinite line. In a similar way, one can think of a *strip load* as a superposition of line loads arranged side by side, and integrate the line load solution along a finite length in a perpendicular direction to obtain equations 2.4.

A number of works have made use of these solutions to simulate the presence of a topographic load on the Earth's surface, such as a volcanic edifice, with applications to dike propagation (Dahm (2000), Maccaferri et al. (2011) among others). Maccaferri et al. (2014) employed the same analytical solutions but with opposite sign to represent the unloading due to the formation of a symmetrical basin in rifted areas. Figures A.1 and A.2 show the contours of the stress field components in an elastic half-space for a uniform strip unloading and a linearly increasing strip unloading, respectively, as calculated from equations 2.4 and 3.3. Notice the symmetry of figure A.1 with respect to the $x = 0$ axis and the asymmetry of figure A.2 that results in a curved and shifted stress barrier. Note that the horizontal stresses σ_{xx} shown in the upper panel of figures A.1 and A.2 are the result of the superposition of the unloading stresses and a uniform tensile

stress $\sigma_{tec} = 5\,\mathrm{MPa}$.

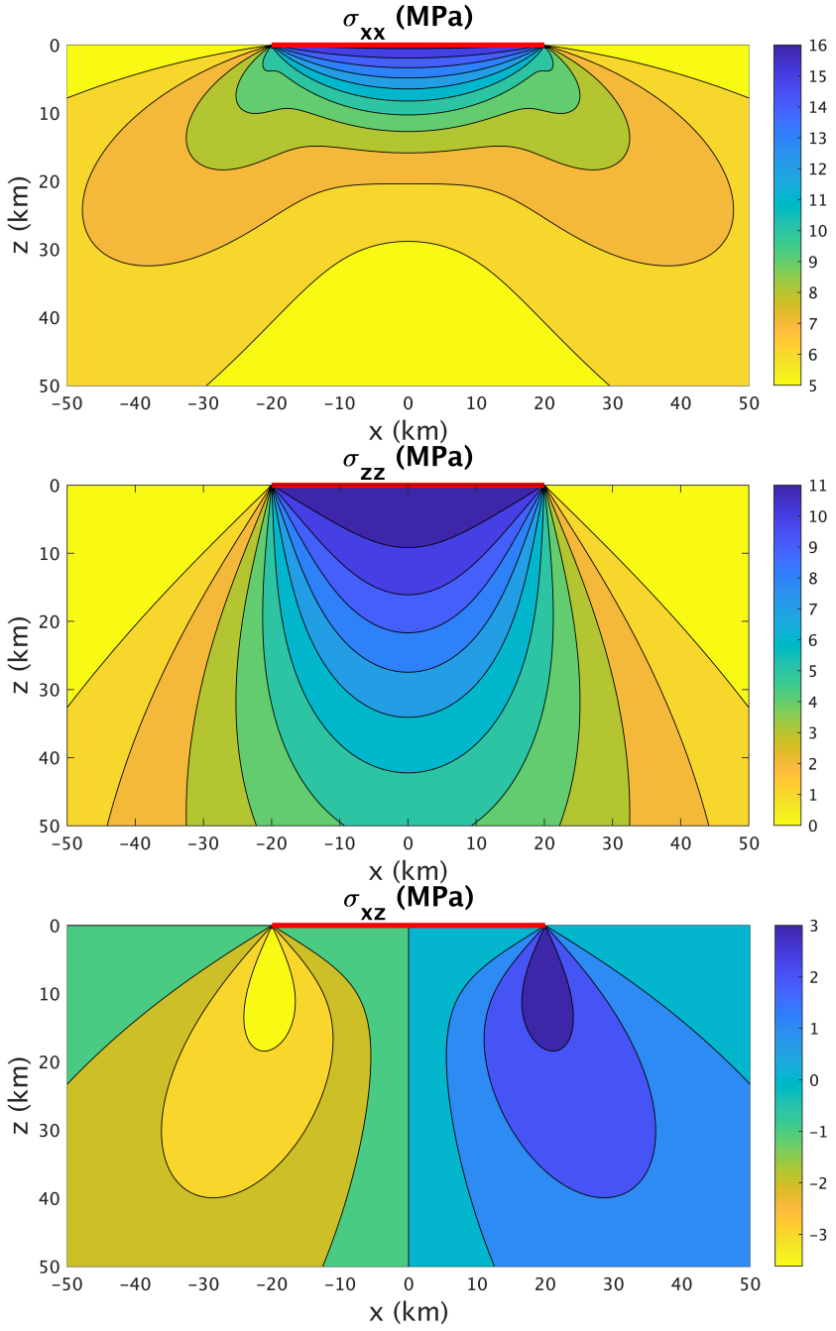

Figure A.1: Stress field generated in the crust by the application of a 40 km wide, 400 m deep symmetrical strip unloading (red horizontal line).

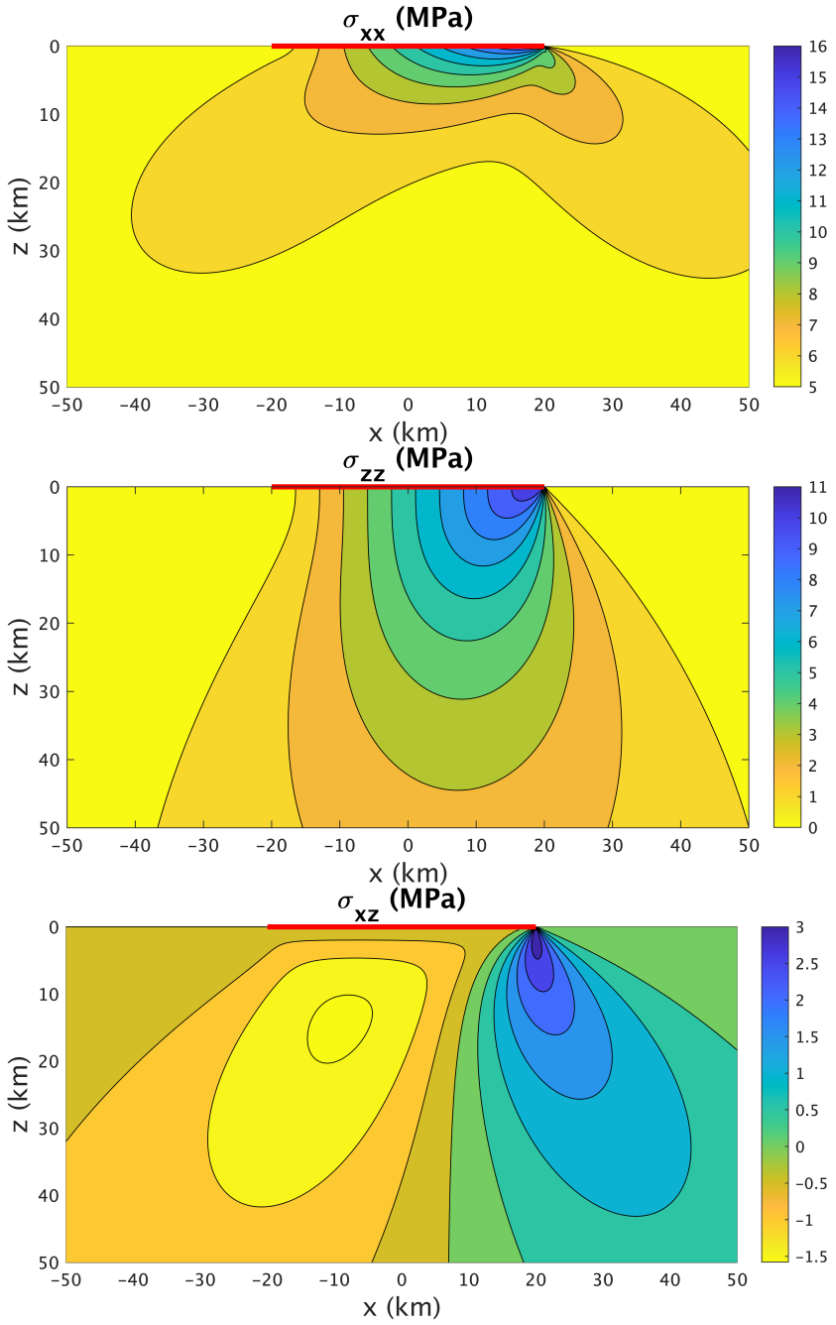

Figure A.2: Stress field generated in the crust by the application of a 40 km wide, 400 m deep asymmetrical strip unloading (red horizontal line).

Appendix B

Validation for σ_{xz}

From Jaeger et al. (2009), the shear stresses in a half-space due to a linear increasing normal load are

$$\sigma_{xz} = \frac{P}{2\pi}\{1 - (z/b)(\theta_1 - \theta_2) + \cos 2\theta_1\}. \tag{B.1}$$

This was found to be wrong as the shear stresses should vanish at the free surface and this is not observed in equation B.1. In order to make this happen we tried changing equation B.1 with

$$\sigma_{xz} = \frac{P}{2\pi}\{1 - (z/b)(\theta_1 - \theta_2) - \cos 2\theta_1\}. \tag{B.2}$$

which seemed to have solved the issue.

However, a proper validation of equation B.2 is still needed. To do so, we can imagine the right triangle of figure 2.7 to be made of a discrete series of rectangles with linearly increasing height. In terms of unloading, this would correspond to making use of the principle of superposition in order to build a discrete series of N uniform box unloadings, linearly increasing from 0 to P. As N approaches infinity this should approximate the continuous unloading distribution shown in figure 2.7. Equations 2.4 can be safely used for this purpose as they have already been validated by comparison to those provided by Davis & Selvadurai (1996). Mathematically, this is written

$$\sigma_{xz}^{val} = \frac{1}{\pi}\sum_{i=1}^{N} P_i \left(\sin(\theta_1^i - \theta_2^i)\sin(\theta_1^i + \theta_2^i) \right) \tag{B.3}$$

where $P = [P_1, P_2, ..., P_i, ..., P_N]$ is the linear increasing unloading distribution and

$$\theta_1^i = \arctan\left(\frac{z}{x - x_c^i - a}\right) \tag{B.4}$$

$$\theta_2^i = \arctan\left(\frac{z}{x - x_c^i + a}\right) \tag{B.5}$$

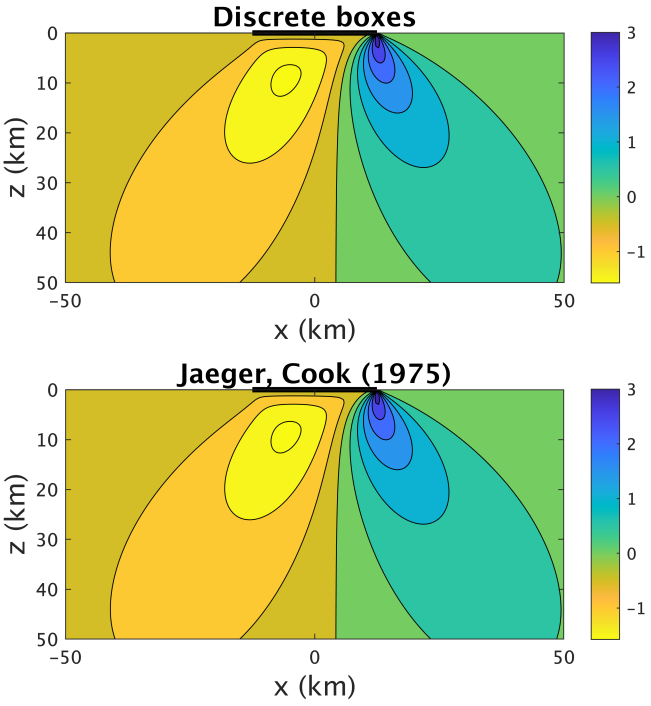

Figure B.1: Validation of equation B.2 through the procedure described in text. *Top:* superposition of linear increasing box unloadings. *Bottom:* corrected formula from Jaeger et al. (2009).

with x_c^i being the center coordinate of the i-th block and a the half width of a block, which in turn depends on the number of blocks N.

The comparison between equations B.3 and B.1 is shown in figure B.1 for $N = 1 \cdot 10^5$. The difference between the two is found to be symmetrical with respect to $x = 0$ and is therefore plotted in figure B.2 only for positive x values. Results for $N = 1 \cdot 10^5$ and $N = 1 \cdot 10^6$ are provided to show that the correspondence improves linearly with the number of boxes.

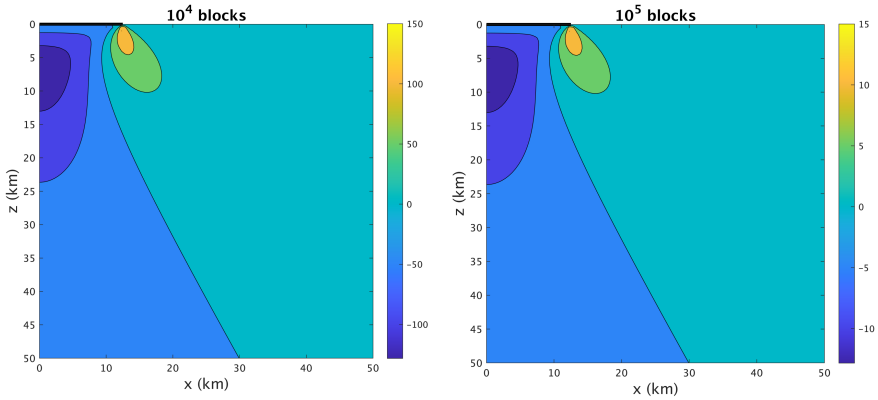

Figure B.2: Difference between equations B.2 and B.3, shown for two values of the number of blocks N.

Appendix C

Polar histograms of dike orientations

Figures C.1 and C.2 show the distribution of orientations for emplaced dikes at each step of the simulations described in section 4.5 for the full and half-graben cases, respectively. Dike orientations are shown as polar histograms (or rose plots) representing the distribution of dip angles of the dikes calculated as an average over their individual segments and read as an output from the simulations. Note that each histogram considers the number of dikes emplaced during the corresponding simulation step and all the previous ones for its calculations and that observations are not normalized. Figures C.3 and C.4 also show polar histograms for the full-graben simulations described in section 4.6, split in two separate images for the sake of visibility.

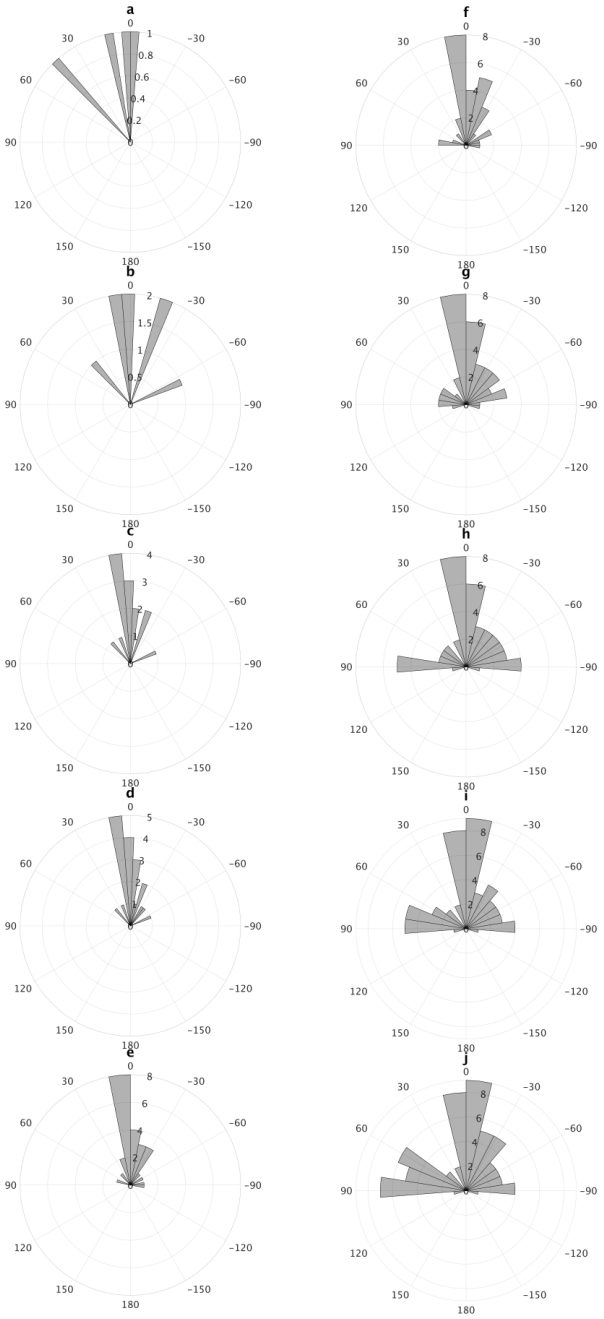

Figure C.1: Polar histograms of dike orientations for the full-graben simulation described in section 4.5.

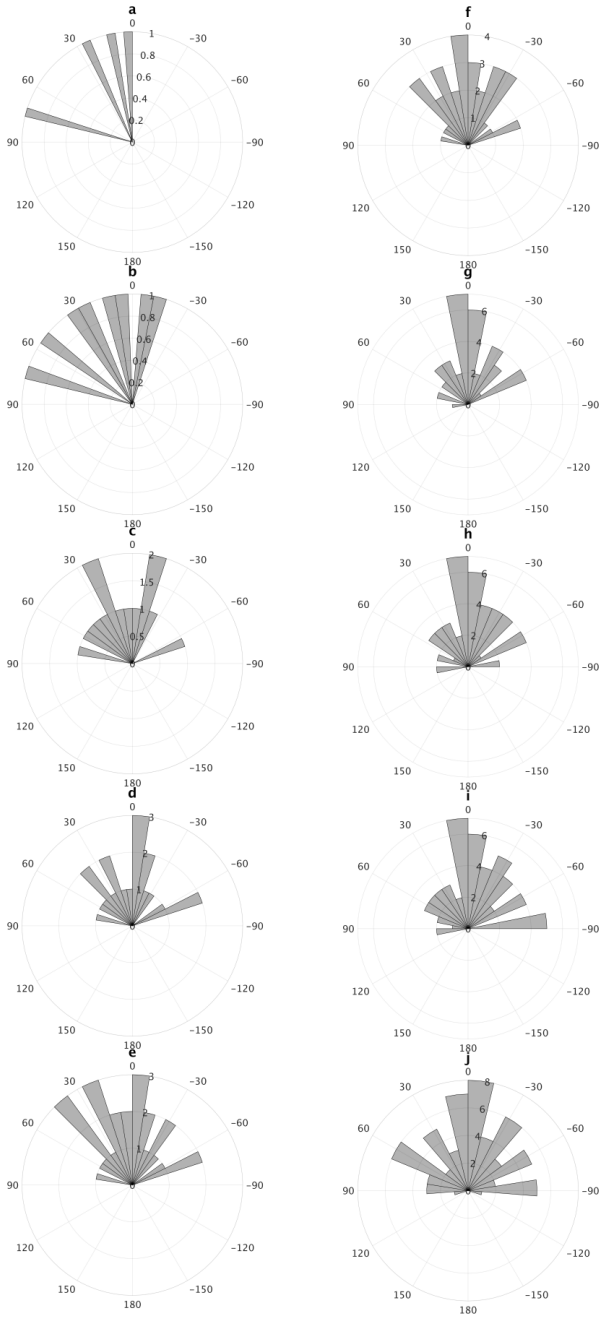

Figure C.2: Polar histograms of dike orientations for the half-graben simulations described in section 4.5.

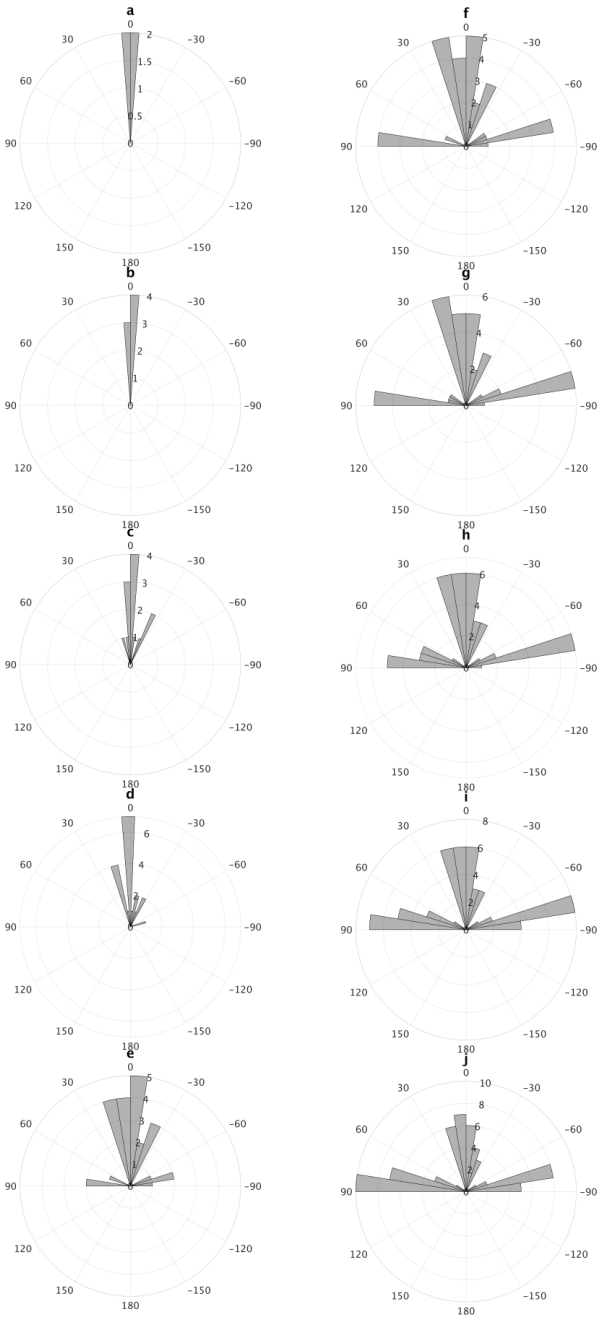

Figure C.3: Polar histograms of dike orientations for the full-graben simulation described in section 4.6. Panels continue in figure C.4.

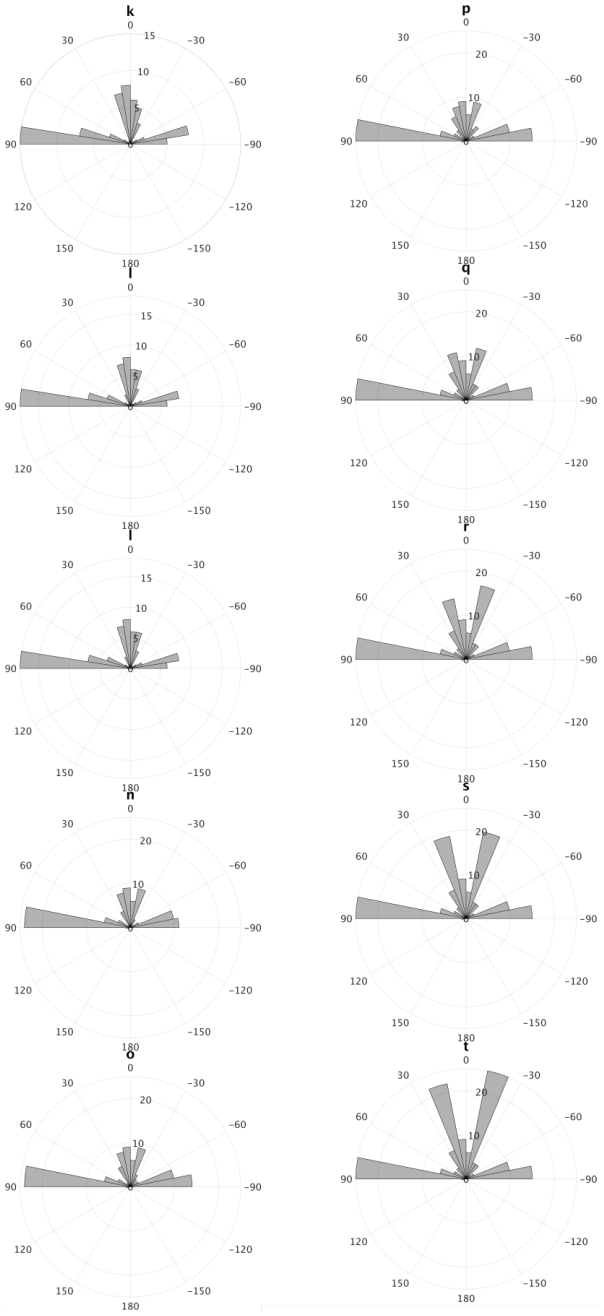

Figure C.4: Polar histograms of dike orientations for the full-graben simulation described in section 4.6.

Appendix D

Additional information

Run	n	n_{tot}	D (m)	x_{inj} (km)	z_{inj} (km)
1	4	4	100	3.2, -13.1, -4.3, 5.4	40
2	4	8	200	7.3, -0.6, 7.1, -2.0	40
3	6	14	300	-2.0, -12.1, 29.1, 8.3, 13.8, -10.6	40
4	6	20	400	-13.3, 11.3, 3.5, -6.0, 7.5, -2.6	40
5	6	26	500	-3.0, -8.5, -11.2, 25.3, 16.6, 3.1	40
6	6	32	600	5.5, 10.4, -11.1, 12.6, -6.6, -1.1	40
7	8	40	700	-7.1, -11.7, -1.9, 2.7, 15.3, 6.1, -10.6, 16.0	38
8	8	48	800	12.3, -2.3, -15.1, -4.4, 15.2, 2.8, -5.6, 4.4	37
9	8	56	900	4.0, -12.5, -9.5, -7.4, 5.1, -3.2, 10.1, -30.3	36
10	8	64	1000	-4.5, 12.4, -10.7, 9.3, 3.5, -7.2, 1.8, -15.6	35

Table D.1: Some of the parameters employed in the dike simulations leading to figure 4.5. n is the number of dikes launched at each run; n_{tot} is the cumulative number of dikes launched up to the run in account; x_{inj} and z_{inj} represent the x and z coordinates of injection in starting order.

Run	n	n_{tot}	D (m)	x_{inj} (km)	z_{inj} (km)
1	4	4	100	-7.3, -0.5, 2.3, 4.3	40
2	4	8	200	-5.9, -2.8, 4.2, 16.7	40
3	6	14	300	4.7, 12.1, -0.7, 6.5, -3.3, -10.8	40
4	6	20	400	10.0, -6.5, 2.6, -9.4, -13.2, 9.3	40
5	6	26	500	-10.1, -4.7, 1.4, -2.9, 3.0, 4.8	40
6	6	32	600	-2.5, -14.3, -0.2, -5.6, 21.8, 11.4	40
7	8	40	700	-25.0, 4.4, -14.0, -2.6, 1.6, 7.5, -2.7, 15.8	40
8	8	48	800	18.6, -6.0, 1.0, 5.6, 11.1, -9.0, -2.6, -12.2	39
9	8	56	900	9.4, 7.9, -8.8, 3.2, -5.6, -12.0, 15.7, -10.3	38
10	8	64	1000	-14.8, -10.2, -4.5, 7.1, 11.3, -2.9, 12.6, 4.8	37

Table D.2: Some of the parameters employed in the dike simulations leading to figure 4.6. n is the number of dikes launched at each run; n_{tot} is the cumulative number of dikes launched up to the run in account; x_{inj} and z_{inj} represent the x and z coordinates of injection in starting order.

Run	n	n_{tot}	D (m)	T (m)	x_{inj} (km)	z_{inj} (km)
1	4	4	100	0	7.9, -32.7, -10.8, 18.6	40
2	4	8	200	0	18.1, -1.6, 17.9, -5.1	
3	6	14	300	0	17.9, 40.2, -12.2, 25.8, 18.2, -7.6	40
4	6	20	400	0	7.3, -19.7, 22.2, -28.7, 26.7, -20.2	40
5	6	26	500	0	-2.6, -6.0, 8.0, 17.8, -21.6, 0.8	39
6	6	32	600	0	-4.1, 15.7, 27.3, -27.7, 21.6, 1.9	38
7	8	40	700	0	-5.6, 27.9, -27.2, 0.8, 13.8, 17.5, -38.6, -2.1	36
8	8	48	800	0	-37.3, -18.6, -26.5, 58.8, -15.4, 18.7, -4.8, 22.2	36
9	8	56	900	0	1.9, -2.7, -20.1, 3.2, -0.7, -11.1, 5.4, 1.1	34
10	8	64	1000	0	-10.9, -44.8, 21.0, -2.2, 2.5, -13.6, 7.6, -15.0	32

Table D.3: Some of the parameters employed in the dike simulations leading to figure 4.8. n is the number of dikes launched at each run; n_{tot} is the cumulative number of dikes launched up to the run in account; x_{inj} and z_{inj} represent the x and z coordinates of injection in starting order. T is the thickness of the sedimentary layer.

Run	n	n_{tot}	D (m)	T (m)	x_{inj} (km)	z_{inj} (km)
11	8	72	1000	100	-28.7, 2.6, 18.1, -4.6, -1.6, 4.7, -2.1, -48.3	31
12	8	80	1000	200	25.5, -3.3, -17.9, 3.7, -5.6, -14.7, 7.3, -21.2	30
13	8	88	1000	300	-0.5, 20.7, -8.2, 11.7, -11.2, -15.6, 14.6, 25.7	29
14	8	96	1000	400	3.2, 7.7, -13.4, 12.9, -6.5, -23.5, -2.1, 21.7	28
15	8	104	1000	500	2.8, -6.2, -26.6, 14.1, -0.8, -15.7, 27.6, 5.4	27
16	8	112	1000	600	-2.8, -1.1, -6.5, 11.1, -19.8, -31.3, 23.7, 1.5	26
17	8	120	1000	700	-2.3, -1.0, 10.6, 35.7, -11.4, 1.1, -26.7, 23.3	25
18	8	128	1000	800	8.8, -13.7, -2.6, -39.1, -2.1, 40.1, 2.5, 31.0	25
19	8	136	1000	800	-1.4, -5.3, 6.8, 10.7, -9.3, -5.9, 50.6, -56.5	25
20	8	144	1000	800	6.4, -3.6, -33.0, 5.1, 10.0, -11.4, 22.8, 14.9	25

Table D.4: Some of the parameters employed in the dike simulations leading to figure 4.9. n is the number of dikes launched at each run; n_{tot} is the cumulative number of dikes launched up to the run in account; x_{inj} and z_{inj} represent the x and z coordinates of injection in starting order. T is the thickness of the sedimentary layer.

Acknowledgements

Thanks to Eleonora, for letting me tell this wonderful story and patiently leading me through it. None of this would have been possible without your manifold guidance.

Thanks to Francesco, for disclosing the functioning of his amazing code and never being hesitant to help.

Thanks to Francesca, Lorenzo, Mehdi, Tim and Valentina for all the advice and willingness to support, and for making me feel part of your group.

Thanks to my parents, my only milestones through this and every journey.

Bibliography

Acocella, V. (2021), *Volcano-Tectonic Processes*, Springer Nature.

Anderson, E. M. (1951), *The dynamics of faulting and dyke formation with applications to Britain*, Oliver and Boyd.

Anderson, E. M. (1972), *The dynamics of faulting and dyke formation with applications to Britain*, Hafner Publishing Company.

Bangerth, W., Dannberg, J., Fraters, M., Gassmoeller, R., Glerum, A., Heister, T. & Naliboff, J. (2021), 'ASPECT: Advanced Solver for Problems in Earth's ConvecTion, User Manual'. doi:10.6084/m9.figshare.4865333.
URL: *https://doi.org/10.6084/m9.figshare.4865333*

Barker, T. G. (1976), 'Quasi-static motions near the san andreas fault zone', *Geophysical Journal International* **45**(3), 689–705.

Birt, C., Maguire, P., Khan, M., Thybo, H., Keller, G. R. & Patel, J. (1997), 'The influence of pre-existing structures on the evolution of the southern kenya rift valley—evidence from seismic and gravity studies', *Tectonophysics* **278**(1-4), 211–242.

Bonini, M., Corti, G., Innocenti, F., Manetti, P., Mazzarini, F., Abebe, T. & Pecskay, Z. (2005), 'Evolution of the main ethiopian rift in the frame of afar and kenya rifts propagation', *Tectonics* **24**(1).

Bosworth, W. (1987), 'Off-axis volcanism in the gregory rift, east africa: Implications for models of continental rifting', *Geology* **15**(5), 397–400.

Bott, M. (1976), Formation of sedimentary basins of graben type by extension of the continental crust, *in* 'Developments in Geotectonics', Vol. 12, Elsevier, pp. 77–86.

Bott, M. (2006), Mechanisms of rifting: geodynamic modeling of continental rift systems, *in* 'Developments in Geotectonics', Vol. 25, Elsevier, pp. 27–43.

Braile, L., Keller, G., Wendlandt, R., Morgan, P. & Khan, M. (2006), The east african rift system, *in* 'Developments in Geotectonics', Vol. 25, Elsevier, pp. 213–III.

Brun, J.-P. (1999), 'Narrow rifts versus wide rifts: inferences for the mechanics of rifting from laboratory experiments', *Philosophical Transactions of the Royal Society of London. Series A: Mathematical, Physical and Engineering Sciences* **357**(1753), 695–712.

Buck, W. R. (1991), 'Modes of continental lithospheric extension', *Journal of Geophysical Research: Solid Earth* **96**(B12), 20161–20178.

Buck, W. R. (2004), 1. consequences of asthenospheric variability on continental rifting, *in* 'Rheology and deformation of the lithosphere at continental margins', Columbia University Press, pp. 1–30.

Burchardt, S. (2018), *Volcanic and Igneous Plumbing Systems: Understanding Magma Transport, Storage, and Evolution in the Earth's Crust*, Elsevier.

Bürgmann, R. & Dresen, G. (2008), 'Rheology of the lower crust and upper mantle: Evidence from rock mechanics, geodesy, and field observations', *Annu. Rev. Earth Planet. Sci.* **36**, 531–567.

Burke, K. (1977), 'Aulacogens and continental breakup', *Annual Review of Earth and Planetary Sciences* **5**(1), 371–396.

Burke, K. (2011), 'Plate tectonics, the wilson cycle, and mantle plumes: geodynamics from the top', *Annual Review of Earth and Planetary Sciences* **39**, 1–29.

Chernet, T., Hart, W. K., Aronson, J. L. & Walter, R. C. (1998), 'New age constraints on the timing of volcanism and tectonism in the northern main ethiopian rift–southern afar transition zone (ethiopia)', *Journal of Volcanology and Geothermal Research* **80**(3-4), 267–280.

Condie, K. C. (2013), *Plate tectonics & crustal evolution*, Elsevier.

Corbi, F., Rivalta, E., Pinel, V., Maccaferri, F., Bagnardi, M. & Acocella, V. (2015), 'How caldera collapse shapes the shallow emplacement and transfer of magma in active volcanoes', *Earth and Planetary Science Letters* **431**, 287–293.

Corti, G. (2009), 'Continental rift evolution: from rift initiation to incipient break-up in the main ethiopian rift, east africa', *Earth-Science Reviews* **96**(1-2), 1–53.

Craig, T., Jackson, J., Priestley, K. & McKenzie, D. (2011), 'Earthquake distribution patterns in africa: their relationship to variations in lithospheric and geological structure, and their rheological implications', *Geophysical Journal International* **185**(1), 403–434.

Crouch, S. L., Starfield, A. M. & Rizzo, F. (1983), 'Boundary element methods in solid mechanics'.

Dahm, T. (2000), 'Numerical simulations of the propagation path and the arrest of fluid-filled fractures in the earth', *Geophysical Journal International* **141**(3), 623–638.

Davis, R. & Selvadurai, A. (1996), *Elasticity and Geomechanics*, Cambridge University Press.
URL: *https://books.google.it/books?id=0HpfQgAACAAJ*

Davis, T. (2021), An analytical and numerical analysis of fluid-filled crack propagation in three dimensions, PhD thesis, Universität Potsdam.

Davis, T., Bagnardi, M., Lundgren, P. & Rivalta, E. (2021), 'Extreme curvature of shallow magma pathways controlled by competing stresses: insights from the 2018 sierra negra eruption', *Geophysical Research Letters* **48**(13), e2021GL093038.

Déverchère, J., Petit, C., Gileva, N., Radziminovitch, N., Melnikova, V. & San'Kov, V. (2001), 'Depth distribution of earthquakes in the baikal rift system and its implications for the rheology of the lithosphere', *Geophysical Journal International* **146**(3), 714–730.

Dunbar, J. A. & Sawyer, D. S. (1988), 'Continental rifting at pre-existing lithospheric weaknesses', *Nature* **333**(6172), 450–452.

Ellis, M. & King, G. (1991), 'Structural control of flank volcanism in continental rifts', *Science* **254**(5033), 839–842.

Gaete, A., Kavanagh, J. L., Rivalta, E., Hazim, S. H., Walter, T. R. & Dennis, D. J. (2019), 'The impact of unloading stresses on post-caldera magma intrusions', *Earth and Planetary Science Letters* **508**, 109–121.

Gerya, T. (2019), *Introduction to numerical geodynamic modelling*, Cambridge University Press.

Hooper, A., Ófeigsson, B., Sigmundsson, F., Lund, B., Einarsson, P., Geirsson, H. & Sturkell, E. (2011), 'Increased capture of magma in the crust promoted by ice-cap retreat in iceland', *Nature Geoscience* **4**(11), 783–786.

Ito, G. & Martel, S. J. (2002), 'Focusing of magma in the upper mantle through dike interaction', *Journal of Geophysical Research: Solid Earth* **107**(B10), ECV–6.

Jaeger, J. C., Cook, N. G. & Zimmerman, R. (2009), *Fundamentals of rock mechanics*, John Wiley & Sons.

Kavanagh, J. L. (2018), Mechanisms of magma transport in the upper crust—dyking, *in* 'Volcanic and igneous plumbing systems', Elsevier, pp. 55–88.

Keranen, K. & Klemperer, S. (2008), 'Discontinuous and diachronous evolution of the main ethiopian rift: Implications for development of continental rifts', *Earth and Planetary Science Letters* **265**(1-2), 96–111.

Keranen, K. M., Klemperer, S. L., Julia, J., Lawrence, J. F. & Nyblade, A. A. (2009), 'Low lower crustal velocity across ethiopia: Is the main ethiopian rift a narrow rift in a hot craton?', *Geochemistry, Geophysics, Geosystems* **10**(5).

Kiselev, A. (1987), 'Volcanism of the baikal rift zone', *Tectonophysics* **143**(1-3), 235–244.

Kühn, D. & Dahm, T. (2008), 'Numerical modelling of dyke interaction and its influence on oceanic crust formation', *Tectonophysics* **447**(1-4), 53–65.

Kusznir, N. J., Roberts, A. M. & Morley, C. K. (1995), 'Forward and reverse modelling of rift basin formation', *Geological Society, London, Special Publications* **80**(1), 33–56.

Le Corvec, N. (2013), Physical and structural controls on monogenetic basaltic volcanism, and implications for the evolution of the Auckland Volcanic Field, PhD thesis, ResearchSpace@ Auckland.

Lustrino, M. & Carminati, E. (2007), 'Phantom plumes in europe and the circum-mediterranean region', *SPECIAL PAPERS-GEOLOGICAL SOCIETY OF AMERICA* **430**, 723.

Maccaferri, F. (2010), 'Numericals and analogue models of fluid-filled fractures propagation in layered media: Application to dikes and hydrofractures'.

Maccaferri, F., Bonafede, M. & Rivalta, E. (2010), 'A numerical model of dyke propagation in layered elastic media', *Geophysical Journal International* **180**(3), 1107–1123.

Maccaferri, F., Bonafede, M. & Rivalta, E. (2011), 'A quantitative study of the mechanisms governing dike propagation, dike arrest and sill formation', *Journal of Volcanology and Geothermal Research* **208**(1-2), 39–50.

Maccaferri, F., Rivalta, E., Keir, D. & Acocella, V. (2014), 'Off-rift volcanism in rift zones determined by crustal unloading', *Nature Geoscience* **7**(4), 297–300.

Maccaferri, F., Smittarello, D., Pinel, V. & Cayol, V. (2019), 'On the propagation path of magma-filled dikes and hydrofractures: The competition between external stress, internal pressure, and crack length', *Geochemistry, Geophysics, Geosystems* **20**(4), 2064–2081.

Mackenzie, G., Thybo, H. & Maguire, P. (2005), 'Crustal velocity structure across the main ethiopian rift: results from two-dimensional wide-angle seismic modelling', *Geophysical Journal International* **162**(3), 994–1006.

Mantiloni, L., Davis, T., Gaete Rojas, A. B. & Rivalta, E. (2021), 'Stress inversion in a gelatin box: testing eruptive vent location forecasts with analog models.', *Geophysical Research Letters* .

Merle, O. (2011), 'A simple continental rift classification', *Tectonophysics* **513**(1-4), 88–95.

Michon, L. & Merle, O. (2001), 'The evolution of the massif central rift; spatio-temporal distribution of the volcanism', *Bulletin de la Société géologique de France* **172**(2), 201–211.

Morgan, P. & Ramberg, I. B. (1987), 'Physical changes in the lithosphere associated with thermal relaxation after rifting', *Tectonophysics* **143**(1-3), 1–11.

Muller, J. R., Ito, G. & Martel, S. J. (2001), 'Effects of volcano loading on dike propagation in an elastic half-space', *Journal of Geophysical Research: Solid Earth* **106**(B6), 11101–11113.

Nakashima, Y. (1993), 'Static stability and propagation of a fluid-filled edge crack in rock: Implication for fluid transport in magmatism and metamorphism', *Journal of Physics of the Earth* **41**(3), 189–202.

Olsen, K. & Morgan, P. (2006), Introduction: progress in understanding continental rifts, *in* 'Developments in Geotectonics', Vol. 25, Elsevier, pp. 3–26.

Pollard, D., Pollard, D. D., Fletcher, R. C. & Fletcher, R. C. (2005), *Fundamentals of structural geology*, Cambridge University Press.

Ritsema, J., van Heijst, H. J. & Woodhouse, J. H. (1999), 'Complex shear wave velocity structure imaged beneath africa and iceland', *Science* **286**(5446), 1925–1928.

Rivalta, E., Taisne, B., Bunger, A. & Katz, R. (2015), 'A review of mechanical models of dike propagation: Schools of thought, results and future directions', *Tectonophysics* **638**, 1–42.

Rooney, T., Furman, T., Bastow, I., Ayalew, D. & Yirgu, G. (2007), 'Lithospheric modification during crustal extension in the main ethiopian rift', *Journal of Geophysical Research: Solid Earth* **112**(B10).

Rosendahl, B., Reynolds, D., Lorber, P., Burgess, C., McGill, J., Scott, D., Lambiase, J. & Derksen, S. (1986), 'Structural expressions of rifting: lessons from lake tanganyika, africa', *Geological Society, London, Special Publications* **25**(1), 29–43.

Rubin, A. M. (1993), 'Dikes vs. diapirs in viscoelastic rock', *Earth and Planetary Science Letters* **119**(4), 641–659.

Segall, P. (2010), *Earthquake and volcano deformation*, Princeton University Press.

Sengor, A. (1995), 'Sedimentation and tectonics of fossil rifts.', *Tectonics of sedimentary basins* pp. 53–117.

Sengör, A. C. & Burke, K. (1978), 'Relative timing of rifting and volcanism on earth and its tectonic implications', *Geophysical Research Letters* **5**(6), 419–421.

Şengör, A. C. & Natal'in, B. A. (2001), 'Rifts of the world', *Geological Society of America Special Papers* **352**, 389–482.

Spence, D., Sharp, P. & Turcotte, D. (1987), 'Buoyancy-driven crack propagation: a mechanism for magma migration', *Journal of Fluid Mechanics* **174**, 135–153.

Sternai, P. (2020), 'Surface processes forcing on extensional rock melting', *Scientific reports* **10**(1), 1–13.

Thatcher, W. (1983), 'Nonlinear strain buildup and the earthquake cycle on the san andreas fault', *Journal of Geophysical Research: Solid Earth* **88**(B7), 5893–5902.

Thybo, H. & Artemieva, I. (2013), 'Moho and magmatic underplating in continental lithosphere', *Tectonophysics* **609**, 605–619.

Thybo, H. & Nielsen, C. (2009), 'Magma-compensated crustal thinning in continental rift zones', *Nature* **457**(7231), 873–876.

Turcotte, D. L. (1979), Flexure, *in* 'Advances in geophysics', Vol. 21, Elsevier, pp. 51–86.

Turcotte, D. L. & Schubert, G. (2002), *Geodynamics*, Cambridge university press.

Watanabe, T., Masuyama, T., Nagaoka, K. & Tahara, T. (2002), 'Analog experiments on magma-filled cracks competition between external stresses and internal pressure', *Earth, planets and space* **54**(12), 1247–1261.

Weertman, J. (1971), 'Theory of water-filled crevasses in glaciers applied to vertical magma transport beneath oceanic ridges', *Journal of Geophysical Research* **76**(5), 1171–1183.

Wernicke, B. (1985), 'Uniform-sense normal simple shear of the continental lithosphere', *Canadian Journal of Earth Sciences* **22**(1), 108–125.

Woldegabriel, G., Aronson, J. L. & Walter, R. C. (1990), 'Geology, geochronology, and rift basin development in the central sector of the main ethiopia rift', *Geological Society of America Bulletin* **102**(4), 439–458.

Wolfenden, E., Ebinger, C., Yirgu, G., Deino, A. & Ayalew, D. (2004), 'Evolution of the northern main ethiopian rift: birth of a triple junction', *Earth and Planetary Science Letters* **224**(1-2), 213–228.

Xu, W., Jónsson, S., Corbi, F. & Rivalta, E. (2016), 'Graben formation and dike arrest during the 2009 harrat lunayyir dike intrusion in saudi arabia: Insights from insar, stress calculations and analog experiments', *Journal of Geophysical Research: Solid Earth* **121**(4), 2837–2851.

Ziegler, P. A. & Cloetingh, S. (2004), 'Dynamic processes controlling evolution of rifted basins', *Earth-Science Reviews* **64**(1-2), 1–50.

Ziv, A., Rubin, A. M. & Agnon, A. (2000), 'Stability of dike intrusion along preexisting fractures', *Journal of Geophysical Research: Solid Earth* **105**(B3), 5947–5961.